UNIVERSITÀ CAMPUS BIO-MEDICO DI ROMA

CORSO DI DOTTORATO DI RICERCA IN

SUSTAINABLE DEVELOPMENT: ENVIRONMENT, FOOD AND HEALTH

Curriculum *Health, Nutrition and Ageing*

XXXVIII ciclo

Midbrain degeneration triggers astrocyte reactivity and tau pathology in experimental Alzheimer's Disease

Relatore:

Prof. Marcello D'Amelio

Correlatrice:

Dott.ssa Paraskevi Krashia

Dottoranda:

Gilda Loffredo

ANNO ACCADEMICO 2024/2025

Abstract

Smaller midbrain volumes have been identified as predictors of Alzheimer's disease (AD) progression and of faster conversion from Mild Cognitive Impairment (MCI) to dementia. Consistently, several midbrain-target regions exhibit neuroinflammation as early as the MCI stage. The concomitant presence of neuroinflammation, amyloid-β (Aβ) and tau pathology appears to be a strong predictor of conversion to dementia. However, the mechanisms through which midbrain degeneration contributes to disease progression − particularly how it triggers neuroinflammation in midbrain-target areas such as the hippocampus − remain unclear.

To address this gap, using adult C57BL/6N mice, we generated a new mouse model bearing lesions in three midbrain nuclei: the dopaminergic Ventral Tegmental Area (VTA) and Substantia Nigra pars compacta (SNpc), and the serotonergic Interpeduncular Nucleus (IPN). This new model allowed us to evaluate the consequences of dopamine (DA) and serotonin (5-HT) depletion in downstream target regions. We characterized the model through stereological cell counts, analyses of monoaminergic fibres and monoamine levels, electrophysiological recordings, and behavioural testing. Hippocampal neuroinflammation was determined by quantifying glial cells, assessing morphological changes, evaluating NLRP3 inflammasome activation and cytokine levels, and performing microglial transcriptional profiling. In parallel, we induced analogous midbrain lesions in Tg2576 transgenic mice, which overexpress the Swedish mutant of amyloid precursor protein, to examine how monoamine depletion interacts with Aβ accumulation.

While lesions in C57BL/6N mice enabled isolation of the effects of monoaminergic dysfunction, lesions in Tg2576 mice provided insight into the interplay between impaired monoaminergic signalling and Aβ-driven pathology. In C57BL/6N mice, combined DA and 5-HT depletion within the hippocampus elicited pronounced microglial activation *via* NLRP3 inflammasome signalling

resulting in elevated IL-1β expression. Pharmacological treatment with dopaminergic agents (L-DOPA or A68930) or the serotonergic agent (fluoxetine) fully prevented this inflammatory response. In Tg2576 mice, superimposed midbrain degeneration markedly exacerbated AD-like pathology, including intensified microglial and astrocytic reactivity, accelerated Aβ plaque deposition, and induction of pathological tau hyperphosphorylation. Notably, L-DOPA or fluoxetine treatment significantly reduced astrocytic activation and tau hyperphosphorylation in lesioned Tg2576 mice.

These findings underscore the pivotal role of midbrain integrity in modulating neuroinflammatory cascades and AD progression. They provide mechanistic insight into the accelerated cognitive decline observed in patients with midbrain deficits and support the development of precision medicine strategies targeting monoaminergic dysfunction in neurodegenerative disease.

INDEX

1. INTRODUCTION

1.1 Thesis Overview

Alzheimer's disease (AD) is no longer considered as a disorder that begins with memory impairment but is instead regarded as a long-lasting biological process in which pathological mechanisms unfold decades before the onset of dementia. Despite extensive characterization of amyloid-β (Aβ) and tau pathology, the factors that determine whether early molecular alterations progress to neurodegeneration and cognitive decline remain only partially understood (**Figure 1**)[1]. Increasing evidence indicates that neuroinflammation is not a secondary epiphenomenon of protein aggregation, but a key driver of the disease progression. Understanding the upstream mechanisms that initiate and sustain maladaptive microglia and astrocytes activation in vulnerable brain regions is therefore crucial.

Among the earliest brain alterations observed in AD are structural and functional changes affecting midbrain monoaminergic nuclei, including dopaminergic and serotonergic systems. These neuromodulatory circuits exert a powerful regulatory control over synaptic plasticity, network stability, and immune homeostasis, suggesting that their early dysfunction may predispose the hippocampus to neuroinflammatory processes.

This thesis is based on the hypothesis that early dysfunction of midbrain monoaminergic systems represents an upstream pathogenic event that lowers the threshold for hippocampal neuroinflammation, thereby accelerating tau pathology and cognitive decline in AD.

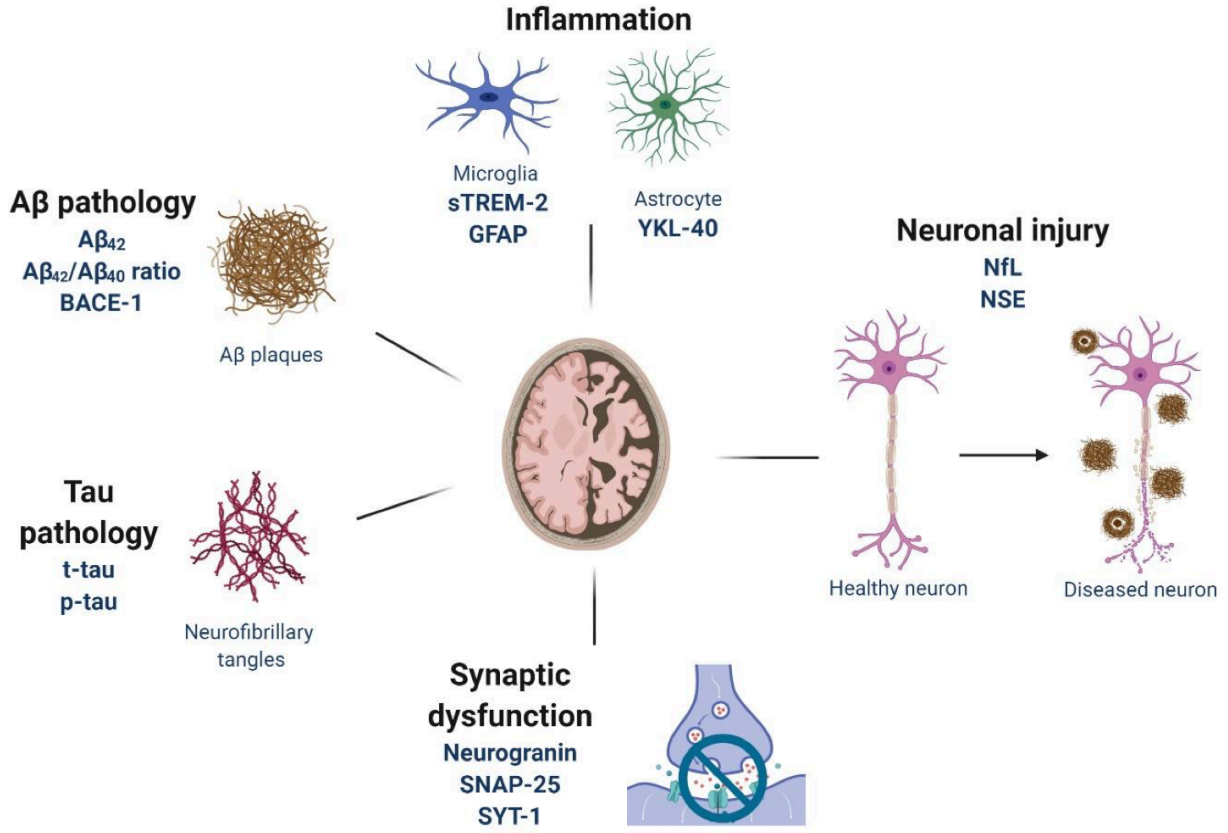

Figure 1: The neuropathology of AD. The neuropathological microscopical hallmarks of AD are extracellular Aβ plaques, intracellular neurofibrillary tangles and neuroinflammation. At the anatomical level, AD brains display synaptic and neuronal loss, ultimately resulting in brain atrophy[1].

1.2 Alzheimer's Disease

1.2.1 Epidemiology and risk factors

AD is the most common cause of dementia and represents a major medical, social, and economic challenge worldwide. Beyond its impact, AD is increasingly conceptualized as a long-lasting biological process in which molecular, cellular, and network-level alterations precede the onset of overt cognitive symptoms by up to two decades[2]. This paradigm shift has reframed AD from a *late-onset* cognitive disorder to a progressive pathophysiological continuum (referred as *AD continuum*), emphasizing the importance of identifying early upstream mechanisms that drive the disease progression.

The prevalence of AD increases exponentially with age, making population aging the primary factor contributing to its growing global burden[3]. However, AD cannot be considered as an inevitable consequence of aging. Instead, it emerges from the complex interplay between genetic susceptibility, systemic health, lifestyle factors, and brain-specific vulnerabilities[3].

Rare autosomal dominant mutations in genes involved in amyloid precursor protein (APP) processing, including APP, PSEN1, and PSEN2, cause *early-onset* familial AD and provided the first causal evidence linking amyloid-β (Aβ) dysregulation to disease pathogenesis[4].

However, the vast majority of AD cases are sporadic and *late-onset*. Both genetic and non-genetic risk factors act as modulators of individual susceptibility, influencing disease risk and progression. Among genetic determinants, the ε4 allele of apolipoprotein E (APOE ε4) remains the strongest[5–7]. This risk factor affects not only amyloid deposition but also lipid homeostasis, synaptic integrity, and innate immune responses, thereby highlighting the convergence of metabolic and inflammatory pathways in AD vulnerability[8]. Non-genetic risk factors, including hypertension, diabetes, obesity, and dyslipidaemia, are consistently associated with increased AD risk, further supporting a tight link between systemic vascular dysfunction and brain resilience[9]. In parallel, lifestyle-related factors, including physical inactivity, less education, excessive alcohol consumption, reduced cognitive reserve, infrequent social contact, chronic stress, depression and sleep disturbances, shape individual vulnerability to AD[9].

Collectively, these observations reinforce the concept of AD as a systemic disorder in which peripheral and central immune–metabolic alterations critically interact.

1.2.2 Stages of AD continuum

Clinically, AD unfolds along a continuum that broadly parallels the progressive accumulation and spatial propagation of neuropathological alterations, although with a substantial temporal gap between pathology and symptom onset[2].

The preclinical stage is defined by the presence of AD-related biological changes in individuals who remain cognitively unimpaired[10–14]. Advances in cerebrospinal fluid biomarkers and molecular neuroimaging have demonstrated that these pathological processes can be detected up to decades before the onset of overt clinical symptoms[10–14]. A landmark 20-year longitudinal study, involving 648 participants who developed AD, revealed a precise temporal sequence of biomarker changes preceding clinical diagnosis. CSF $A\beta_{42}$ concentrations diverged from normal controls approximately 18 years before diagnosis, representing the earliest detectable abnormality. This was followed by alterations in the $A\beta_{42}/A\beta_{40}$ ratio at 14 years, phosphorylated tau 181 at 11 years, total tau at 10 years, and neurofilament light chain at 9 years before diagnosis. Structural brain changes, specifically hippocampal volume reduction, became apparent 8 years before diagnosis, while measurable cognitive decline on the Clinical Dementia Rating Scale emerged around 6 years prior to clinical diagnosis. Notably, the rate of biomarker changes initially accelerated during the preclinical phase, before subsequently slowing as clinical dementia became manifest[15].

As pathology progresses, a subset of individuals transitions to a prodromal phase commonly referred to as Mild Cognitive Impairment (MCI), characterized by measurable cognitive decline − particularly in episodic memory − while functional independence remained largely preserved[16,17]. Importantly, MCI represents a clinically and biologically heterogeneous condition, as only a fraction of affected individuals progress to dementia. This heterogeneity underscores the existence of disease-modifying mechanisms that critically influence the rate and likelihood of clinical conversion.

The dementia stage of AD − moderate and severe − is instead marked by progressive impairment across multiple cognitive domains that can include increased memory loss, confusion, inability to learn new information, language difficulties, and challenges with reading, writing, working with numbers, and problems in organizing thoughts. Subjects also show significant personality changes such as apathy, depression, delusions or agitation. Symptoms during this stage may be quite distressing, even dangerous for patients and their caregivers[18]. These clinical manifestations closely reflect the widespread dissemination of tau pathology, sustained neuroinflammatory activation, synaptic dysfunction, and neuronal loss across large-scale brain networks[19–23].

1.2.3 The amyloid cascade hypothesis and its limitation

The amyloid cascade hypothesis has historically provided the dominant framework for understanding AD pathogenesis. According to this model, abnormal accumulation of Aβ peptides − arising from altered APP processing − represents the initiating event that triggers a cascade of downstream pathological processes, including tau hyperphosphorylation, synaptic dysfunction, neuroinflammation, and neurodegeneration[4].

Although this hypothesis is strongly supported by genetic evidence from familial AD, its limitations have become increasingly evident. A substantial proportion of cognitively unimpaired individuals harbour significant amyloid burden, indicating that amyloid pathology alone is insufficient to drive clinical decline[24]. Moreover, amyloid load correlates poorly with symptom severity, whereas tau pathology and neuroinflammatory markers show a much stronger association with cognitive impairment and disease progression[2,25].

Consequently, converging evidence increasingly conceptualize amyloid pathology as a necessary but not sufficient condition for neurodegeneration. Within this revised framework, Aβ accumulation acts as an upstream permissive factor that sensitizes neural circuits to secondary

pathological mechanisms − most notably tauopathy and sustained neuroinflammation − which ultimately determine the clinical outcome.

This shift provides a conceptual foundation for investigating additional disease modifiers, including early dysfunction of neuromodulatory systems, such as dopamine (DA) and serotonin (5-HT) signalling, that may critically shape the trajectory from preclinical pathology to overt dementia.

1.3 Dopaminergic and Serotonergic Systems

1.3.1 The Dopaminergic System: Sources, Connections, and Functions

DA neurons are primarily located in midbrain nuclei, including the Substantia Nigra *pars compacta* (SNpc) and the Ventral Tegmental Area (VTA)[26–28] (**Figure 2A**). Neurons in the SNpc form the nigrostriatal pathway, which mainly projects to the dorsal striatum and is essential for motor control, whereas VTA neurons give rise to the mesocorticolimbic pathway, innervating limbic and cortical regions such as the nucleus accumbens (NAc), hippocampus, amygdala, and prefrontal cortex[29,30]. The VTA acts as a hub integrating internal states and environmental cues, receiving inputs from multiple brain regions, modulating downstream circuits through long axons and extensive arborization (**Figure 2B**). This architecture allows precise neuromodulation, but also confers high vulnerability to metabolic stress and pathological insults[27]. The hippocampus receives direct VTA/SNpc dopaminergic innervation, which is critical for synaptic plasticity and memory encoding[30–33].

Notably, although the Locus Coeruleus (LC) is classically defined by its noradrenergic projections, it is also capable of DA release, prompting a reassessment of earlier studies that attribute LC-mediated effects exclusively to norepinephrine (NE). Recent findings have indeed revealed that

the LC significantly modulates hippocampal-dependent memory and synaptic strength[34–37] primarily *via* DA receptor (DR) activation rather than β-adrenergic pathways[34,35].

Rodent studies further support this mechanism showing that LC activation stabilizes hippocampal place cells and enhances spatial learning and memory[38–40], whereas LC suppression impairs these functions[34,39]. However, the extent to which LC-derived DA and NE exerts distinct, synergistic, or antagonistic effects remains unresolved, highlighting the need for receptor-specific and circuit-level analyses to fully elucidate LC-mediated neuromodulation.

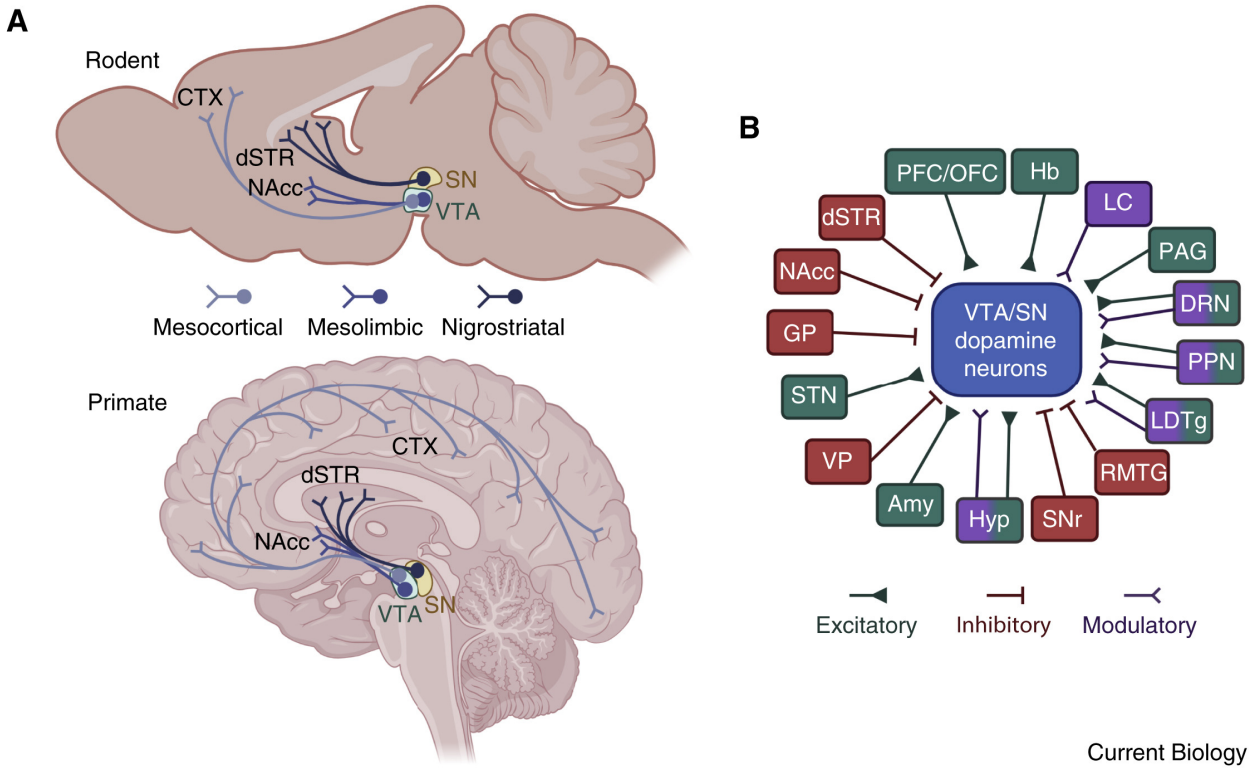

Figure 2. Anatomical connectivity of midbrain DA neurons. (**A**) Major projection pathways of DA neurons in mammals, illustrated using rodent and human brains as examples. Note the more extensive mesocortical pathway in primates. (**B**) Key brain regions that send direct projections to DA neurons in the VTA and SNpc. This list is not exhaustive but highlights the remarkable connectivity of midbrain DA neurons, reflecting their role in integrating diverse streams of information. **Abbreviations**: Amy, amygdala; DRN, dorsal raphe nucleus; dSTR, dorsal striatum; GP, globus pallidus; LC, locus coeruleus; LDTg, laterodorsal tegmental nucleus; Hyp, hypothalamus; Hb, habenula; OFC, orbitofrontal cortex; PAG, periaqueductal gray; PPN, pedunculopontine nucleus; RMTg, rostromedial tegmental nucleus; SN, substantia nigra; SNr, substantia nigra pars reticulata; STN, subthalamic nucleus; VP, ventral pallidum; VTA, ventral tegmental area. Figure from[28].

Functionally, the mesocorticolimbic DA system supports reinforcement learning, motivation, salience attribution, and adaptive behaviour[41]. Within cortical and hippocampal circuits, DA modulates synaptic plasticity mechanisms such as long-term potentiation (LTP) and long-term depression (LTD), thereby influencing learning and memory consolidation[32,42]. DA also regulates emotional states and stress responses; alterations in dopaminergic tone are associated to apathy, depression, and anxiety, frequently observed in prodromal AD stages[43,44]. Finally, DA cts as neuroimmune modulator, positioning its system as a key interface between neural and non-neural processes relevant to neurodegenerative diseases[26,27].

Several features render the mesocorticolimbic DA system particularly susceptible to pathological insults: its spontaneous firing activity, high metabolic demand, extensive axonal arborization, and limited antioxidant defences make neurons vulnerable to oxidative stress, mitochondrial dysfunction, and inflammation[27,45–48].

1.3.2 The Serotonergic System: Sources, Connections, and Functions

While the Dorsal Raphe Nucleus (DRN) serves as the primary source of serotonergic projections in widespread brain regions, including to the frontal cortex, the basal ganglia and the midbrain, the hippocampus also receives serotonergic inputs from the Median Raphe Nucleus (MRN) and the interpeduncular nucleus (IPN)[49–51]. Through this extensive innervation (**Figure 3**), 5-HT exerts a broad modulatory influence on mood regulation, cognitive flexibility, stress responsiveness, and synaptic plasticity[50,52–57].

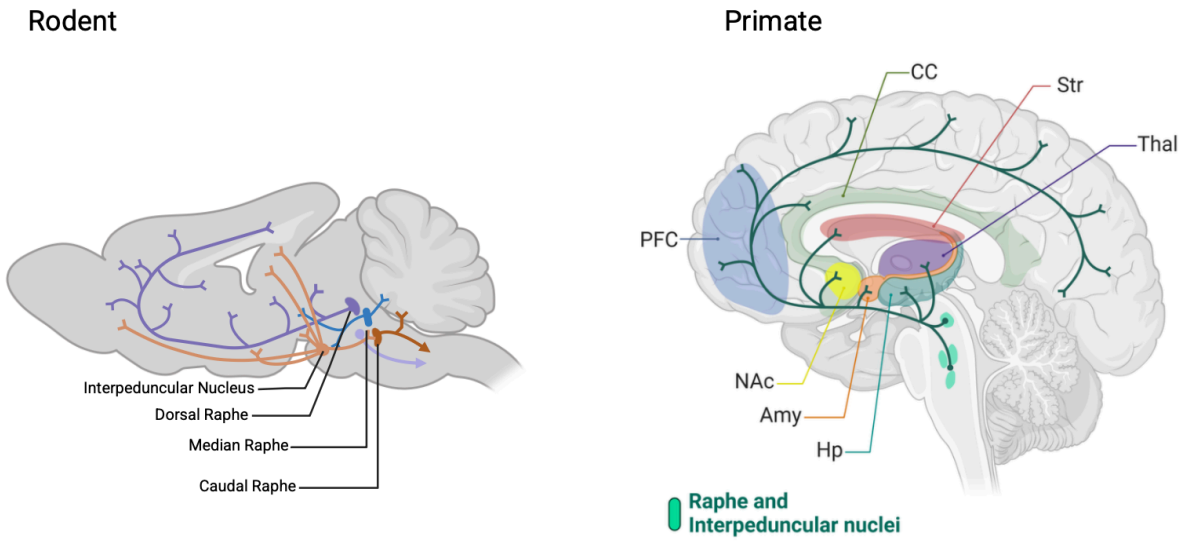

Figure 3: The neuroanatomy of the serotonergic system. The anatomical organization of the 5-HT system is highly conserved across vertebrate species. For example, rodents (*left*) show structures homologous to the human brain (*right*) The Raphe nuclei as well as IPN are interconnected with numerous cortical and subcortical regions. [Figure created using BioRender.com].

Serotonergic projections to the hippocampus are particularly relevant in the context of AD, as they modulate memory encoding, emotional behaviour, and neuroimmune interactions within a region that is highly vulnerable to early AD pathology. Unlike to fast synaptic neurotransmission, serotonergic signalling operates on slower temporal scales, shaping circuit excitability and homeostatic balance over extended periods[53,58–60].

Similar to dopaminergic systems, serotonergic neurons display features that confer increased vulnerability to pathological insults, including long axonal projections, high metabolic demand, and limited regenerative capacity. Consistent with these characteristics, early alterations of serotonergic nuclei have been reported early along the *AD continuum*, suggesting that serotonergic dysfunction may contribute to disease vulnerability during preclinical and prodromal stages.

1.3.3 Dopaminergic and serotonergic control of NLRP3 inflammasome in microglia

Neuroinflammation is increasingly recognized as a core pathogenic driver in AD, rather than a merely secondary response to protein aggregation[25,61–63]. Monoaminergic systems are not only

early targets of AD pathology but also potent regulators of immune homeostasis. Loss of these signalling may causally facilitate neuroinflammatory cascades, amplifying downstream tau pathology and cognitive decline[64,65]. Within this framework microglia − the principal innate immune cells of the central nervous system (CNS) − dynamically regulate synaptic remodelling, debris clearance, and tissue homeostasis. Under physiological conditions, microglial inflammatory pathways are tightly controlled, allowing these cells to act as immune sentinels without inducing chronic inflammation.

Among these pathways, the NOD-, LRR- and Pyrin domain-containing protein 3 (NLRP3) has emerged as a key component of microglial immune surveillance[66]. Rather than being constitutively active, NLRP3 functions as a sensor of cellular and metabolic homeostasis, responding to subtle danger-associated signals and intracellular stressors[67]. Controlled NLRP3 signalling supports beneficial microglial functions, including the clearance of noxious stimuli, localized cytokine release, and promotion of phagocytic activity, thereby contributing to tissue maintenance and neural circuit integrity. Importantly, this homeostatic activity operates within a narrow physiological range; ageing, metabolic stress, or early monoaminergic dysfunction may lower the activation threshold of NLRP3, shifting microglial responses from adaptive surveillance toward sustained inflammasome activation. Such dysregulation may represent a critical mechanistic link between early neuromodulatory deficits, chronic neuroinflammation, and the progression of AD pathology[66,68].

DA receptors on microglia and astrocytes allow DA to modulate neuroimmune activity, maintaining homeostasis in hippocampal and cortical regions[69–73]. DA modulates microglial activity through its receptors, particularly D1-like receptors (DRD1), which inhibit NLRP3 inflammasome activation[73]. DRD1 stimulation elevates cAMP and engages downstream signalling

pathways that prevent inflammasome assembly and caspase-1 activation, reducing interleukin-1β (IL-1β) release[65] (**Figure 4,** *top*).

Loss of DA input removes this inhibitory check-point, lowering the threshold for NLRP3 activation in response to amyloid or other stressors, thereby exacerbating hippocampal neuroinflammation and promoting tau hyperphosphorylation[65] (**Figure 4,** *bottom*).

Beyond its neuromodulatory role, 5-HT is also increasingly recognized as an important regulator of neuroimmune homeostasis. Serotonergic modulation of microglia and astrocytes is much more widespread and receptor-diverse, involving multiple receptor subtypes expressed across the CNS, including 5-HT_{1A}, 5-HT_{2B}, and 5-HT_{7}. Activation of these receptors can shape the balance between anti- (**Figure 4,** *top*) and pro- (**Figure 4,** *bottom*) inflammatory phenotypes and regulate cytochine production over extended networks[74–79]. Specifically, 5-HT_2B receptor activation in neonatal microglia is critical to limit neuroinflammation and prevent exaggerated inflammatory responses in adulthood[75]. Pharmacological enhancement of serotonergic signalling *via* selective 5-HT reuptake inhibitors (SSRIs) further attenuates microglial activation and reduces IL-1β and TNF-α production in experimental and clinical models[74,76,80,81].

Together, these findings indicate that dopaminergic and serotonergic signalling jointly regulate microglial responsiveness, set the inflammatory threshold, and control NLRP3 inflammasome activation.

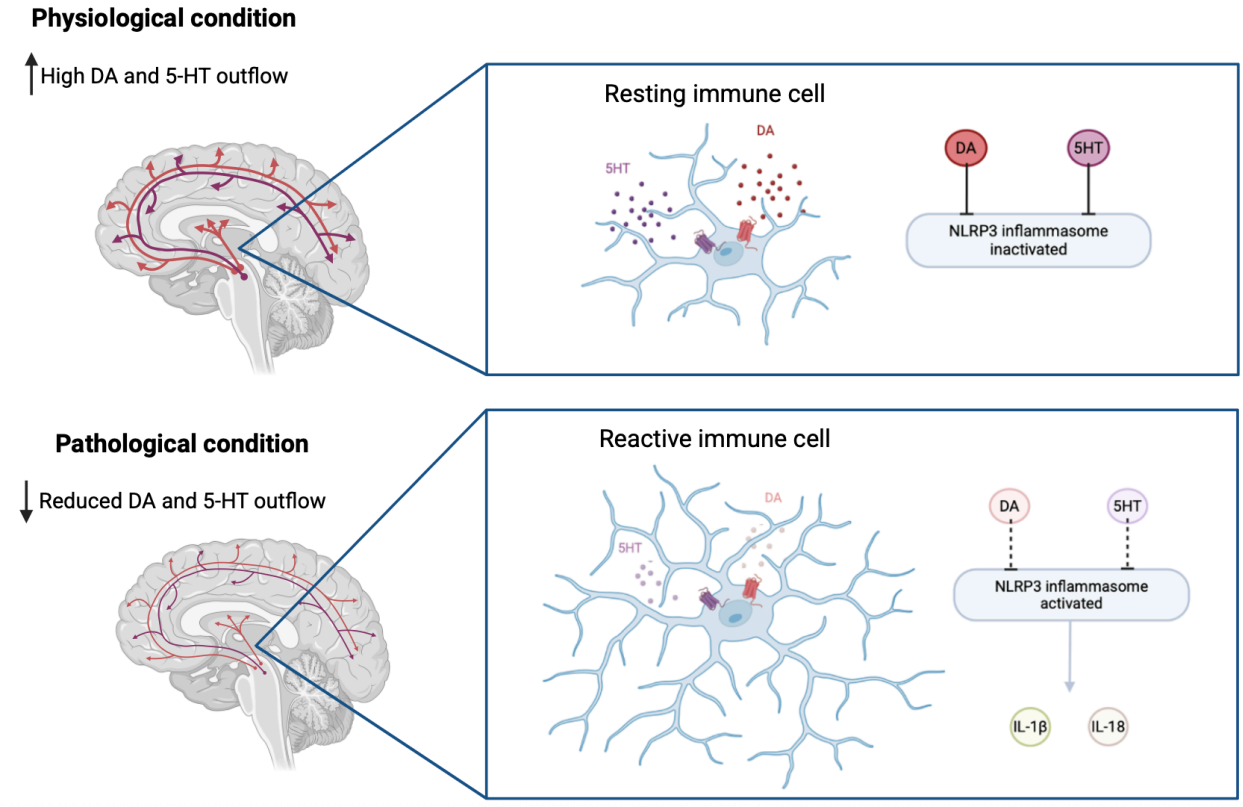

Figure 4. DA and 5-HT regulate microglial NLRP3 inflammasome activity. *Top*, under physiological conditions, high DA (**red**) and 5-HT (**violet**) *via* their receptors expressed on microglia and astrocytes regulate neuroimmune system in a homeostatic state, and maintain the NLRP3 inflammasome inactive in microglia. *Bottom*, under pathological conditions, reduced DA and 5-HT outflow and the consequent reduction in DA and 5-HT receptors signalling may exacerbate microglial activation, induce NLRP3 inflammasome activation and the release of the pro-inflammatory cytokines IL-1β and IL-18. [Figure created using BioRender.com].

1.4 Monoaminergic dysfunction in AD

1.4.1 Alterations of the midbrain dopaminergic system in AD

Although AD has historically been viewed as a cortico-hippocampal disorder primarily driven by amyloid and tau pathology, growing evidence indicates that subcortical neuromodulatory systems, particularly the dopaminergic system, are affected early and may actively contribute to disease progression[70,45,82–86]. Dopaminergic dysfunction is emerging as an upstream event influencing cognitive decline, neuropsychiatric symptoms, and neuroinflammatory processes[83,87,88].

Emerging evidence suggests that VTA dopaminergic neurons are affected early in AD, showing subtle structural and functional impairments prior to widespread neuronal loss[45,70,82,89]. Early

dopaminergic dysfunction may disrupt circuit homeostasis and amplify downstream pathological cascades, acting as a convergence point for cognitive, emotional, and immune-related deficits[26,30]. Experimental evidence from transgenic mouse models of AD, including Tg2576 and APP/PS1 lines, indicates that the mesocorticolimbic dopaminergic system is selectively and precociously affected during the disease progression. In particular, dopaminergic neurons of the VTA exhibit early structural and functional alterations, including neuronal atrophy, hyperexcitability, reduced DA synthesis, and impaired axonal projections toward limbic and cortical targets, occurring prior to extensive amyloid plaque deposition and widespread neurodegeneration[45,47,90,91]. These findings suggest that VTA dysfunction represents an early pathogenic event rather than a secondary consequence of cortical pathology.

Studies in AD mouse models, including Tg2576 and APP/PS1 lines, have demonstrated that VTA dopaminergic neuron loss is accompanied by reduced dopaminergic innervation in the hippocampus and prefrontal cortex, leading to impairments in synaptic plasticity, memory encoding, and motivational behaviours[45,82,91–93]. Importantly, selective experimental lesions of VTA dopaminergic neurons are sufficient to induce cognitive and behavioural deficits resembling early AD phenotypes, supporting a causal contribution of mesocorticolimbic DA dysfunction to disease-related symptoms[94]. Together, these data highlight the vulnerability of VTA dopaminergic circuits as a convergent node linking early molecular pathology to network-level dysfunction in AD.

Converging clinical evidence supports the notion that mesocorticolimbic dopaminergic dysfunction is already present in the earliest clinical stages of AD. Neuroimaging studies using structural MRI, PET, and functional connectivity approaches have revealed reduced VTA volume, altered dopaminergic signalling, and disrupted connectivity between the VTA and hippocampal-prefrontal networks in individuals with MCI and in cognitively unimpaired subjects at increased

risk for AD[83,95,96]. Moreover, several studies have shown that pharmacological manipulations aimed at increasing the dopaminergic transmission in the hippocampus and cortex could improve synaptic function, cognitive impairments and memory deficits in AD mouse model and patients[45,92,94,97–101]

Notably, reductions in VTA integrity and mesocorticolimbic functional connectivity correlate with episodic memory deficits, motivational impairment, and neuropsychiatric symptoms such as apathy and depression − features that frequently precede overt dementia[102–104]. Longitudinal studies further demonstrate that individuals presenting smaller midbrain volumes or greater baseline functional disconnection of dopaminergic circuits progress more rapidly from MCI to dementia[84,85,95,102]. Collectively, these findings indicate that dopaminergic dysfunction is an early and clinically relevant component of the *AD continuum*, with prognostic value for disease progression.

1.4.2 Serotonergic dysfunction in early AD

In addition to dopaminergic circuits, serotonergic systems have emerged as early and vulnerable targets along the *AD continuum*. Alterations in 5-HT-regulated functional domains – such as mood, cognitive flexibility, synaptic plasticity and stress responsiveness − are frequently observed in the earliest stages of AD, suggesting that a serotonergic dysfunction contributes to disease vulnerability.

Post-mortem and neuroimaging studies have documented degeneration of Raphe nuclei, reduced serotonergic fibre density, and decreased expression of specific 5-HT receptor subtypes in AD patients, with pathological changes detectable already at preclinical or prodromal stages[105,106]. In particular, reduced hippocampal 5-HT_{1A} receptors binding has been reported in AD, supporting an early disruption of serotonergic modulation within memory-related circuits[107]. Clinically,

serotonergic deficits are closely linked to the emergence of neuropsychiatric symptoms such as depression, anxiety, and apathy, which often precede overt cognitive decline and are associated with an increased risk of progression to dementia[108,109].

In the context of AD, serotonergic dysfunction may therefore act as a permissive factor that lowers the threshold for sustained neuroinflammatory activation in vulnerable brain regions such as the hippocampus. While dopaminergic signaling appears to exert a more direct inhibitory control over inflammasome activation, serotonergic tone may critically determine the inflammatory set-point of glial cells, modulating their responsiveness to Aβ accumulation, synaptic stress, and metabolic perturbations[25,61,110]. Supporting this view, enhancement of serotonergic signalling has been associated with reduced Aβ burden and slower pathological progression in both experimental models and clinical studies[107,111].

1.4.3 From monoaminergic dysfunction to disease mechanisms: an unresolved gap

Taken together, preclinical and clinical evidence indicates that early alterations in midbrain monoaminergic systems − particularly dopaminergic and serotonergic circuits − represent a common and clinically relevant feature of the *AD continuum*. Alterations in dopaminergic and serotonergic signalling have each been associated with changes in synaptic plasticity, network function, cognitive performance, neuropsychiatric symptoms, and immune regulation. Such dysfunctions may act as an upstream trigger for the dysregulation in the inflammatory cascade, promoting the initiation and amplification of neuroinflammation.

However, despite robust documentation of early monoaminergic vulnerability, the mechanistic pathways linking these neuromodulatory deficits to core AD pathologies remain incompletely understood. Indeed, how disruptions in these monoaminergic systems − individually or in combination − contribute to these processes remains incompletely understood. In addition, it is

still unclear whether degeneration of specific dopaminergic and serotonergic nuclei is sufficient to trigger inflammasome-mediated microglial activation, or instead synergizes with Aβ pathology to accelerate tau-related neurodegeneration, represents a critical unresolved question[25,112,113].

In AD, sustained exposure to Aβ and tau aggregates shifts microglia toward a chronically pro-inflammatory state[25,61]. In this process the NLRP3 inflammasome acts as a central hub, promoting caspase-1–dependent maturation of IL-1β and IL-18, thereby amplifying local and network-level inflammation[110]. Genetic deletion or pharmacological inhibition of NLRP3 in AD mouse models reduces microglial reactivity, amyloid and tau pathology, and rescues cognitive function, establishing a causal role for this inflammasome in the disease progression[110,112].

In this context, reduced DA and 5-HT release in target regions, especially the hippocampus, can act as an upstream trigger for microglial NLRP3 activation, establishing a feed-forward loop where monoamines dysfunction promote neuroinflammation, which in turn accelerates tau pathology and cognitive decline[65].

Although both monoaminergic dysfunction and NLRP3 activation have been independently implicated in AD, their mechanistic interplay remained underexplored.

The present work tests the hypothesis that selective degeneration of midbrain dopaminergic and serotonergic neurons is sufficient to initiate hippocampal NLRP3-driven neuroinflammation, thereby providing a causal link between early neuromodulatory deficits and accelerated AD pathology[110,112].Addressing this gap is essential to move beyond descriptive associations and toward a mechanistic understanding of how early midbrain monoaminergic dysfunction shapes vulnerability to AD.

2. Working Hypothesis

2.1 Background and Specific Aims

Although Aβ accumulation and tau pathology are defining molecular features of AD, growing evidence indicates that neuroinflammation mediated by microglial and astrocytic activation plays a central and active role in driving disease progression[112,114–116]. The concomitant presence of Aβ pathology, tau hyperphosphorylation, and neuroinflammatory markers constitutes one of the strongest predictors of cognitive impairment and conversion to dementia[117–119]. These observations support a model in which progression along the *AD continuum* preferentially occurs in Aβ-positive individuals who also exhibit sustained neuroinflammatory activation and tauopathy. However, the upstream mechanisms that initiate and shape this inflammatory response remain poorly defined.

Among the potential early triggers of neuroinflammation, brainstem monoaminergic systems have emerged as particularly vulnerable candidates[65,120–125]. Neuromodulatory nuclei, including the midbrain dopaminergic and serotonergic nuclei, exhibit early structural and functional alterations along the *AD continuum*. In particular, midbrain dopaminergic pathways show atrophy, reduced connectivity with cortical and limbic regions, hypometabolism, and neuroinflammatory changes detectable as early as the MCI stage[93,95,126–129]. These alterations are frequently accompanied by neuropsychiatric symptoms, including apathy, depression, and anxiety. Longitudinal studies indicate that reduced midbrain volumes or baseline functional disconnection of dopaminergic circuits predict faster progression to dementia[83,86,127,130–133]. Moreover, in cognitively unimpaired individuals, hippocampal volume and memory performance correlate positively with VTA integrity, highlighting the importance of mesocorticolimbic connectivity in sustaining cognitive function[95].

Despite this accumulating evidence, a critical gap remains. It is currently unclear whether early damage to midbrain monoaminergic nuclei merely reflects ongoing AD pathology or instead represents an upstream pathogenic event that directly triggers hippocampal neuroinflammation. In particular, whether selective depletion of dopaminergic and serotonergic input is sufficient to initiate inflammatory responses independently of pre-existing Aβ pathology has not been directly tested. Furthermore, the relative contribution of monoaminergic dysfunction *versus* amyloid burden in shaping hippocampal inflammatory activation and downstream AD-related pathology remains unresolved.

Based on these considerations, we hypothesize that early midbrain impairment represents an upstream pathogenic event that lowers the threshold for hippocampal neuroinflammation. In this framework, loss of monoaminergic tone is proposed to initiate or amplify NLRP3-inflammasome–mediated inflammatory cascades, which in turn promote tau hyperphosphorylation and accelerate the disease progression. Under normal conditions, dopaminergic signalling provides direct inhibitory control over NLRP3 inflammasome activation in microglia, while serotonergic tone establishes the inflammatory set-point of hippocampal glial cells, thereby modulating their responsiveness to pathological stressors such as Aβ accumulation, synaptic dysfunction, and metabolic stress. The reduction of these modulatory influences thus lowers the threshold for neuroinflammatory activation.

To test this hypothesis, we focused on the hippocampus, a key hub for cognition and memory that is strongly modulated by dopaminergic and serotonergic inputs[33,49,134,135] and is among the earliest brain regions affected in AD. We evaluated the effects of monoaminergic depletion induced by selective midbrain lesions of the VTA and SNpc for dopaminergic neurons, and the IPN for serotonergic neurons in both non-transgenic mice (C57BL/6N) and pre-plaque-stage Tg2576 mice, a validated AD model overexpressing the human APP carrying the Swedish mutation (APPSwe).

This experimental design allowed us to disentangle the effects of monoaminergic deprivation from those driven by Aβ pathology.

In non-transgenic mice, we investigated whether selective depletion of midbrain monoaminergic input is sufficient to induce hippocampal neuroinflammation by assessing i) microglial reactivity and IL-1β release mediated by the NLRP3-inflammasome pathway, and ii) whether pharmacological restoration of monoaminergic tone using dopaminergic (L-DOPA and A-68) or serotonergic (fluoxetine) treatments could suppress these inflammatory responses.

In Tg2576 mice, we examined whether combined monoaminergic depletion accelerates the progression of AD-like pathology by analysing i) microglial and astrocytic reactivity, ii) Aβ accumulation, and iii) tau phosphorylation. Finally, we assessed whether restoring monoaminergic signalling could mitigate the hyper-inflammatory phenotype and attenuate the acceleration of AD-related pathology.

Through this approach, the present work aims to establish a causal link between early midbrain monoaminergic dysfunction and hippocampal NLRP3-driven neuroinflammation in AD progression, thereby identifying neuromodulatory systems as potential early therapeutic targets for delaying or preventing cognitive decline.

The results described herein led to a peer-reviewed publication[136] where I share first authorship, reflecting my primary role in the experimental design and execution of the study.

3. Material and Methods

3.1 Animals

Experiments complied with the ARRIVE procedures and the ethical guidelines of the European Council Directive (2010/63/EU). Experimental approval was obtained from the Italian Ministry of Health. Male and female C57BL/6N (Charles River, Italy) and female B6.129P2(Cg)-Cx3cr1^{tm1Litt}/J ($CX_3CR\text{-}1^{GFP}$ knock-in/knock-out; Jackson Laboratory Strain #:005582) mice were used at 2-3 months of age. Heterozygous male Tg2576 mice (Taconic #APPSWE - Model 1349 tg/wt; 41) and their Wild-Type (WT) littermates (mice with the same strain and genetic background of Tg2576, negative for APPSWE overexpression - Taconic #APPSWE - Model 1349 wt/wt) were used at 6-7 months of age.

All mice were housed with *ad libitum* food and water, with a 12 h light/dark cycle. Mice were housed in cages of 3-4 individuals and all cages were equipped with the same environmental enrichment.

3.2 Stereotaxic injections

Mice were anaesthetized with Rompun (20 mg/mL, 0.5 mL/kg; Bayer) and Zoletil (100 mg/mL, 0.5 mL/kg; Virbac; intraperitoneally i.p.) and positioned in a stereotaxic apparatus.

For Caspase-3 (Casp3) mice (C57BL/6N, $CX_3CR\text{-}1^{GFP}$ or Tg2576 mice), we infused a mix of Adeno-Associated Viruses (AAVs; 0.5 µL each, flux 80 nL/min[138]: (i) AAV1-THp-iCre ($5x10^{12}$ viral particles/mL; Vector Biolabs) and (ii) AAV5-flex-taCasp3-TEVp ($4.2x10^{12}$ viral particles/mL; UNC Vector core, gift from Nirao Shah) in the left VTA (AP: -3.2, ML: -0.35, DV: -4.4; 43), to lesion Tyrosine Hydroxylase-positive (TH^+) neurons in the VTA and Substantia Nigra

pars compacta (SNpc) and 5-HT$^+$ neurons in the interpeduncular nucleus (IPN). Sham mice were injected only with the AAV1-THp-iCre virus.

In a separate cohort of C57BL/6N mice, the AAV1-THp-iCre + AAV5-flex-taCasp3-TEVp mix (0.125 µL each, flux 25 nL/min) were injected in the IPN (thereafter: Casp3^{IPN}; AP: -3.5, ML: 0, DV: -4.7; 43) to lesion the 5-HT$^+$ neurons of the IPN while leaving intact the TH$^+$ neurons of the VTA/SNpc. Sham mice were injected only with the AAV1-THp-iCre virus (Sham^{IPN}).

For 6-hydroxy-dopamine (6OHDA) lesion (C57BL/6N mice), 6OHDA (Sigma-Aldrich; 7.6 mg/mL, calculated as free-base) was dissolved in 0.2 mg/mL ascorbic-acid (Tocris) prepared in 0.9% saline, and continuously kept on ice. Each mouse was injected with 2.5 µg in 0.4 µL (flux 40 nL/min) unilaterally in the left VTA. Thirty minutes before surgery, mice received 10 mL/kg (2.85 mg/mL as free base, i.p.) of the norepinephrine (NE) reuptake-inhibitor desipramine-hydrochloride (Sigma-Aldrich), to prevent NE fibre degeneration. Control mice were injected with Saline.

C57BL/6N and $CX_3CR\text{-}1^{GFP}$ mice received the intracerebral injection at 2 months of age. Tg2576 mice were injected at 6 months of age. All mice were used 30 days following injection to ensure steady-state lesion.

For all infusions we used 1 µL Hamilton syringes (Model Neuros7001) mounted on a Pump-11 Elite Nanomite (Harvard Apparatus). When possible, the accuracy of the injection site was controlled by immunofluorescence analysis; mice with misplaced injection were excluded.

3.3 Drug treatments

Animals were injected with L-DOPA (i.p., 10 mg/kg; Sigma-Aldrich) plus benserazide (12 mg/kg; Sigma-Aldrich [134], or with A68930-hydrochloride (5 mg/kg; Santa Cruz), once a day for 4 or 7

days, respectively; 0.9% saline was used as control (vehicle); experiments were performed 1h after the last injection.

Fluoxetine-hydrochloride (30 mg/kg; Tocris) was dissolved in water and delivered *ad libitum* in drinking bottles wrapped in tin-foil for 30 days, starting immediately after surgery. Normal drinking water was used as control.

3.4 Immunofluorescence

Anaesthetized mice (Rompun/Zoletil) were transcardially-perfused with phosphate buffer (PB; 0.1 M, pH 7.4) followed by 4% paraformaldehyde in PB. Brains were postfixed in 4% paraformaldehyde for at least 4h, dehydrated and cryoprotected in 30% sucrose in PB at 4°C until sinking. Thirty µm-thick coronal sections were cut with a cryostat, and slices were collected in PB-Sodium Azide 0.02%. All analyses were performed in the left hemisphere, ipsilateral to the lesion.

Slices were incubated with primary antibodies in PB containing 0.3% Triton X-100 overnight at 4°C for TH, Iba1, GFAP, hippocampal 5-HT transporter (SERT) staining, or 3 nights for IL-1β/Iba1, IL-18/Iba1, IL-18 Receptor (IL-18R)/GFAP, p-Nuclear Factor kappa B (NFκB)/S100β and Microtubule-Associated Protein 2 (MAP2).

For 5-HT, slices were incubated with primary antibodies in PB containing 0.5% Triton X-100 and 10% donkey-serum for 2 nights at 4°C.

For hippocampal TH^+/NE transporter-positive (NET^+) fibres, sections were incubated in citrate buffer (10 mM Sodium-citrate, pH 6.0 containing 0.05% Tween-20; 20 min, 75°C), rinsed in PB, immersed in blocking solution (5% donkey serum, 0.2% Triton X-100 in PB; 1h, RT), and incubated with primary antibody in the same solution (overnight at 4°C; [140].

For NLRP3/Iba1/GFAP staining and NLRP3/Iba1 staining, sections were pretreated with 50% methanol (15 min, RT) immersed in blocking solution (3% bovine serum albumin, 0.1% Triton X-100 in PB, 30 min, RT) and incubated with primary antibodies in PB with 0.1% Triton X-100 (2 nights, 4°C).

For Iba1/CD68, slices were permeabilized using 0.5% Triton X-100 in PB (45 min, RT), incubated in blocking solution (2% bovine-serum albumin, 0.5% Triton X-100 in PB, 1h, RT) and exposed to primary antibodies in blocking solution (2 nights, 4°C).

For C3/GFAP, slices were immersed in blocking solution (5% donkey serum, 0.1% Triton X-100 in PB; 1 h, RT) and then incubated with primary antibodies in 1% donkey serum, 0.1% Triton X-100 in PB (overnight, 4°C).

For C3aR/Iba1/NeuroTrace analysis slices were incubated in blocking solution (3% BSA, 5% goat serum, 0.5% Triton X-100 in PB; 1 h, RT) and then with primary antibodies in blocking solution (overnight, 4°C).

For tau staining, slices were pretreated with 50% methanol (15 min, RT), immersed in blocking solution (3% bovine serum albumin, 0.1% Triton X-100 in PB with M.O.M.® (Mouse on Mouse) Blocking Reagent (1:1000; Vector laboratories, #MKB-2213-1, 2h, RT) and then incubated with primary antibodies in 0.1% Triton X-100 in PB (2 nights, 4°C).

For Aβ staining, sections were pretreated with M.O.M.® (1:1000; 2 h, RT) diluted in permeabilization solution (PB with 0.3% Triton X-100) and incubated with primary antibodies overnight at 4°C in permeabilization solution.

For every immunofluorescence protocol, after primary antibody, slices were incubated with secondary antibodies in the same solution of primary antibody (2 h, RT) and counterstained with Blue-Fluorescent Nissl-Stain (NeuroTrace 1:200; Invitrogen) or DAPI (1:1000, Serva).

After mounted, slices were examined using a Nikon Eclipse Ti2 confocal microscope. The labelling specificity was confirmed by omission of primary antibodies and use of normal serum instead (negative controls). For quantitative analysis, images were processed simultaneously and analysed with Fiji-ImageJ (http://imagej.nih.gov/ij/): after 8-bit conversion and background subtraction, the signal was quantified by measuring the relative fluorescence intensity. The F/A ratio defines mean fluorescence intensity (F) over surface area (A).

For analysis of fibre density and intensity, and protein levels, images were acquired with a 20x-objective by Z-stacks, then processed by maximum-intensity projection. All samples were captured with identical Z-stack thickness and laser settings within each analysis.

$TH^+/DAT^+/SERT^+$ fibre intensity was quantified by setting 16 frames (100x100 pixel). The total fibre number per 250 μm was counted manually[141,142].

CD68, NLRP3, IL-1β and IL-18 protein levels were measured within $Iba1^+$ cells.

Automated total cell counts and analysis of overlapping regions between markers to assess colocalization were performed in Imaris XT software (Bitplane AG, Oxford Instruments, Abingdon-on-Thames, UK). For all double-positive cell counting analyses, the Surfaces function was used. Briefly, after applying background subtraction and automatic thresholding, to retain only objects within lower and upper threshold limits, and splitting of touching objects to separate individual cells, colocalization between markers was quantified using the Overlapped Volume Surfaces option. Complement component 3 (C3) levels were quantified within $GFAP^+$ cells, while MAP2 intensity was quantified by setting 12 frames (90x90 pixel) over the stratum radiatum. Intracellular Aβ levels were quantified by setting 10 randomly-distributed frames on the hippocampal CA1 pyramidal layer (70x70 pixel).

To analyse the number of Aβ plaques and the $AT8^+$ area in the hippocampus, we acquired Z-stack large images with a 20x-objective. The mean number of $6E10^+$ plaques in the hippocampus from

at least 3 slices/animal was quantified. To calculate $AT8^+$ area, the hippocampus was manually defined, and automatic brightness thresholding was used to delineate the positive area. Hippocampal $AT8^+$ area was expressed as ratio of total area analysed in each slice/animal (modified from 47). Intracellular AT8 levels were quantified by Z-stack with 60x-oil objective and by setting 1 frame (20x20 pixel).

For all analysis, quantification was done on 4 slices/mouse. Data were then averaged per mouse for figures and statistical analysis.

Primary antibodies: 5-HT (1:500; ImmunoStar #20080; RRID:AB_572263), AT8 Ser202/Thr205 (1:200; Invitrogen #1020; RRID:AB_223647), C3 (1:300; Novus Biologicals #NB200-540; RRID:AB_2744548), C3aR (1:200, HycultBiotech #HM3028; RRID:AB_2131309), CD68 (1:400; Biorad #MCA1957; RRID:AB_322219), DAT (1:400; Chemicon #MAB369; RRID:AB_2190413), GFAP (1:1000; Millipore #AB5804; RRID:AB_2109645), GFAP (1:1000; DAKO #Z0334; RRID:AB_2314535), hAPP695 (6E10; 1:500, BioLegend #803001; RRID: AB_2564653), IBA1 (1:600; Wako #019-19741; RRID:AB_839504), AIF-1/Iba1 (1:600; Novus Biologicals #NB100-1028; RRID:AB_3148646), IL-1β (1:200; R&D #AF-401-NA; RRID:AB_416684), IL-18 (1:300; MBL #D047-3; RRID:AB_592016), IL-18Rα/IL-1 r5 (1:100; R&D #AF856; RRID:AB_355664), MAP2 (1:500; Invitrogen #MA5-12826; RRID:AB_10976831), NET (1:500; Atlas Antibodies #AMAb91116; RRID:AB_2665806), NLRP3 (1:200; Adipogen #AG-20B-0014; RRID:AB_2490202), p-NFκB (Ser536) (1:200; Cell Signaling #3033; RRID:AB_331284), S100β (1:500; SYSY #287 006; RRID:AB_2713986), SERT (1:500; Millipore #PC177L; RRID:AB_2122553), TH (1:1000; Millipore #MAB318; RRID:AB_2201528), TH (1:500; Millipore #AB152; RRID: AB_390204).

Secondary Antibodies (ThermoFisher): Alexa Fluor-488 donkey anti-rabbit (1:200; #A-21206; RRID:AB_2535792), Alexa Fluor-555 donkey anti-rabbit (1:200; #A31572; RRID:AB_162543),

Alexa Fluor-647 goat anti-rabbit (1:200; #A-31573; RRID:AB_2536183), Alexa Fluor-488 donkey anti-mouse (1:200; #R37114; RRID:AB_2556542), Alexa Fluor-555 donkey anti-mouse (1:200; #A31570; RRID:AB_2536180), Alexa Fluor-488 donkey anti-rat (1:200; #A21208; RRID:AB_2535794), Alexa Fluor-647 goat anti-rat (1:200; #A-21247; RRID:AB_141778), Alexa Fluor-488 donkey anti-goat (1:200; #A-11055; RRID:AB_2534102), Alexa Fluor-647 donkey anti-goat (1:200; #A-21447; RRID:AB_141844), Alexa Fluor-555 goat anti-chicken (1:200; # A-21437; RRID:AB_2535858).

Exclusively for the representative confocal images, after the quantitative analysis, LUTs were equally increased at the same level for all groups of a given experiment. Quantitative analyses were performed on raw images.

3.5 Stereology

Immunofluorescence sections were used to estimate i) TH^+ neurons in the left SNpc, VTA and *Locus Coeruleus* (LC), ii) 5-HT^+ neurons in the entire Interpeduncular Nucleus (IPN); iii) 5-HT^+ neurons in the dorsal and medial Raphe; iv) $Iba1^+$ and $GFAP^+$ cells in the hippocampus. The area boundaries for VTA/SNpc/LC were defined by TH, the IPN/dRaphe/mRaphe by 5-HT, the hippocampus by DAPI staining, using the 5x-objective, in accordance to Paxinos guidelines[139].

We applied an optical fractionator stereological design using the Stereo Investigator System (MBF Bioscience). A stack of MAC5000 controller modules (Ludl Electronic Products, Ltd) was interfaced with a Zeiss Microscope Axio Imager KMAT with a motorized stage and a Zeiss Axiocam 506 mono with Working High End PC. A 3D-optical fractionator counting probe (x, y, z dimension 50×50×25 μm for TH^+ neurons, 70×70×25 μm only for 5-HT^+ neurons and 100×100×25 μm for glia cells) was applied. Cells were marked with a 100x-oil-(VTA/SNpc) or a 40x-objective (neurons in LC/IPN/dRaphe/mRaphe; glia cells in hippocampus).

The total cell number was estimated according to the formula (Equation 1):

$$N = SQ \times (1/ssf) \times (1/asf) \times (1/tsf) \quad (1)$$

where SQ represents the cell number counted in all optically sampled fields of the ROI, ssf is the section sampling fraction, asf is the area sampling fraction and tsf is the thickness sampling fraction.

3.6 Morphological analysis

Microglia were imaged with a Zeiss Microscope Axio Imager KMAT with motorized stage and a camera connected to Neurolucida software (7.5v; MBF Bioscience) for quantitative 3D-analysis of the entire cell[90,142]. Only non-overlapping cells that showed clear soma and branching were analysed. Soma area and perimeter were measured; Sholl analysis included counting the number of dendritic intersections, nodes and endings, and dendritic lengths at fixed distances from the soma in 10 μm-spaced concentric circles originating from the soma. Analysis was done with 100x-oil objective. Nine representative cells/animal were analysed randomly, and data were averaged for each mouse.

3.7 Total protein extraction and Western-blot analysis

The ipsilateral hippocampus was dissected from the entire brain and stored at -80°C until the day of the experiment. Tissue was homogenized in RIPA buffer containing (in mM): 50 Tris-HCl pH 7.5, 150 NaCl, 5 $MgCl_2$, 1 EDTA, 1% Triton X-100, 0.25% sodium deoxycholate, 0.1% SDS, 1 sodium-orthovanadate, 5 b-glycerophosphate, 5 NaF and protease inhibitor cocktail; samples were then sonicated four times (five strokes of 0.5 pulse/s) and incubated on ice for 30 min[48]. Samples were centrifuged (13000 g, 20 min, +4°C) and the supernatant's protein concentration was determined by the Bradford method. Proteins were applied to SDS-PAGE and electroblotted on a

polyvinylidene-difluoride membrane. Blotting analysis was performed using a chemiluminescence detection kit. The relative levels of immunoreactivity were determined by densitometry using ImageJ.

Primary antibodies: Glycogen Synthase Kinase 3β (GSK3β; 1:1000, Cell Signaling Technology; #9832s; RRID: AB_10839406); p-GSK3β (Ser9) (1:1000, Cell Signaling Technology; #9336s; RRID: AB_331405); JNK (1:1000, Cell Signaling Technology; #9252s; RRID: AB_2250373); p-JNK (Thr183/Tyr185) (1:1000, Cell Signaling Technology; #9251s; RRID: AB_331659); p-p38 (Thr180/Tyr182) (1:1000, Cell Signaling Technology; #4511s; RRID: AB_2139682); p38 (1:1000, Cell Signaling Technology, #8690s; RRID: AB_10999090); β-Tubulin (1:1000, Biolegend; #801201; RRID: AB_2313773). All primary antibodies were incubated overnight except for β-Tubulin (2 h).

Secondary antibodies: goat anti-mouse IgG (1:3000; Bio-Rad; #1706516; RRID: AB_11125547), goat anti-rabbit IgG (1:3000; Bio-Rad; #1706515; RRID: AB_2617112).

Membranes were stripped using Re-Blot Plus Strong Solution (Millipore; 15 min, RT). Both groups (Shan *vs* Casp3; Tg Sham *vs* Tg Casp3) were analysed simultaneously.

3.8 Microglia sorting, RNA isolation and RNA-sequencing

3.8.1 Microglia sorting

Hippocampus from Sham and Casp3 $CX_3CR\text{-}1^{GFP}$ mice (Sham: n = 3; Casp3: n = 5 mice) was dissociated into single-cell suspensions using Adult Brain Dissociation kit (Miltenyi Biotec, #130-107-677) according to the manufacturer's instructions. Briefly, each mouse was transcardially perfused with 1x $D\text{-}PBS^{+/+}$. The hippocampus of each Sham or Casp3 $CX_3CR\text{-}1^{GFP}$ mouse was isolated and added in half brain of a C57BL/6N mouse, to increase the quantity of tissues to dissociate. Tissues were then cut into small pieces and enzymatically and mechanically dissociated

on the gentle MACS Octo Dissociator with Heaters (Miltenyi Biotec, #130-096-427) using the 37C_ABDK_01 program. Following dissociation, samples were resuspended and passed through a prewet 70 µm MACS SmartStrainer (Miltenyi Biotec, #130-110-916,) and centrifuged at 300 *g* for 10 min at 4°C. Following centrifugation, the supernatant was discarded, and the debris were removed using the Debris Removal solution (Miltenyi Biotec, #130-109-398) provided by the kit. Finally, cells were resuspended in 100 µL of Running Buffer and stained for 30 min at 4°C protected from light with the following antibodies: CD11b Monoclonal Antibody (M1/70) PE-Cyanine7 (1:100; Invitrogen, #25-0112-82; RRID: AB_469588) and PerCP anti-mouse CD45 Antibody (1:100; BioLegend #103130; RRID: AB_893339). To exclude dead cells, LIVE/DEAD Fixable Aqua Dead Cell Stain Kit (1:100; Invitrogen, #L34957) was used. Cells were washed with Running Buffer and pelleted at 1000 *g* for 10 min at 4°C. Then, cells were resuspended in 400 µL of Running Buffer. Afterward, the samples were taken to FACS and the gating strategy was set to $CD11b^{+}CD45^{+}eGFP^{+}$ for isolation of microglia from Sham or Casp3 $CX_3CR\text{-}1^{GFP}$ hippocampi. The sorting purity was to be approximately 97%.

3.8.2 RNA extraction and mRNA-Seq

Total RNA from isolated microglia was purified *via* the spin-colum based "Total RNA purification Plus Micro Kit" (Norgen Biotek, #48500), following the manufacturer instructions.

Low-input mRNA-Seq was performed by Igatech Service (Udine, Italy). Briefly, RNA samples were quantified, and quality tested by TapeStation RNA assay (Agilent Technologies). Libraries were generated using the Ovation SoLo RNA-seq Library Preparation kit (Tecan Genomics) following the manufacturer's instructions. Final libraries were checked with Qubit 3.0 Fluorometer (Invitrogen) and Agilent Bioanalyzer DNA assay. Libraries were then barcoded for multiplexing and sequenced on paired-end 150 bp mode on NovaSeq 6000 (Illumina) at a depth of 30 million

reads. Base calling and demultiplexing were performed with Illumina BCL Convert v3.9.31. Lower quality bases and adapters were removed by Cutadapt v1.11 software[144]. Reads were aligned on reference GRCm39.112 genome with STAR using default parameters[144]. Assembling and quantitation of full-length transcripts representing multiple spliced variants for each gene locus was performed by Stringtie[145] using default parameters.

Differentially expressed genes (DEGS) were identified with DESeq2[146]. The ToppGene suite was used with default settings to identify functional enrichment in the DEG lists (http://toppgene.cchmc.org).

3.9 High performance liquid chromatography (HPLC)

Quantification of hippocampal monoamines (DA, 5-HT, NE), and relative metabolites (DOPAC and HVA for DA, 5-HIAA for 5-HT, MOPEG for NE) was performed using a HPLC system (UltiMate® 3000, ThermoFisher) coupled with Coulochem electrochemical detection (6011RS Ultra Coulometric Analytical Cell, ThermoFisher). After animal sacrifice, the left hippocampus was rapidly dissected on ice and immediately stored at -80°C until analysis. On the day of analysis frozen samples were homogenized on ice with 0.05M $HClO_4$ and antioxidant solution (containing in mM: 0.27 Na_2EDTA, 100 acetic acid, 0.0125 ascorbic acid) in a 4:1 ratio. The homogenate was mechanically lysed, sonicated on ice and centrifuged (10000 rpm, 20 min, 4°C). The supernatant was transferred into a new tube and the pellet was weighed. 20 µL of each sample were injected onto the HPLC-ECD (run-time: 60 min; flow-rate: 0.6 mL/min). Standards of each metabolite were prepared fresh on the day with same solutions and quantities as for tissue samples. The chromatographic separation was performed on a Hypersil GOLD aQ-C18 column (150×3 mm, 5 µm) fitted with an aQ-C18 drop-in guard pre-column (10×3 mm, 5 µm) maintained at 37°C. The

mobile phase consisted of 5% methanol and buffer solution (0.1 M Na-Phosphate, 0.1 mM Titriplex® III and 0.5 µM 1-Octanesulfonic-Acid Na-salt, pH 3.6 adjusted with 85% Ortho-Phosphoric-acid), filtered through a 0.22 µm cellulose-ester membrane (Millipore). The potential applied to both dual-inline flow-through micro-porous graphitic carbon-working electrodes was set at +450 mV, with 1 nA-gain for ECRS1 and 10 nA-gain for ECRS2. The chromatograms were integrated with Chromeleon™ Software (7.0v; ThermoFisher). The sample concentration of metabolites was calculated from the corresponding peak height, normalized to the pellet weight.

3.10 Brain slicing and electrophysiology

Following anaesthesia, mice were decapitated and the brain was rapidly removed; 300 µm-thick parasagittal slices containing the left dorsal hippocampus were cut (Leica VT1200S vibratome) in oxygenated (95% O_2, 5% CO_2) ice-cold sucrose-based solution (in mM: 3 KCl, 1.25 NaH_2PO_4, 26 $NaHCO_3$, 10 $MgSO_4$, 0.5 $CaCl_2$, 25 glucose, 185 sucrose; ~300 mOsm, pH 7.4). Brain slices were left to recover in artificial Cerebro-Spinal Fluid (aCSF; containing in mM: 124 NaCl, 1.25 NaH_2PO_4-H_2O, 26 $NaHCO_3$, 3 KCl, 10 Glucose, 1 $MgSO_4$, 2 $CaCl_2$, ~300 mOsm, pH 7.4) at 32-34°C for 40 min, and moved at RT for at least 30 min before recording[147].

For recording, each slice was placed under an Olympus BX51WI microscope and perfused with oxygenated aCSF (3-4 mL/min, 30-32°C). The hippocampus was visualized with infrared differential-interference-contrast at 4x.

Recordings were performed using a MultiClamp700B amplifier, digitized with Digidata1550B and computer-saved with pClamp11 (Molecular Devices). Patch-pipettes (3-5 MΩ), filled with aCSF, were pulled from TW150F-4 glass tubes (WPI). Field excitatory postsynaptic potentials (fEPSPs), recorded in the stratum radiatum, were induced with Schaffer collateral stimulation (100 µs), acquired at 20 kHz and filtered off-line with a 10 kHz low-pass Bessel filter. Input-Output (I/O)

curves of fEPSP slopes were obtained at 10 μA-stepped increasing stimulation every 30 s. The Paired-Pulse Ratio (PPR) was evaluated with pairs of stimuli (20-1000 ms interval), at half-maximal stimulation. For Long-Term Potentiation (LTP), after 20 min of test stimulation (half-maximal intensity, every 30 s) to assess slope stability, the slice was challenged with two trains at 100 Hz (1 s duration, 20 s interval) followed by test stimulation for 1h. The LTP magnitude was evaluated as the fEPSP mean slope at 60 min after the conditioning trains, normalized to the mean baseline slope [45,140,141]. To assess the effect of the IL-1β receptor antagonist (IL-1β-Ra) on LTP, slices were pre-incubated with IL-1β-Ra (100 ng/mL, from freshly-thawed stock in PBS/BSA 0.1%; R&D Systems) in oxygenated aCSF for 1 h and recorded as above.

Coronal slices (240 μm-thickness) were used for spine density analysis. CA1 pyramidal neurons were filled with biocytin during whole-cell patch clamp. Freshly weighted biocytin (0.2%; Tocris) was added to intracellular solution containing (in mM): Cs-methanesulfonate 120, CsCl 15, NaCl 8, HEPES 10, EGTA 0.20, TEA-Cl 10, QX314-Cl 5, Mg-ATP 2, Na-GTP 0.3 (~275–285 mOsm, pH 7.4). Patch-pipettes used for cell filling had a tip resistance of 4-10 MΩ and a minimum filling time of 10 min was used for each cell. Access resistance was monitored throughout this time to check for accessibility to the cytoplasm. To avoid cell damage after filling, the electrode was removed from the slice by establishment of an outside-out patch.

3.12 Spine density analysis

For analysis of biocytin-filled neurons, slices bearing neurons loaded with biocytin were fixed by immersion in 4% paraformaldehyde in PB overnight (4°C). Then, slices were washed three times in PB and incubated with Streptavidin (Thermo Fisher #S32355, Alexa Fluor 555-conjugated RRID:AB_2571525) and Green-Fluorescent Nissl-Stain (NeuroTrace 1:600; Invitrogen #N21480) in PB containing 0.3% Triton X-100 (overnight, 4°C).

The z-stack confocal images were captured using Nikon Eclipse Ti2 confocal microscope with 60x-oil objective and 4.5 digital zoom. We analysed spines in distal (terminal) apical dendrites. Spine density was assessed by counting the number of spines in at least 18 segments per neuron (4 cells, 5 animals per experimental group) chosen in branch orders 2–4 of apical dendrites extending for an additional 30-60 μm away from the starting point[148]. Imaris software (9.8.2) was utilized to create 3D reconstructions of dendritic segments using the Filaments tool. The settings used for all reconstructions is the same as in [149]. An observer blinded to the experimental groups manually edited the reconstructions to include or exclude misidentified spines.

3.13 Behavioural Testing

All behavioural tests were conducted between 09:00 a.m. and 4:00 p.m. Mice were habituated to the experimenter through daily handling sessions for one week prior to the onset of behavioural testing. In addition, animals were acclimated to the testing room for one hour immediately before the start of each experimental session.

To minimize potential olfactory interference, the chambers and objects were cleaned between animals and/or sessions using a 5% ethanol solution.

3.13.1 Open Field and Novel Object Recognition (NOR) Tests

Testing was performed in a dimly-lit (25 lux) plexiglass open field arena (60×60×30 cm), with dark-grey walls and white floor. On Day1 (D1), each mouse was placed in the arena centre and allowed to freely-explore for 10 min, during which movements were recorded. We analysed the time spent (s) in the arena centre and periphery, and the total distance travelled. Thereafter, we conducted the NOR test, consisting of habituation, training and testing[90]. During habituation, mice were familiarized with the empty arena for 10 min (D2). 24 h later (D3), mice were trained for 10

min by exposure to two identical objects (yellow wooden spheres) placed in the arena center. Mice were then returned to their home cage. Following 24 h (D4), mice were returned to the arena for the test session (10 min), during which one object was replaced by a novel object (a light-grey wooden cone). In both the training and testing sessions the animals were left to freely-explore the objects, and the exploration time was recorded, calculated as the time when they touched or climbed on an object or sniffed it at a distance of at least 2 cm. The Object Discrimination Ratio (ODR) was calculated using the following formula (Equation 2):

$$ODR = \frac{\text{Time exploring the novel object}}{\text{Time exploring novel object + Time exploring familiar object}} \text{ x } 100 \quad (2)$$

Objects were randomized and counterbalanced across groups.

3.13.2 Spatial Object Recognition (SOR) Test

The SOR test was conducted in the same circular arena previously described for the open field and NOR tasks. For this test, a high-contrast black-and-yellow striped cue was affixed to the inner wall of the arena to provide a visual local cue and enhance spatial orientation. Each mouse was tested individually across five consecutive 6-min sessions, with each session separated by a 3-min inter-trial interval in the home cage. In all sessions, animals were placed into the arena from the same starting location (protocol adapted from[150,151].

During session 1 (S1), mice were allowed to freely explore the empty apparatus, enabling familiarization with the environmental context and distal cues in the absence of objects. During sessions 2 to 4 (S2-S4), mice were exposed to four distinct objects (A-D) placed in fixed positions to allow the animals to encode the spatial configuration (habituation phase). The objects differed in shape, size, and material to promote discrimination and reduce object bias: (A) a yellow wooden ball, (B) a gray metal column, (C) a light-grey wooden cone, and (D) a glass jar with a perforated red cap.

Habituation to the spatial configuration was assessed by averaging the duration of contact with the four objects during sessions 2, 3, and 4 for each experimental group to provide an index of general exploratory activity. Object exploration was defined as the total time (s) the animal spent with its snout either in direct contact with the object or within approximately 2 cm of it.

Session 5 (S5) involved a spatial rearrangement: object A was moved to the previous location of object B, object B was placed in a novel, unoccupied position, while objects C and D remained in their original locations. This configuration was used to assess spatial novelty detection based on differential exploration of Displaced Objects (DO) *versus* Non-Displaced Objects (NDO), using the following formula (Equations 3 and 4):

$$\mathrm{DO}\ [\mathrm{S5}] - \mathrm{DO}\ [\mathrm{S4}] = \mathrm{DO} \quad (3)$$

$$\mathrm{NDO}\ [\mathrm{S5}] - \mathrm{NDO}\ [\mathrm{S4}] = \mathrm{NDO} \quad (4)$$

These values were used to quantify the change in exploratory behaviour elicited by the spatial rearrangement.

All sessions were video-recorded using a ceiling-mounted camera, and behavioural tracking was performed offline with EthoVision XT v.17.0 (Noldus).

3.13.3 Accelerated Rotarod Test

Motor coordination and motor learning were assessed using the accelerated rotarod test. The experimental procedure, performed over three consecutive days, consisted of two days of training followed by one test session on the third day (protocol adapted from[152]. The test was conducted using a computerized four-lane rotarod apparatus (Panlab, Harvard Apparatus), featuring a rotating cylinder (3 cm diameter) with independently controlled lanes, such that up to four mice could be tested simultaneously.

On the first day, mice underwent an acclimation phase consisting of a single 30-s trial on the rod rotating at a constant speed of 4 rpm. Subsequently, in each session, the rod acceleration was programmed to increase linearly from 4 to 40 rpm over a 300-s period. Each session included four trials per mouse, separated by 5-min inter-trial intervals. The following behavioural parameters were measured for each trial: latency to fall (time in seconds spent on the rod) and the best performance across sessions, defined as the longest latency to fall on the final test day.

3.14 Power analysis, Sample size, randomization, blinding

The sample number per group and experiment was determined by power analysis (G*Power software, 3.1.9.7v) using a power of 0.8 and errors of 0.05; standard deviations of all groups were obtained from previous publications with similar experiments.

Randomization was done with a random-number table to decide how mice from the same litter would be randomly assigned to the different groups.

Researchers were blinded to the animal group; un-blinding occurred after analysis.

The experimental units for each experiment are described in detail in Figure legends.

3.15 Statistical analysis

Analyses were performed using Prism8.01 (GraphPad). Data were checked for normality using the Shapiro-Wilk and D'Agostino-Pearson tests. Data from two groups (i.e. Sham/Casp3, Saline/6OHDA, WT/Tg2576, Tg Sham/Tg Casp3) were analysed with Two-tailed parametric (unpaired *t*-test or Welch's *t*-test) or non-parametric Mann-Whitney tests according to normality. Sholl analysis data, PPR, I/O curves, mean exploration time during the training and test phases of the NOR test, mean exploration time during the familiarization and test phases of the SOR test, and mean latency to fall across sessions in the rotarod test were analysed by Two-way Repeated-

Measures (RM) ANOVA, using distance from soma, interval, stimulus intensity, object category (left *vs* right and novel *vs* familiar), test sessions (S1-4), object category (DO *vs* NDO), and number of sessions (S1-12) as repeated values, respectively. Post-hoc tests were performed using Sidak's or Tukey's multiple comparison tests.

Data from three or four groups were analysed by One-Way ANOVA followed by Tukey's multiple comparison test, or with Kruskal-Wallis followed by Dunn's multiple comparison test.

For the differential expression analysis of transcriptomics expression, statistical significance was determined using the Wald test [153]. Cut offs ($p < 0.050$) were used for p values and for p values adjusted with the false discovery rate (FDR) methods of Benjamini-Hochberg and Benjamini-Yekutieli (FDR B&H and FDR B&Y, respectively).

See Figure legends for more details. $p \leq 0.05$ indicates statistical significance. In box-and-whisker plots, the central line denotes the median, edges are upper and lower quartiles, whiskers show minimum and maximum values and points are individual experiments. In the violin plots used for spine density, the width of the plot at any given point corresponds to the frequency of data points at that value. The volcano plot for the transcriptomic analysis shows scattered individual data points. All other data are presented as mean ± s.e.m.

4. Results

4.1 Lesion of midbrain DA and 5-HT nuclei induces hippocampal NLRP3-mediated microglia response in C57BL/6N mice

To evaluate the involvement of DA and 5-HT in hippocampal function, we induced a midbrain lesion in the C57BL/6N mouse strain. Specifically, we targeted the dopaminergic VTA and the medial portion of the SNpc, as well as the serotonergic IPN, regions known to provide monoaminergic inputs to the hippocampus[33,49,50,154]. To simultaneously target these nuclei with a single tool, we took advantage of the ectopic expression of the TH promoter. Although the TH protein is selectively expressed in dopaminergic neurons of the VTA and SNpc, the TH promoter is also ectopically expressed in the IPN[35,155,156]. Therefore, we used a combined viral strategy to unilaterally co-infuse into the midbrain (i) an AAV expressing an improved Cre-recombinase under the TH promoter (AAV1-THp-iCre), together with (ii) an AAV containing the Cre-recombinase-inducible floxed Caspase-3 (AAV5-flex-taCasp3-TEVp) gene, to overexpress Casp3, an executioner caspase in apoptosis[148], following TH promoter-driven recombination [35,157]; thereafter, Casp3 mice; **Figure 5A,B**). Control mice received only the AAV1-THp-iCre virus (hereafter, Sham mice).

In Casp3 and Sham mice, we next examined the midbrain rostro-caudally to confirm the lesion in the VTA, SNpc and IPN (**Figure 5C**). The stereological counting of TH^+ neurons in the ipsilateral VTA and SNpc revealed a significant reduction in Casp3 compared to Sham mice one month post-lesion (**Figure 5D**). Consistent with the ectopic activity of the TH promoter in the IPN, $5\text{-}HT^+$ neurons were also significantly reduced in Casp3 mice (**Figure 5E**). Since the midbrain receives TH^+ fibres from the LC, we also investigated whether the viral infusion could lead to the retrograde loss of TH^+ LC neurons (**Figure 5F**). Yet, no changes were observed in the number of LC TH^+ neurons in Casp3 mice (**Figure 5G**).

To confirm the reduction of midbrain monoaminergic inputs to the hippocampus in Casp3 mice, we analysed the dopaminergic and serotonergic innervations in the dorsal hippocampus one month post-surgery (**Figure 5H**). Hippocampal TH+ fibre density was significantly reduced in Casp3 mice (**Figure 5I**). This was not due to damage to the TH^+ innervation from the LC, as the density of NET-positive fibres remained unchanged (**Figure 5J**). Consistent with the significant loss of IPN 5-HT^+ neurons, Casp3 mice also exhibited reduced hippocampal serotonergic fibre density, labelled for the 5-HT transporter (SERT; **Figure 5K**). Of note, the stereological cell counting of 5-HT^+ neurons in both the dorsal and medial Raphe showed no changes in Casp3 mice (**Figure 5L**,**M**), confirming that the reduction of hippocampal $SERT^+$ fibres is solely due to the IPN lesion. In line with the loss of dopaminergic and serotonergic innervation in the hippocampus, HPLC analysis of total hippocampal tissue confirmed decreased levels of both DA and 5-HT and their relative metabolites (DOPAC, HVA and 5-HIAA) in Casp3 mice (**Figure 5N,O**). No changes in NE and MOPEG levels were observed (**Figure 5P**). Thus, the midbrain lesion in Casp3 mice results in the combined depletion of both DA and 5-HT in the hippocampus.

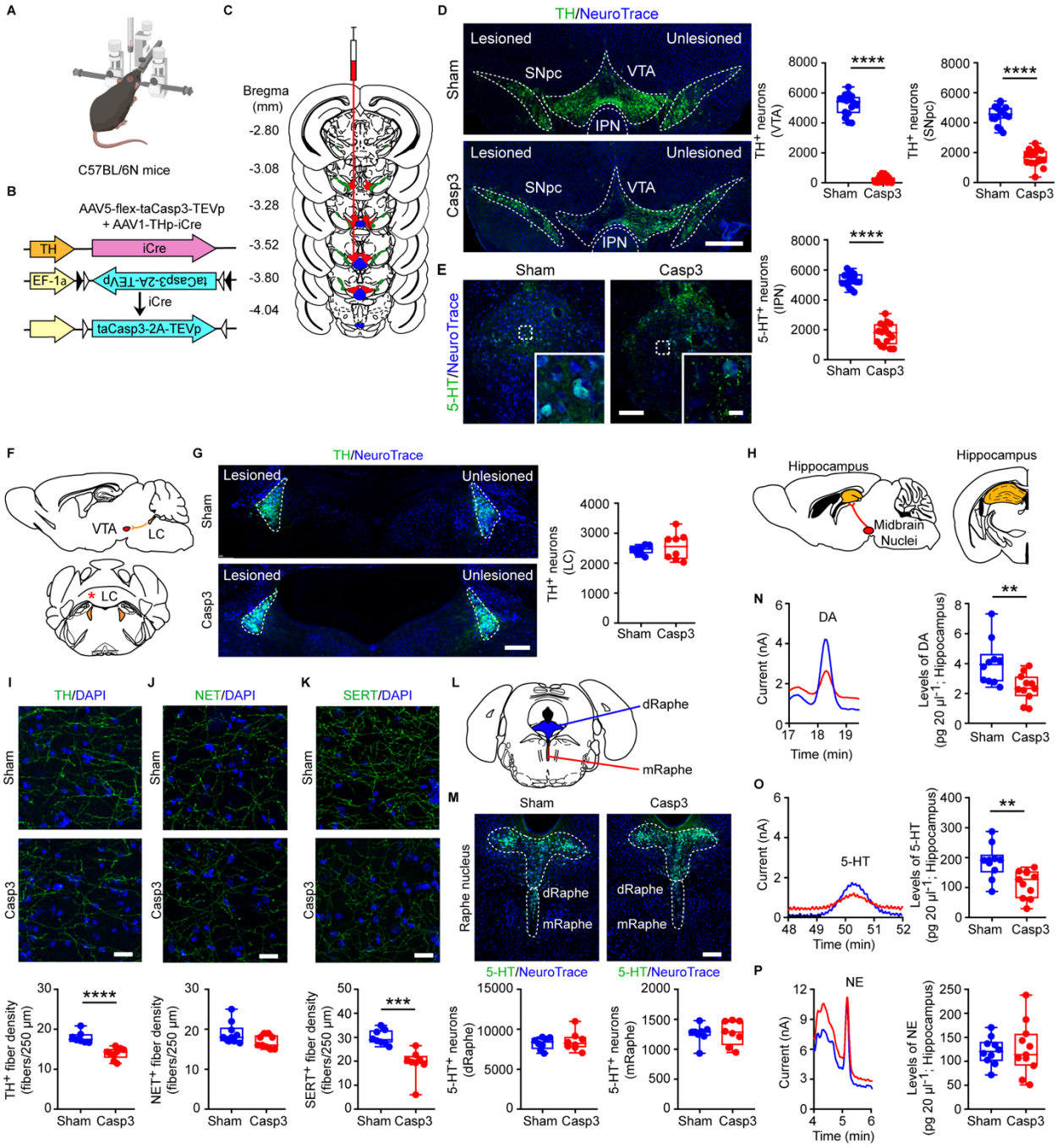

Figure 5: Validation of midbrain lesion in Casp3 mice. A-B) C57BL/6N mice were unilaterally infused in the midbrain with a dual-AAV approach. The double-floxed AAV5-flex-taCasp3-TEVp, driven by the EF-1α promoter, comprises the inverted taCasp3-TEVp. Expression of iCre-recombinase under the TH promoter (AAV1-THp-iCre) determines recombination resulting in the active orientation of taCasp3-TEVp. **C)** Rostro-caudal extent of regions for cell counts. The evaluated midbrain nuclei are VTA (red), SNpc (green), IPN (blue). **D)** Immunofluorescence of TH^+ neurons, counterstained with NeuroTrace, in Sham and Casp3 mice (scale: 500 µm) and stereological TH^+ cell count in the ipsilateral VTA (n = 16 mice / group. Mann-Whitney test: ****$p < 0.0001$) and SNpc (n = 16 mice / group. Unpaired *t*-test: ****$p < 0.0001$). **E)** Images of IPN stained with 5-HT and NeuroTrace (scale: 100 µm; inset, 10 µm), and stereological 5-HT^+ cell count (n = 16 mice / group. Unpaired *t*-test: ****$p < 0.0001$). **F)** Scheme of LC-VTA connectivity (sagittal section) and LC (coronal section). The * indicates the analysed hemisphere. **G)** Confocal images of LC TH^+ neurons (counterstained with NeuroTrace, scale: 200 µm) and plot of TH^+ cell counts (n = 8 mice / group). **H)** Scheme of VTA-hippocampus connectivity (sagittal section) and of hippocampus (coronal section). **I-K)** Confocal

images and plots showing **I)** TH^+ (Sham: n = 7, Casp3: n = 9 mice. Unpaired *t*-test: ****p < 0.0001), **J)** NET^+ (Sham: n = 10; Casp3: n = 9 mice) and **K)** $SERT^+$ (n = 8 mice / group. Unpaired *t*-test: ***p = 0.0003) hippocampal fibre density (expressed as fibres per 250 µm; scale: 20 µm). Nuclei are counterstained with DAPI. **L)** Schematic representation of dorsal (dRaphe; blue) and medial raphe (mRaphe; red; coronal section). **M)** Confocal images of dRaphe and mRaphe stained with 5-HT in Sham and Casp3 mice (counterstained with NeuroTrace; scale: 200 µm) and plots showing 5-HT^+ neuron counts (n = 8 mice / group). **N-P)** Representative chromatogram segments and plots of monoamine hippocampal levels (Sham: n = 10, Casp3: n = 11 mice; *DA*: Unpaired *t*-test: **p = 0.007; *5-HT*: Unpaired *t*-test: **p = 0.004). Figure from[136]

Consistent with the known role of DA and 5-HT in modulating hippocampal-dependent memory[134,158,159], Casp3 mice exhibited significant impairments in object recognition and spatial memory, as assessed by the NOR and SOR tests, respectively (**Figure 6A-C**). Casp3 mice also displayed anxiety-like behaviour − evidenced by reduced time spent in the centre and increased time in the periphery of the open field arena − as well as hyperlocomotion, reflected by a greater total distance travelled (**Figure 6D-E**). Notably, Casp3 mice showed no motor coordination deficits, in the accelerated rotarod test compared to Sham mice (**Figure 6F**).

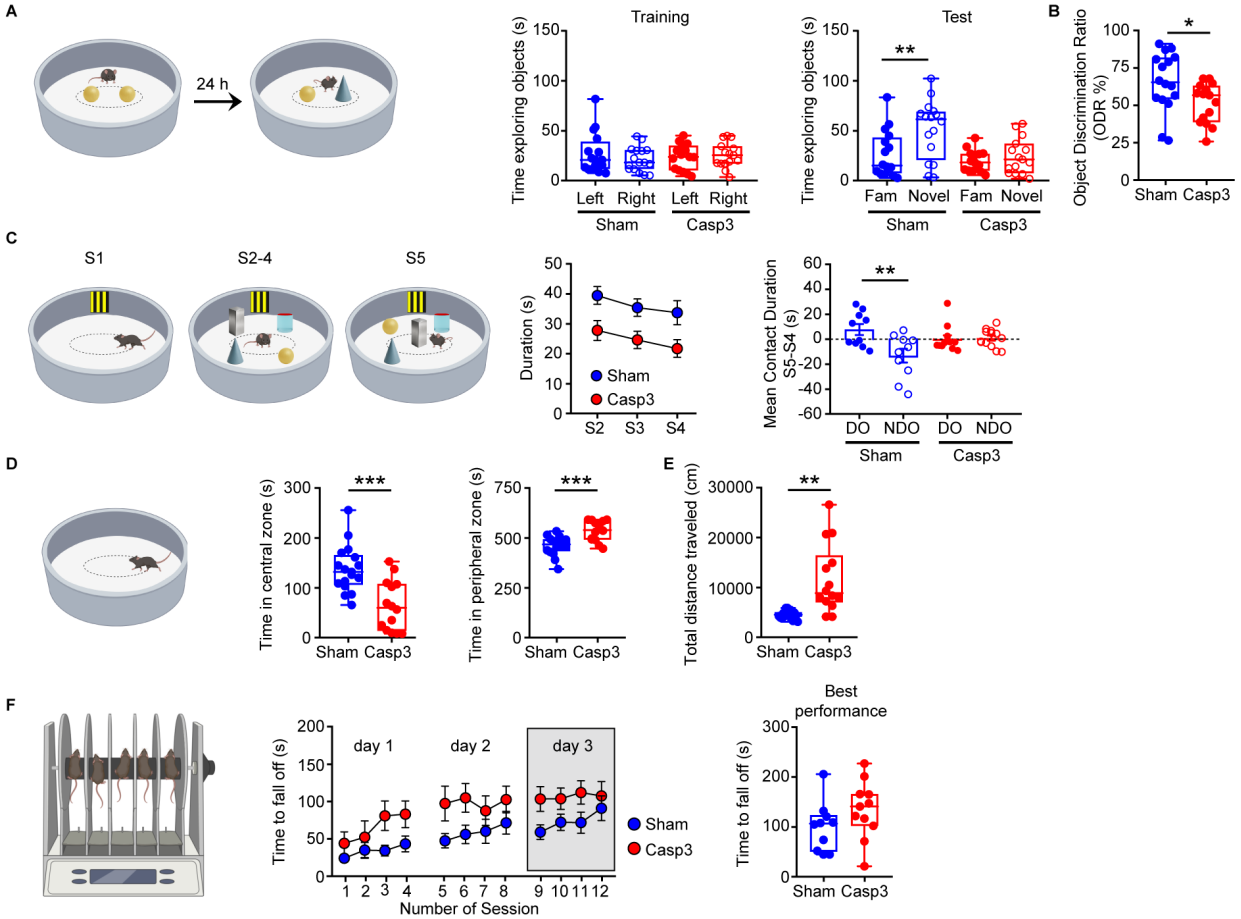

Figure 6: Behavioural evaluation in Sham and Casp3 mice. A) The plots show the exploration time spent by Sham and Casp3 mice with the novel and/or familiar object during the NOR training (left) and test session 24 h after training (right; Sham: n = 16; Casp3: n = 15 mice. Two-way RM-ANOVA: Training: interaction $F_{1,58} = 1.064$, $p = 0.3065$; object category $F_{1,58} = 0.2731$, $p = 0.6032$; lesion $F_{1,58} = 0.01358$, $p = 0.9076$; Test: interaction $F_{1,58} = 3.331$, $p = 0.0732$; object category $F_{1,58} = 7.526$, $p = 0.0081$; lesion $F_{1,58} = 9.465$, $p = 0.0032$; Sham Familiar Object vs Sham Novel Object: **p = 0.0092, with Tukey's multiple comparisons test), and (**B**) the Object Discrimination Ratio (Unpaired t-test: *p = 0.0272). **C**) The plots show (left) the mean duration of exploration (± s.e.m) across all objects during sessions 2, 3, and 4 (Sham: n = 10; Casp3: n = 11 mice. Two-way RM-ANOVA: interaction $F_{2,57} = 0.0181$, $p = 0.982$; sessions $F_{2,57} = 1.710$, $p = 0.1899$; lesion $F_{1,57} = 19.34$, $p < 0.0001$) and (right) the mean time (± s.e.m) spent exploring Displaced (DO) or Non-Displaced Objects (NDO) during S5 minus the time spent exploring the same object category during the final familiarization session (S4), in Sham and Casp3 mice (Two-way RM-ANOVA: interaction $F_{1,38} = 7.242$, $p = 0.0105$; object category $F_{1,38} = 6.904$, $p = 0.0123$; lesion $F_{1,38} = 0.6922$, $p = 0.4106$; Sham DO vs Sham NDO: **p = 0.0039, with Tukey's multiple comparisons test). **D**) The plots show the time spent in the central (left) and peripheral (right) zones of the open field arena (Sham: n = 17; Casp3: n = 14 mice. Time in Centre: Unpaired t-test: ***p = 0.0002; Time in Periphery: Unpaired t-test: ***p = 0.0002), and (**E**) the locomotor activity in the whole arena of Sham and Casp3 mice during the open field test (Total distance travelled: Welch's t-test: **p = 0.0020). **F**) The plots show the motor coordination (left) in Sham and Casp3 mice during the rotarod test, assessed as mean latency to fall (± s.e.m) over 4 sessions/day across 3 consecutive days (Sham: n = 10; Casp3: n = 11 mice. Two-way RM-ANOVA: interaction $F_{11,2092} = 0.9112$, $p = 0.5304$; sessions $F_{11,209} = 9.573$, $p < 0.0001$; lesion $F_{1,19} = 3.314$, $p = 0.0845$), and their best performance (right) on the final test day (Day 3; Unpaired t-test: $p = 0.1562$). Figure from[136]

To investigate whether the midbrain lesion could induce the insurgence of inflammatory events in the hippocampus, we examined morphological and functional changes in microglia and astrocytes, one month post-lesion (**Figure 7A**). Stereological cell counting in the dorsal hippocampus revealed an increase in the number of $Iba1^+$ microglia in Casp3 mice (**Figure 7B**).

In contrast, the number of $GFAP^+$ astrocytes remained unchanged following lesion (**Figure 7C**).

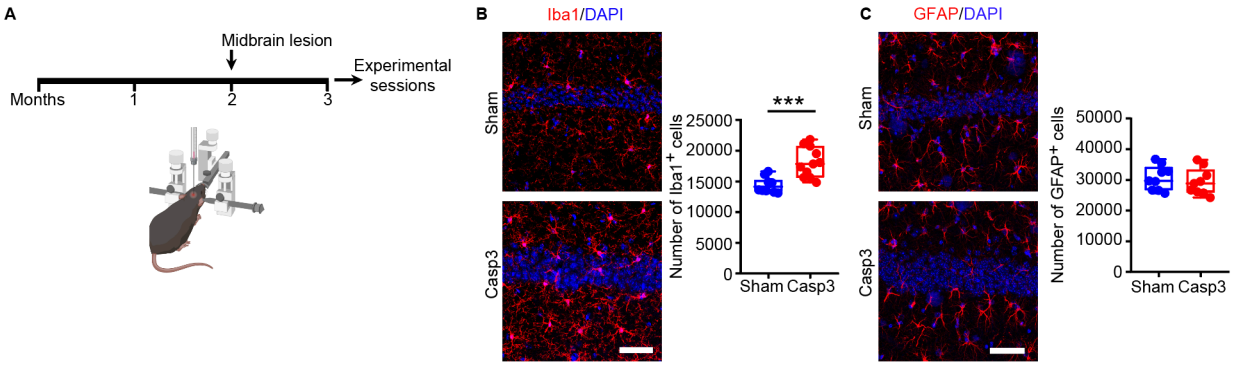

Figure 7: Midbrain lesion induces NLRP3-dependent microglia response in the hippocampus of Casp3 mice. A) Experimental workflow: mice were examined 1 month after lesion. **B)** Images and plot showing hippocampal $Iba1^+$ cell count in Sham and Casp3 mice (Sham: n = 10; Casp3: n = 11 mice; Unpaired *t*-test: ***p = 0.0003). Nuclei are counterstained with DAPI (scale: 50 µm). **C)** Representative confocal images and plot showing stereological cell count of $GFAP^+$ cells in the hippocampus of Sham and Casp3 mice (n = 9 mice / group). Nuclei are counterstained with DAPI (scale: 50 µm). Figure adapted from[136]

To further characterise phenotypic changes in microglia, we analysed their morphology using Sholl analysis. We observed a greater complexity of microglia processes in Casp3 mice, including increased number of intersections, nodes and endings, as well as increased processes length (**Figure 8A**). Microglia soma perimeter and area were comparable between groups (**Figure 8A**). Functional marker analysis revealed higher CD68 immunoreactivity in the cell body of $Iba1^+$ cells from Casp3 mice (**Figure 8B**), overall suggesting altered microglia.

One of the key contributors in the development of neuroinflammation is the NLRP3 inflammasome, which drives the secretion of pro-inflammatory cytokines such as IL-1β and IL-18[110,160]. Therefore, we examined the number of $Iba1^+$ cells expressing NLRP3 ($NLRP3^+/Iba1^+$) and the levels of NLRP3 and IL-1β. Cell counting revealed a significant increase in the percentage of $NLRP3^+/Iba1^+$ cells in Casp3 compared to Sham mice (**Figure 8C,** *left*). Moreover, we found increased NLRP3 immunoreactivity (**Figure 8C,** *right*), associated with higher IL-1β levels (**Figure 8E**), indicating a pro-inflammatory profile.

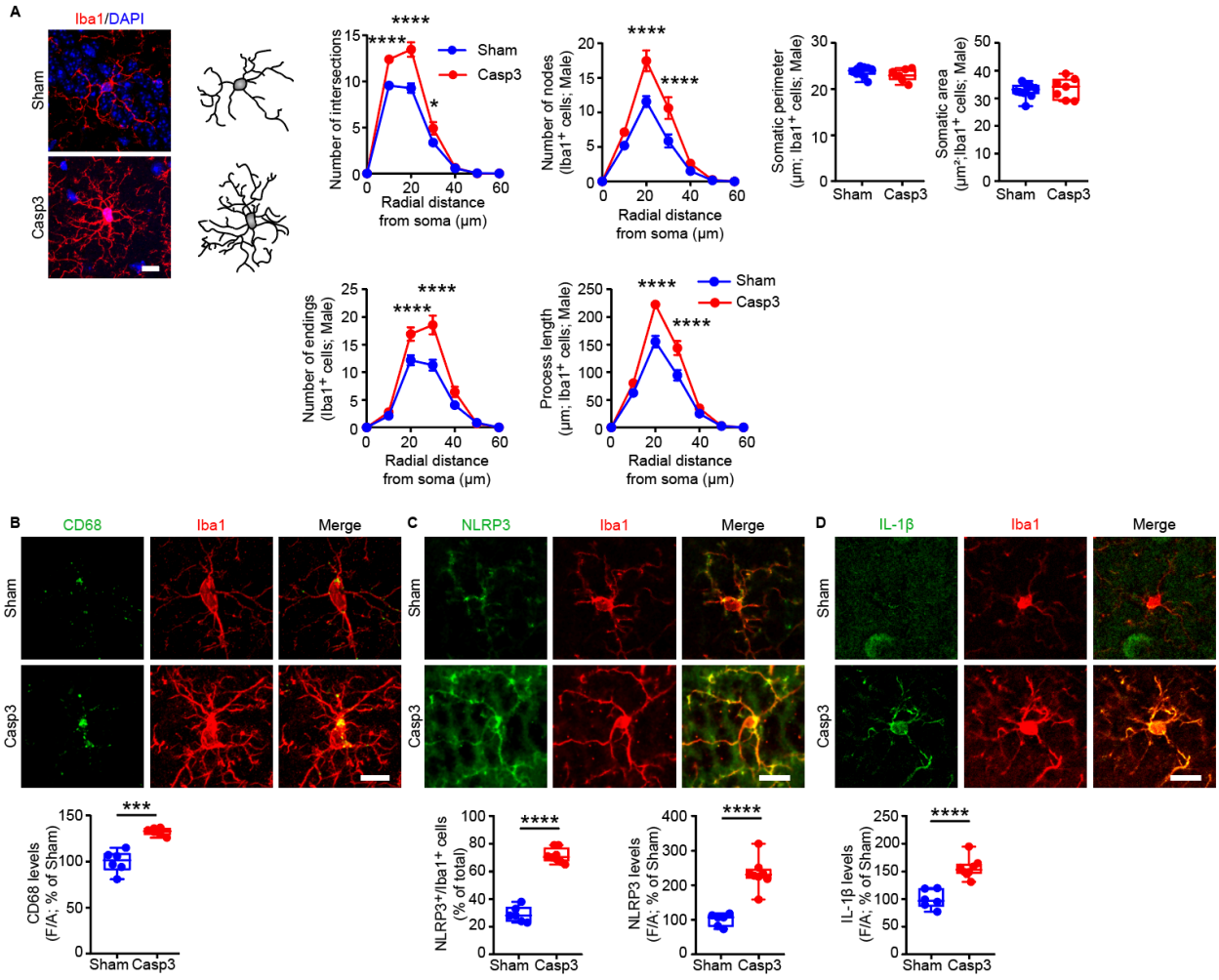

Figure 8: Midbrain lesion induces NLRP3-dependent microglia response in the hippocampus of Casp3 mice. **A)** Representative images and 3D-reconstruction of microglia (scale: 10 µm) in Sham and Casp3 mice. The graph shows microglia Sholl analysis, depicting number of intersections at different distances from soma (Sham: n = 10; Casp3: n = 7 mice; Two-way RM-ANOVA: *Intersections*: interaction $F_{6,90} = 15.58$, $p < 0.0001$; distance $F_{6,90} = 579.6$, $p < 0.0001$; lesion $F_{1,15} = 16.68$, $p = 0.001$; Sham *vs* Casp3: ****$p < 0.0001$ at 10-20 µm; *$p = 0.017$ at 30 µm, analysed with Sidak's multiple comparisons test); *Nodes*: interaction $F_{6,90} = 9.348$, $p < 0.0001$; distance $F_{6,90} = 192.4$, $p < 0.0001$; lesion $F_{1,15} = 11.57$, $p = 0.004$; ****$p < 0.0001$ at 20-30 µm; *Endings*: interaction $F_{6,90} = 12.39$, $p < 0$ .0001; distance $F_{6,90} = 261.4$, $p < 0.0001$; lesion $F_{1,15} = 10.65$, $p = 0.005$; ****$p < 0.0001$ at 20-30 µm; *Length*: interaction $F_{6,90} = 14.29$, $p < 0.0001$; distance $F_{6,90} = 416.9$, $p < 0.0001$; lesion $F_{1,15} = 14.62$, $p = 0.002$; ****$p < 0.0001$ at 20-30 µm; all with Sidak's multiple comparisons test), and the somatic perimeter and area of $Iba1^+$ cells in the hippocampus of Sham and Casp3 mice (Sham: n = 10; Casp3: n = 7 mice). **B)** Representative images and plot showing CD68 immunostaining intensity in microglia (scale: 10 µm; n = 6 mice / group; Welch's *t*-test: ***$p = 0.0007$). **C)** Confocal images of NLRP3 and Iba1 immunostaining (scale: 15 µm). The plots show: % of $NLRP3^+/Iba1^+$ cells (Sham: n = 6; Casp3: n = 8 mice. Unpaired *t*-test: ****$p < 0.0001$) and NLRP3 levels (Unpaired *t*-test: ****$p < 0.0001$). **D)** Confocal images and plot of hippocampal IL-1β levels (scale: 15 µm) in microglia (Sham: n = 6; Casp3: n = 8 mice; Unpaired *t*-test: ****$p <$ 0.0001). Figure adapted from[136]

To assess the transcriptional signatures associated with microglia reactivity, we also performed mRNA sequencing on FACS-sorted hippocampal microglia from Sham and Casp3-lesioned

$CX_3CR\text{-}1^{GFP}$ mice at one month post-lesion (**Figure 9A-D**). Among the 19,117 genes detected, six differentially expressed genes (DEGs) reached significance after FDR correction (FDR < 0.05), and 381 met a nominal threshold (p < 0,05), as illustrated in the volcano plot (**Figure 9E**).

We next examined the full set of DEGs using ToppGene functional annotation to identify perturbed biological processes. The top enriched Gene Ontology (GO) terms within the "Biological Process" category are shown in **Figure 9F**. Consistent with a shift toward a reactive phenotype, Casp3 microglia exhibited significant enrichment for terms related to microglial cell activation (GO:0001774), chemotaxis (GO:0006935), and neuroinflammatory response (GO:0150076). Additional enriched processes included apoptotic regulation (GO:0042981) and translational machinery dynamics such as cytoplasmic translation (GO:0002181), synaptic translation (GO:0140241) and ribosome assembly (GO:0042255).

Collectively, these results demonstrate that the combined depletion of both midbrain DA and 5-HT in Casp3 mice triggers hippocampal neuroinflammation *via* microglia activation and NLRP3 pathway induction.

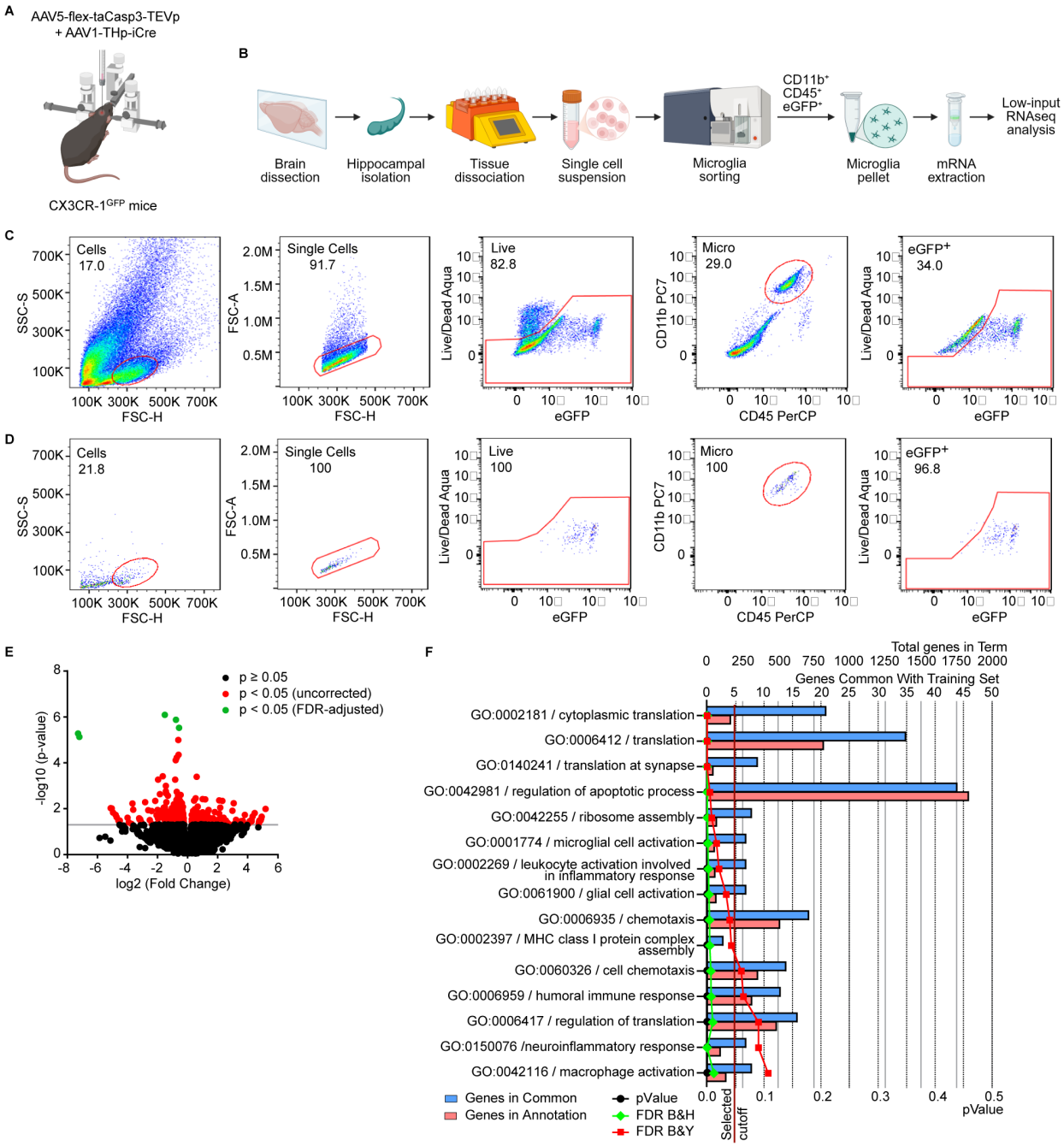

Figure 9: Additional analysis of RNA sequencing in hippocampal microglia from Sham and Casp3 CX$_3$CR-1^{GFP} mice. A) CX$_3$CR-1^{GFP} mice expressing the GFP protein in microglia were unilaterally infused in the midbrain with the AAV5-flex-taCasp3-TEVp + AAV1-THp-iCre mix and analysed 1-month post-lesion. **B)** Scheme of the experimental procedure used for the isolation of hippocampal microglia using the CD11b$^+$-CD45$^+$-eGFP$^+$ gating strategy. **C-D)** Flow-cytometry gating strategy for microglia isolation (**C**) and purity check (**D**). From left to right: the gating on the general cell population was based on size (FSC-H) and granularity (SSC-S); FSC-A *vs* FSC-H "Single Cells" Isolating single cells by removing doublets or clumps; eGFP *vs* live dead Aqua: "Live" Identifying live cells using a viability dye (live dead Aqua); CD45 *vs* CD11b "Micro" Identifying microglia or myeloid cells (CD11b^{high}, CD45^{mid}); eGFP *vs* live dead Aqua: "eGFP$^+$" Identifying cells expressing microglia eGFP$^+$. **E**) Volcano plots illustrating the magnitude (as log$_2$ fold change) and statistical significance (as -log$_{10}$ p-values) of changes in the expression of individual genes in hippocampal microglia of lesioned relative to Sham mice. **F**) Functional enrichment analysis of DEGs ($p < 0.05$) identified in hippocampal microglia gene expression profile of Casp3 compared to Sham

$CX_3CR\text{-}1^{GFP}$ mice. The chart displays the most significant functional enrichment terms for the gene ontology (GO) biological process. The analysis was performed with the ToppGene suite. Figure adapted from[136]

Given the well-established role of monoamines in modulating hippocampal function, we next asked whether this neuroinflammatory environment compromises neuronal dendritic structure. Morphological analysis of biocytin-filled CA1 pyramidal neurons revealed a significant reduction in distal apical spine density in Casp3 mice relative to Sham controls (**Figure 10A**). To determine whether this structural alteration translated into a functional deficit, we assessed Long-Term Potentiation (LTP) at CA3–CA1 synapses. LTP appeared unaltered in Casp3 slices (**Figure 10B**), suggesting that elevated IL-1β levels might mask a synaptic deficit, an interpretation consistent with prior reports indicating that IL-1β can enhance LTP[161]. Indeed, pre-incubation with the IL-1β receptor antagonist (IL-1β-Ra) unmasked a clear LTP impairment in Casp3 mice (**Figure 10B**), despite unchanged glutamate release probability (PPR) and Input/Output (I/O) curves (**Figure 10C**).

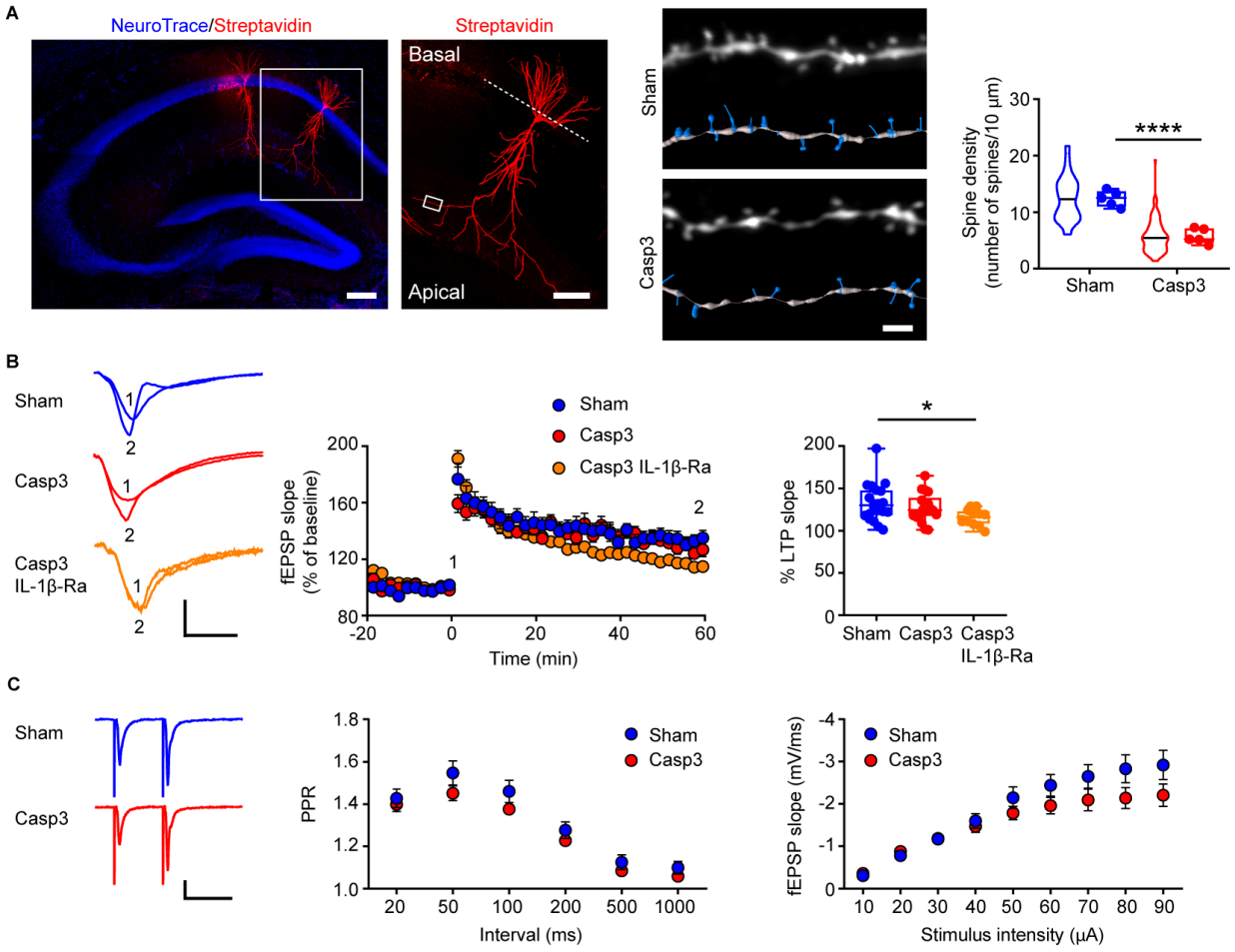

Figure 10: Analysis of synaptic plasticity in Sham and Casp3 mice. A) *Right*, confocal images of biocytin-filled CA1 pyramidal neurons (scale: *left* 250 µm; *right* 100 µm). *Left*, representative images and 3D reconstruction of apical dendritic fragments in the CA1 of Sham and Casp3 mice (scale: *left* 2 µm). Violin plots represent quantification per dendrite and dots represent average data per animal (at least 18 dendritic fragments from 4 cells / 5 mice were used per group; Unpaired *t*-test: ****p < 0.0001). **B)** Representative traces showing *f*EPSPs at half maximal stimulation during baseline and 1 h after the conditioning train (scale: 5 ms; 1 mV) and time-course (mean ± s.e.m.) of normalized, average *f*EPSP slope from Sham, Casp3 and Casp3 slices treated with IL-1β-Ra. The plot shows pooled data for *f*EPSP normalized slope (Sham: n = 20 slices / 10 mice; Casp3: n = 18 slices / 9 mice; Casp3 IL-1β-Ra: n = 12 slices / 5 mice. Kruskal-Wallis: p = 0.038; Sham *vs* Casp3 IL-1β-Ra: *p = 0.023, with Dunn's multiple comparisons test). **C)** Representative *f*EPSP traces of paired responses to half maximal stimulation of Shaffer collateral fibres from Sham and Casp3 slices at 50 ms interval (scale: 50 ms; 1 mV). The plots show (*left*) the PPR at different stimulus intervals (Sham: n = 19 slices / 6 mice; Casp3: n = 17 slices / 5 mice. Two-way RM-ANOVA interaction $F_{5,170} = 0.7433$, p = 0.592; interval $F_{2648,90} = 128.7$, p < 0.0001; lesion $F_{1,34} = 1.636$, p = 0.210) and (*right*) the I/O curves at different stimulation intensities (Sham: n = 21 slices / 12 mice; Casp3: n = 18 slices / 8 mice. Two-way RM-ANOVA interaction $F_{8,296} = 3.575$, p = 0.0006; interval $F_{1430,53} = 86.65$, p < 0.0001; lesion $F_{1,37} = 1.529$, p = 0.224). Figure adapted from[136]

To prove that the hippocampal microglia response requires the loss of both DA and 5-HT, we examined the hippocampus of mice infused in the midbrain with the catecholaminergic neurotoxin 6OHDA that induces selective loss of VTA and SNpc dopaminergic neurons but does not affect IPN 5-HT$^+$ neurons (**Figure 11A-C**). Analysis of microglia in the hippocampus of 6OHDA mice

showed no differences in cell number and morphology compared to saline-injected mice (**Figure 11D-G**). In line with these results, no changes were detected in the levels of CD68, NLRP3 or IL-1β in Iba1^{+} cells of 6OHDA mice (**Figure 11H-J**).

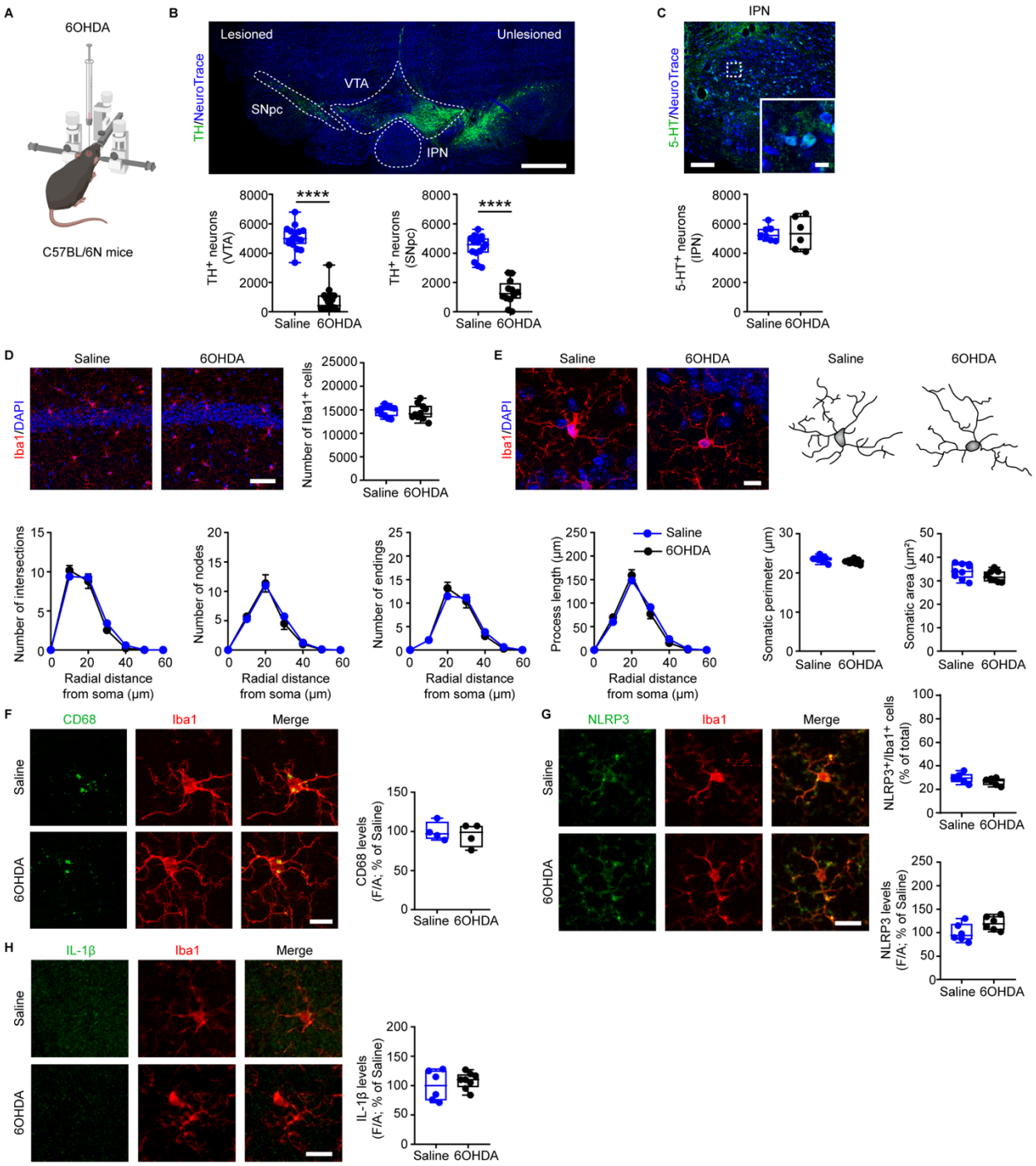

Figure 11: Validation of dopaminergic lesion and evaluation of hippocampal neuroinflammation in 6OHDA mice. A) Unilateral infusion of 6OHDA or saline into the left midbrain under stereotactic control in C57BL/6N mice. **B)** Representative immunofluorescence of TH^+ neurons, counterstained with NeuroTrace, in the midbrain of 6OHDA mice (scale: 500 µm) and stereological cell count of TH^+ neurons in the ipsilateral VTA (*left*; Saline: n = 16; 6OHDA: n = 17 mice. Mann-Whitney test: ****$p < 0.0001$) and SNpc (*right*; Saline: n = 15; 6OHDA: n = 12 mice. Unpaired *t*-test: ****$p < 0.0001$). **C)** Representative confocal images of IPN stained with 5-HT and NeuroTrace in 6OHDA mice (scale: 100 µm; inset, 10 µm), and stereological cell count of $5\text{-}HT^+$ neurons in 6OHDA mice (Saline: n = 7; 6OHDA: n = 6 mice). **D)** Confocal images and plot showing cell count of $Iba1^+$ cells in Saline and 6OHDA hippocampi (n = 10 mice / group). Nuclei are counterstained with DAPI (scale: 50 µm). **E)** Representative confocal images and 3D-reconstruction of microglia (Iba1; scale: 10 µm). The graphs show Sholl analysis of microglia cells, depicting number of intersections, nodes, endings and length at different radial distances from soma (Saline: n = 9; 6OHDA: n = 8 mice; Two-way RM-ANOVA: *Intersections*: interaction $F_{6,90} = 1.461$, $p = 0.201$; distance $F_{6,90} = 422.1$, $p < 0.0001$; lesion $F_{1,15} = 0.223$, $p = 0.644$; *Nodes*: interaction $F_{6,90} = 0.738$, $p = 0.621$; distance $F_{6,90} = 181.9$, $p < 0.0001$; lesion $F_{1,15} = 0.041$, $p = 0.843$; *Endings*: interaction $F_{6,90} = 1.651$, $p = 0.142$; distance $F_{6,90} = 260.5$, $p < 0.0001$; lesion $F_{1,15} = 0.002$, $p = 0.964$; *Length*: interaction $F_{6,90} = 2.522$, $p = 0.027$; distance $F_{6,90} = 412.6$, $p < 0.0001$; lesion $F_{1,15} = 0.008$, $p = 0.930$) and somatic area and perimeter. **F)** Confocal images of CD68 and Iba1 (scale: 10 µm). The plot shows CD68 immunostaining intensity in microglia cell body (n = 4 mice / group). **G)** Confocal images of NLRP3 and Iba1 (scale: 15 µm). The plots show: (*top*) the % of $NLRP3^+/Iba1^+$ cells and (*bottom*) NLRP3 levels (n = 6 mice / group). **H)** Confocal images of IL-1β and Iba1 (scale: 15 µm) and plot of hippocampal IL-1β levels (Saline: n = 6; 6OHDA: n = 8 mice). Figure from[136]

Similarly, to assess whether the selective loss of the serotonergic component alone is sufficient to elicit hippocampal neuroinflammation, a separate cohort of mice received targeted IPN injections ($Casp3^{IPN}$ mice) of the AAV1-THp-iCre + AAV5-flex-taCasp3-TEVp mix, selectively lesioning $5\text{-}HT^+$ neurons while sparing midbrain dopaminergic neurons (**Figure 12A-C**). Compared with Sham-injected controls ($Sham^{IPN}$), $Casp3^{IPN}$ mice showed a selective reduction of hippocampal $SERT^+$ fibres and preserved TH^+ innervation (**Figure 12D-E**). Notably, serotonergic denervation alone failed to induce microglia reactivity, as evidenced by unchanged microglia number, morphology (**Figure 12F-I**) and levels of CD68, NLRP3, or IL-1β immunoreactivity in $Iba1^+$ cells (**Figure 12J-L**), arguing against a pro-inflammatory microglia response.

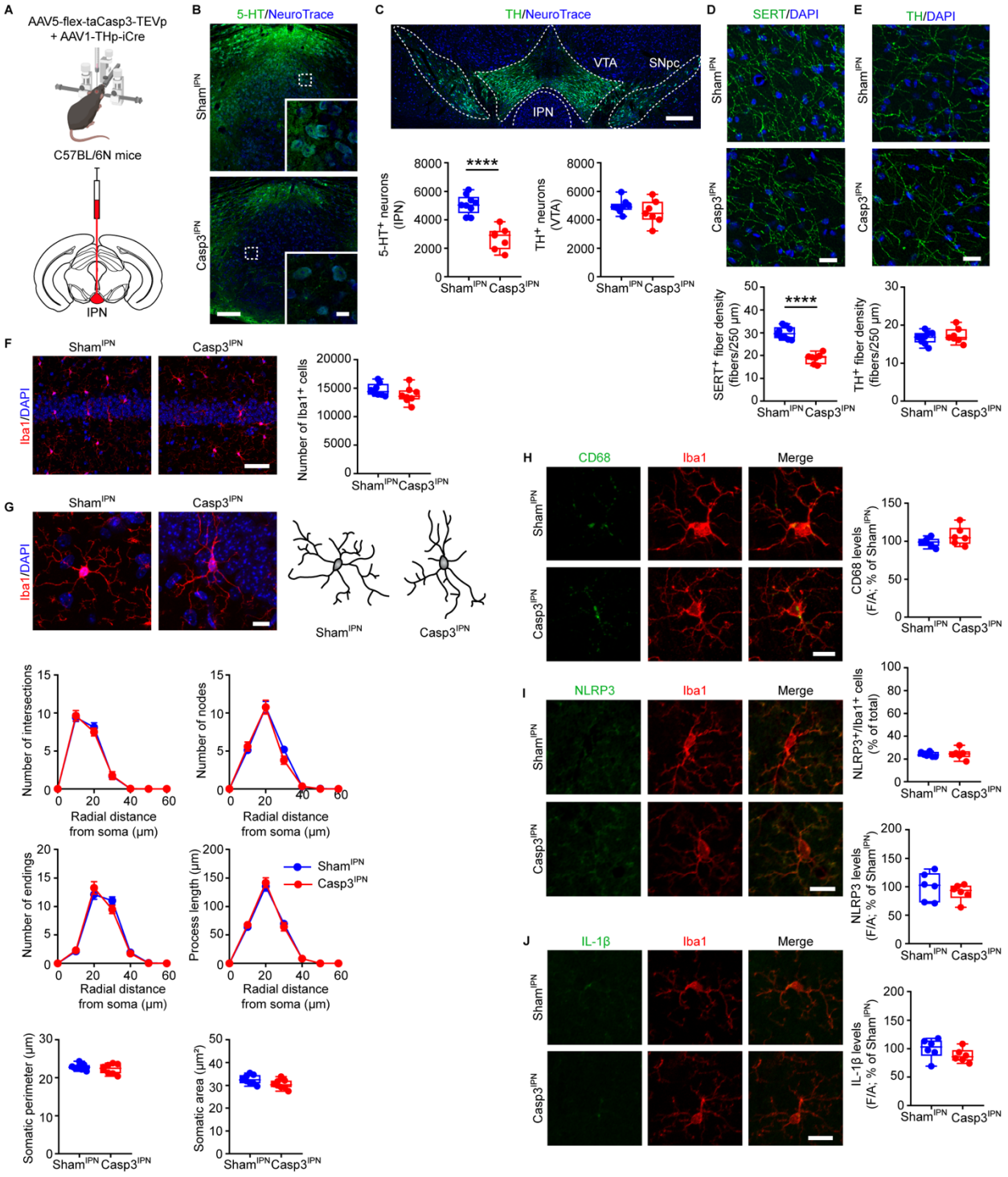

Figure 12: Validation of serotonergic lesion and evaluation of hippocampal neuroinflammation in Casp3^{IPN} mice. A) Unilateral infusion of AAV5-flex-taCasp3-TEVp and AAV1-THp-iCre into the IPN under stereotactic control in C57BL/6N mice. **B)** Representative confocal images of IPN stained with 5-HT and NeuroTrace in Sham^{IPN} and Casp3^{IPN} mice (scale: 100 µm; inset, 10 µm), and stereological cell count of 5-HT^{+} neurons in the total IPN (Sham^{IPN}: n = 9; Casp3^{IPN}: n = 7 mice. Unpaired *t*-test: ****p < 0.0001). **C)** Representative immunofluorescence of TH^{+} neurons, counterstained with NeuroTrace, in the midbrain of Casp3^{IPN} mice (scale: 250 µm) and stereological cell count of TH^{+} neurons in the ipsilateral VTA (Sham^{IPN}: n = 9; Casp3^{IPN}: n = 7 mice). **D-E)** Confocal images and plots showing **D)** SERT^{+} (Sham^{IPN}: n = 9; Casp3^{IPN}: n = 7 mice. Unpaired *t*-test: ****p < 0.0001) and **E)** TH^{+} (Sham^{IPN}:

n = 9; Casp3^{IPN}: n = 7 mice) hippocampal fibre density (expressed as fibres / 250 µm; scale: 20 µm). Nuclei are counterstained with DAPI. **F)** Confocal images and plot showing cell count of Iba1^{+} cells in Sham^{IPN} and Casp3^{IPN} hippocampi (n = 8 mice / group). Nuclei are counterstained with DAPI (scale: 50 µm). **G)** Representative confocal images and 3D-reconstruction of microglia (scale: 10 µm), and graphs showing Sholl analysis of microglia cells, depicting number of intersections, nodes, endings and length at different radial distances from soma (n = 8 mice / group; Two-way RM-ANOVA: *Intersections*: interaction $F_{6,84} = 0.312$, $p = 0.929$; distance $F_{6,90} = 296$, $p < 0.0001$; lesion $F_{1,14} = 0.041$, $p = 0.842$; *Nodes*: interaction $F_{6,84} = 1.1$, $p = 0.369$; distance $F_{6,90} = 216.6$, $p < 0.0001$; lesion $F_{1,14} = 0.041$, $p = 0.842$; *Endings*: interaction $F_{6,84} = 1.390$, $p = 0.228$; distance $F_{6,90} = 249.4$, $p < 0.0001$; lesion $F_{1,14} = 0.035$, $p = 0.853$; *Length*: interaction $F_{6,84} = 0.358$, $p = 0.904$; distance $F_{6,90} = 302.6$, $p < 0.0001$; lesion $F_{1,14} = 0.042$, $p = 0.841$) and somatic area and perimeter. **H)** Confocal images of CD68 and Iba1 (scale: 10 µm). The plot shows CD68 immunostaining intensity in microglia cell body (n = 6 mice / group). **I)** Confocal images of NLRP3 and Iba1 (scale: 15 µm). The plots show: (*top*) the % of NLRP3^{+}/Iba1^{+} cells and (*bottom*) NLRP3 levels (n = 6 mice / group). **J)** Confocal images of IL-1β and Iba1 (scale: 15 µm) and plot of hippocampal IL-1β levels (n = 6 mice / group). Figure from[136]

Collectively, these findings demonstrate that only the combined loss of midbrain DA and 5-HT innervation synergistically drives hippocampal neuroinflammation, dendritic spine loss, and associated deficits in synaptic plasticity − key pathological features contributing to memory impairment in AD.

4.2 Boosting of DA or 5-HT signalling rescues hippocampal NLRP3-mediated neuroinflammation in Casp3 mice

DA and 5-HT receptors are expressed in both microglia and astrocytes. Indeed, both monoamines negatively regulate glial cell reactivity by inhibiting the NLRP3 inflammasome and the subsequent release of pro-inflammatory cytokines[73,74,121,162].

We thus treated Casp3 mice with dopaminergic or serotonergic drugs to attenuate hippocampal inflammation (**Figures 12 and 14**). Sub-chronic administration of the DA precursor L-DOPA (4 days) or the selective D1 receptor agonist A68930 (7 days) (**Figure 13A**) reduced the microglial pro-inflammatory response in Casp3 mice compared to vehicle-treated controls, fully restoring both microglia numbers and morphology to levels comparable to Sham mice (**Figure 13B-C**). Both drugs also reduced the percentage of NLRP3^{+}/Iba1^{+} cells and the levels of NLRP3 and IL-1β compared to vehicle-treated Casp3 mice (**Figure 13D,E**).

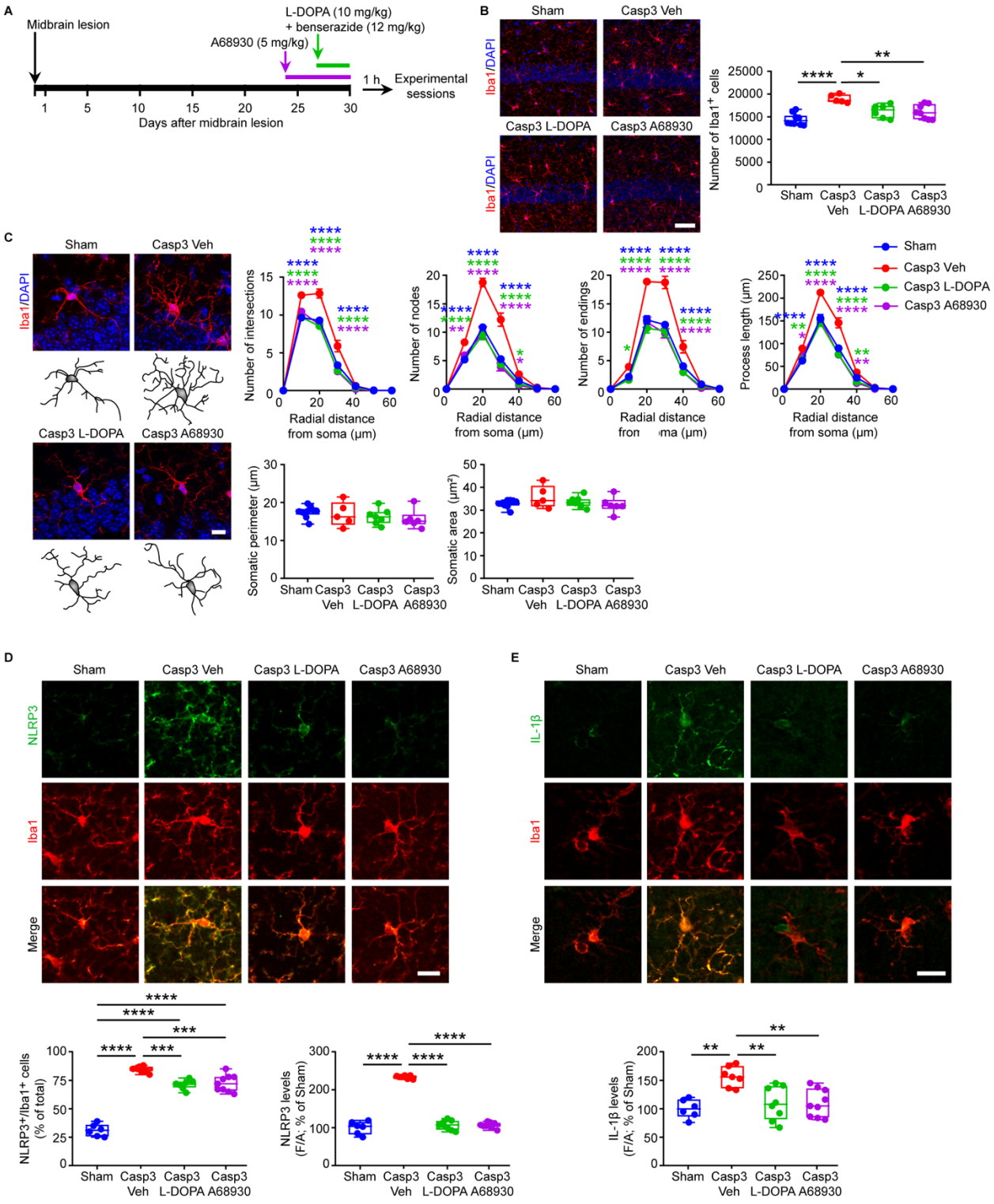

Figure 13: Dopaminergic treatments suppress microglia-mediated neuroinflammation in the Casp3 hippocampus. A) Experimental procedure for the sub-chronic treatments of saline (Veh), L-DOPA (10 mg/kg + benserazide 12 mg/kg; 4 days; i.p) or A68930 (5 mg/kg; 7 days; i.p.) in Casp3 mice. Animals were sacrificed 1h after the last treatment. **B)** Confocal images and plot showing Iba1^{+} numbers in the hippocampus (scale: 50 µm) of Sham mice and of Casp3 mice treated with Veh or L-DOPA or A68930 (Sham: n = 10, Casp3 Veh: n = 5, Casp3 L-DOPA: n = 6, Casp3 A68930: n = 8 mice; One-way ANOVA: $F_{3, 25} = 12.92$; $p < 0.0001$; Sham *vs* Casp Veh: ****$p < 0.0001$; Casp3 Veh *vs* Casp3 L-DOPA: *$p = 0.012$, Casp3 Veh *vs* Casp3 A68930: **$p = 0.004$, with Tukey's multiple

comparisons test). Nuclei are counterstained with DAPI. **C)** Representative confocal images and 3D-reconstruction of microglia in Sham and Casp3 mice treated with Veh, L-DOPA or A68930 (scale: 10 μm) and intersection analysis (Sham: n = 10; Casp3 Veh: n = 5, Casp3 L-DOPA: n = 7, Casp3 A68930: n = 6 mice. Two-way RM-ANOVA: *Intersections*: interaction $F_{18,144} = 11.59$, $p < 0.0001$; distance $F_{6,144} = 1530$, $p < 0.0001$; treatment $F_{3,24} = 20.31$, $p < 0.0001$; Sham *vs* Casp3 Veh (blue): ****$p < 0.0001$ at 10-30 μm; Casp3 Veh *vs* Casp3 L-DOPA (green): ****$p < 0.0001$ at 10-30 μm; Casp3 Veh *vs* Casp3 A68930 (purple): ****$p < 0.0001$ at 10-30 μm, analysed with Tukey's multiple comparisons test). **D)** Confocal images of NLRP3 and Iba1 immunostaining (scale: 15 μm). The plots show: the % of $NLRP3^+/Iba1^+$ cells (Sham: n = 6; Casp3 Veh: n = 7, Casp3 L-DOPA: n = 8, Casp3 A68930: n = 9 mice; One-Way ANOVA: $F_{3,26} = 121.4$; $p < 0.0001$. Sham *vs* Casp3 Veh: ****$p < 0.0001$, Sham *vs* Casp3 L-DOPA: ****$p < 0.0001$, Sham *vs* Casp3 A68930: ****$p < 0.0001$, Casp3 Veh *vs* Casp3 L-DOPA: ***$p = 0.0003$, Casp3 Veh *vs* Casp3 A68930: ***$p = 0.0006$, with Turkey's) and NLRP3 levels (One-Way ANOVA: $F_{3,26} = 254$; $p < 0.0001$. Sham *vs* Casp3 Veh: ****$p < 0.0001$, Casp3 Veh *vs* Casp3 L-DOPA: ****$p < 0.0001$, Casp3 Veh *vs* Casp3 A68930: ****$p < 0.0001$, with Turkey's). **E)** Confocal images of IL-1β and Iba1 (scale: 15 μm) and plot of IL-1β levels (Sham: n = 6; Casp3 Veh: n = 7, Casp3 L-DOPA: n = 8, Casp3 A68930: n = 9 mice; One-Way ANOVA: $F_{3,26} = 8.224$; $p = 0.0005$. Sham *vs* Casp3 Veh: **$p = 0.001$, Casp3 Veh *vs* Casp3 L-DOPA: **$p = 0.003$, Casp3 Veh *vs* Casp3 A68930: **$p = 0.003$, with Turkey's). Figure adapted from[136]

Similarly, the chronic treatment of Casp3 mice with the selective 5-HT reuptake inhibitor (SSRI) fluoxetine, started one day after lesioning and continued for 30 days (**Figure 14A**), prevented microglia reactivity as shown by the reduced number and morphological complexity of $Iba1^+$ cells compared to vehicle-treated Casp3 mice, reaching those of Sham mice (**Figure 14B,C**). Fluoxetine also attenuated the activation of the NLRP3 pathway, as demonstrated by the lower percentage of $NLRP3^+/Iba1^+$ cells and the lower levels of NLRP3 and IL-1β compared to vehicle-treated Casp3 mice (**Figure 14D,E**). Collectively, these results indicate that both dopaminergic and serotonergic treatments can protect Casp3 mice from NLRP3-mediated neuroinflammation (**Figure 14F**).

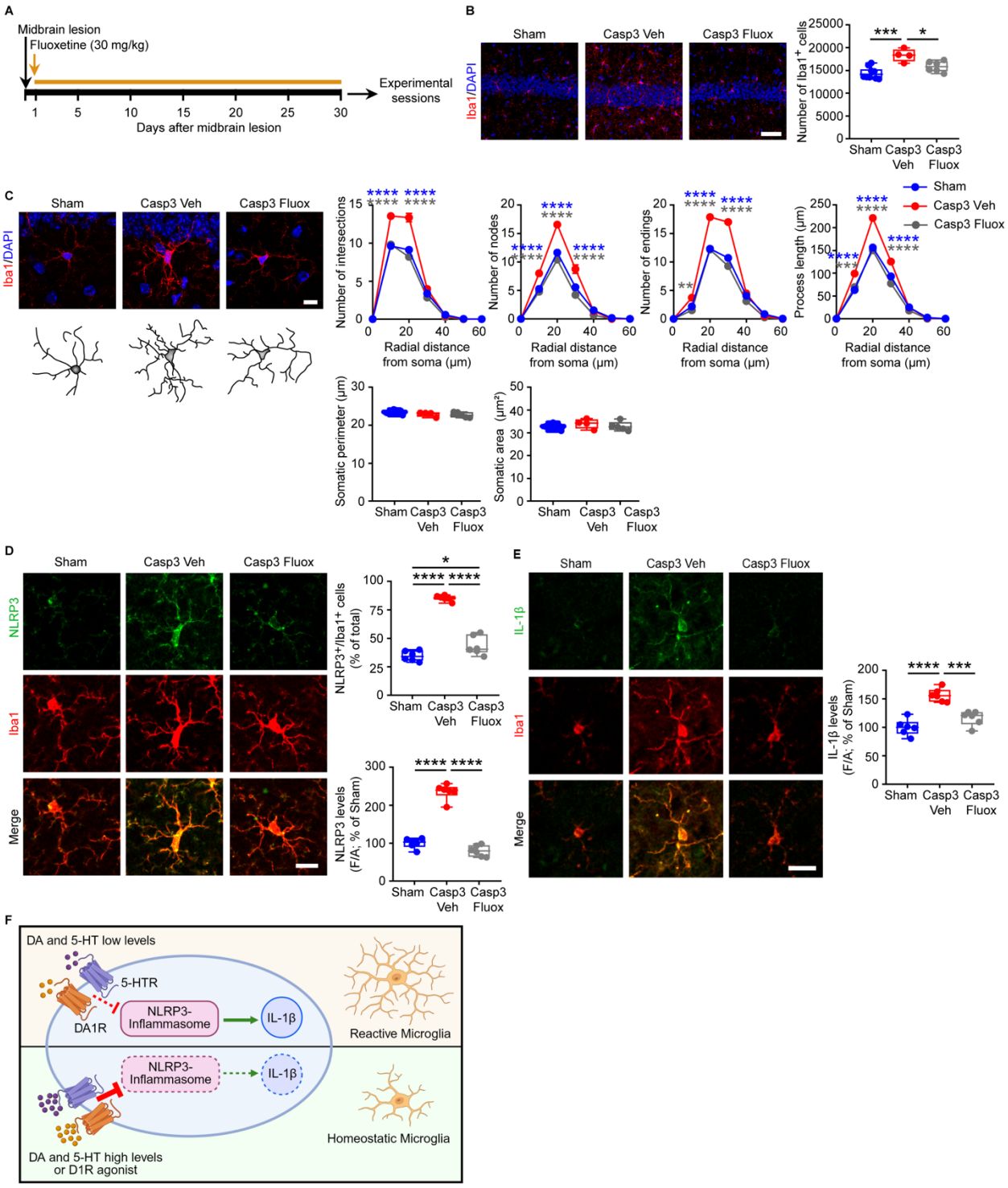

Figure 14: Fluoxetine prevents microglia-mediated neuroinflammation in the Casp3 hippocampus. A) Experimental procedure for chronic treatment with or without fluoxetine in drinking water (30 mg/kg; 30 days) in Casp3 mice. **B)** Confocal images and plot showing stereological cell count of hippocampal Iba1^{+} cells (scale: 50 µm) in Sham mice and in Casp3 mice drinking normal water (Veh) or water containing fluoxetine (Fluox; Sham: n = 10, Casp3 Veh: n = 4, Casp3 Fluox: n = 6 mice; One-way ANOVA: $F_{2,17} = 14.05$; p = 0.0003; Sham *vs* Casp Veh: ***p = 0.0002; Casp3 Veh *vs* Casp3 Fluox: *p = 0.018, with Tukey's multiple comparisons test). Nuclei are counterstained with DAPI. **C)** Representative images and 3D-reconstruction of microglia in Sham and Casp3 mice treated with Veh or Fluox (scale: 10 µm). The graph shows number of intersections (Sham: n = 10, Casp3 Veh: n = 4, Casp3 Fluox: n = 5 mice. Two-way RM-ANOVA: interaction $F_{12,96} = 25.84$, p < 0.0001; distance $F_{6,96} = 1559$, p < 0.0001; treatment

$F_{2,16} = 33.80$, $p < 0.0001$; Sham *vs* Casp3 Veh (blue): ****$p < 0.0001$ at 10-20 μm; Casp3 Veh *vs* Casp3 Fluox (grey): ****$p < 0.0001$ at 10-20 μm, analysed with Tukey's multiple comparisons test). **D)** Confocal images of NLRP3 and Iba1 in the hippocampus (scale: 15 μm). The plot shows: the % of $NLRP3^+/Iba1^+$ cells (n = 6 mice / group; One-way ANOVA: $F_{2,15} = 137$; $p < 0.0001$; Sham *vs* Casp Veh: ****$p < 0.0001$; Casp3 Veh *vs* Casp3 Fluox: ****$p < 0.0001$, Sham *vs* Casp3 Fluox: *$p = 0.034$; with Tukey's multiple comparisons test) and NLRP3 levels (One-way ANOVA: $F_{2,15} = 157.3$; $p < 0.0001$; Sham *vs* Casp Veh: ****$p < 0.0001$; Casp3 Veh *vs* Casp3 Fluox: ****$p < 0.0001$; with Tukey's multiple comparisons test). **E)** Confocal images of IL-1β and Iba1 (scale: 15 μm) and plot of IL-1β levels (n = 6 mice / group; One-way ANOVA: $F_{2,15} = 30.09$; $p < 0.0001$; Sham *vs* Casp Veh: ****$p < 0.0001$; Casp3 Veh *vs* Casp3 Fluox: ***$p = 0.0002$; with Tukey's multiple comparisons test). **F)** Schematic representation of DA and 5-HT role in microglia. Deprivation of both monoamines triggers NLRP3 inflammasome activation in microglia, promoting IL-1β release. Intervention with dopaminergic (L-DOPA or A68930) or serotonergic (Fluox) drugs inhibits NLRP3-mediated microglia reactivity, reducing IL-1β release. Figure adapted from[136]

4.3 Midbrain lesion in the Tg2576 mouse model worsens hippocampal microglia reactivity

To evaluate the impact of DA and 5-HT deprivation on hippocampi that are accumulating soluble Aβ, a condition that may mirror the preclinical stage of human AD, we examined the microglial response in naïve Tg2576 mice (**Figure 15**) and in Tg2576 mice with midbrain lesions (Tg Casp3, **Figure 16**), induced by the same experimental approach as for C57BL/6N mice. We used Tg2576 mice at 7 months of age, an time-point at which we previously documented a partial loss of VTA DA neurons, leading to reduced hippocampal DA outflow associated with neuronal loss, as well as synaptic and behavioural deficits[45,90,91,140].

To assess whether the hippocampus of naïve Tg2576 mice (**Figure 15A**) exhibits microglia reactivity, we examined microglia density and morphological changes. We found a greater number of $Iba1^+$ cells in Tg2576 mice (**Figure 15B**). These cells had also an increased number of intersections, nodes, endings, and processes length, as well as a significant soma enlargement (**Figure 15C-E**) accompanied by enhanced CD68 immunoreactivity (**Figure 15F**). Furthermore, we observed a significant increase in the percentage of $NLRP3^+/Iba1^+$ cells in Tg2576 compared to WT mice, along with increased microglia NLRP3, IL-1β and IL-18 immunoreactivity (**Figure 15G-I**). Collectively, these data indicate that Tg2576 mice exhibit hippocampal

neuroinflammation mediated by microglia through the activation of the NLRP3 inflammasome pathway, which coincides with the loss of DA signalling from the VTA.

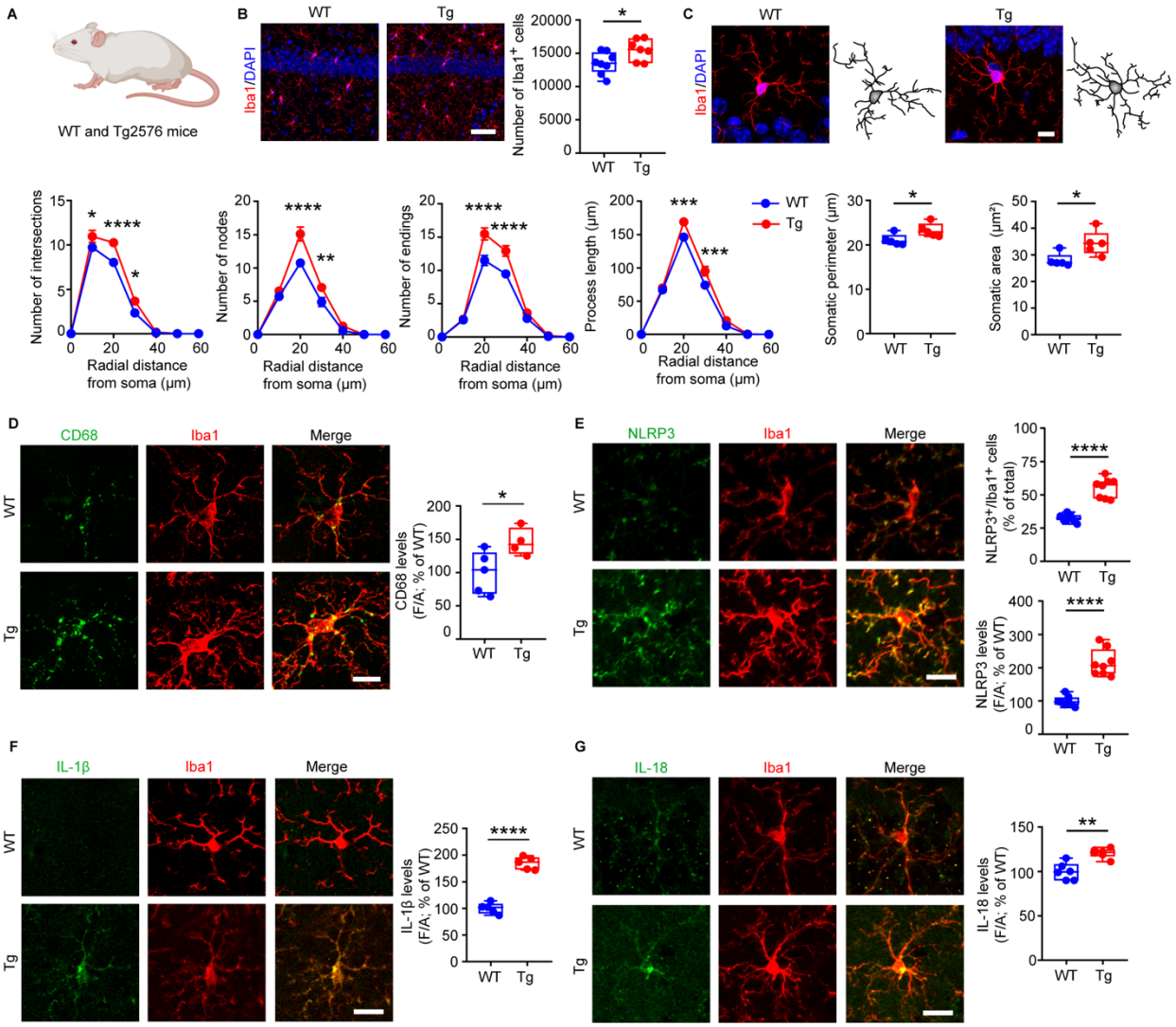

Figure 15: Mild hippocampal microglia reactivity in 7-month-old naïve Tg2576 mice. A) Evaluation of hippocampal neuroinflammatory processes in wild-type (WT) mice and in naïve pre-plaque Tg2576 (Tg) mice at 7 months of age. **B)** Confocal images and plot showing cell count of Iba1$^+$ cells in WT and Tg hippocampi (scale: 50 µm. WT: n = 8, Tg: n = 7 mice. Unpaired *t*-test: *p = 0.031). Nuclei are counterstained with DAPI. **C)** Representative images and 3D-reconstruction of microglia (scale: 10 µm). The graph shows Sholl analysis of intersections (n = 5 mice / group; Two-way RM-ANOVA: interaction $F_{6,48} = 4.832$, p = 0.0006; distance $F_{6,48} = 516.1$, p < 0.0001; genotype $F_{1,8} = 11.20$, p = 0.010; WT *vs* Tg2576: *p = 0.041 at 10 µm; ****p < 0.0001 at 20 µm; *p = 0.023 at 30 µm, analysed with Sidak's multiple comparisons test). Nuclei are counterstained with DAPI. **D)** Confocal images of CD68 and Iba1 immunostaining (scale: 10 µm), and plot showing CD68 immunostaining intensity in microglia cell body (WT: n = 5; Tg2576: n = 4 mice. Unpaired *t*-test: *p = 0.042). **E)** Confocal images of NLRP3 and Iba1 immunostaining (scale: 15 µm). The plots show: the % of NLRP3$^+$/Iba1$^+$ cells (n = 8 mice / group; Welch's *t*-test: ****p < 0.0001) and NLRP3 levels (Welch's *t*-test: ****p < 0.0001). **F)** Confocal images of IL-1β and Iba1 immunostaining (scale: 15 µm), and plot showing IL-1β levels in the hippocampus (n = 8 mice / group. Unpaired *t*-test: ****p < 0.0001). **G)** Confocal

images of IL-18 and Iba1 immunostaining (scale: 15 μm), and plot showing hippocampal IL-18 levels (n = 6 mice / group. Unpaired *t*-test: **p = 0.001). Figure adapted from[136]

To validate our hypothesis that the enhanced loss of midbrain monoamines could aggravate the microglia response, we next examined Tg Casp3 mice, generated by unilateral co-infusion of the AAV1-THp-iCre and AAV5-flex-taCasp3-TEVp viruses into the left midbrain of 6-month-old Tg2576 mice (**Figure 16A**). Consistent with the evidence that DA and 5-HT deficiency triggers microglia-mediated neuroinflammation in the hippocampus of C57BL/6N mice (see **Figure 8**), the lesion significantly exacerbated the microglia response in Tg Casp3 compared to Tg Sham mice. Specifically, stereological cell counting and Sholl analysis of $Iba1^+$ cells in Tg Casp3 mice one month post-lesion revealed an increase in cell numbers and hyper-ramification of microglia processes (**Figure 16B,C**). Additionally, $Iba1^+$ cells of Tg Casp3 mice showed significantly higher NLRP3, IL-1β and IL-18 immunoreactivity compared to Tg Sham mice (**Figure 16D-F**), indicating a worsened pro-inflammatory microglial state.

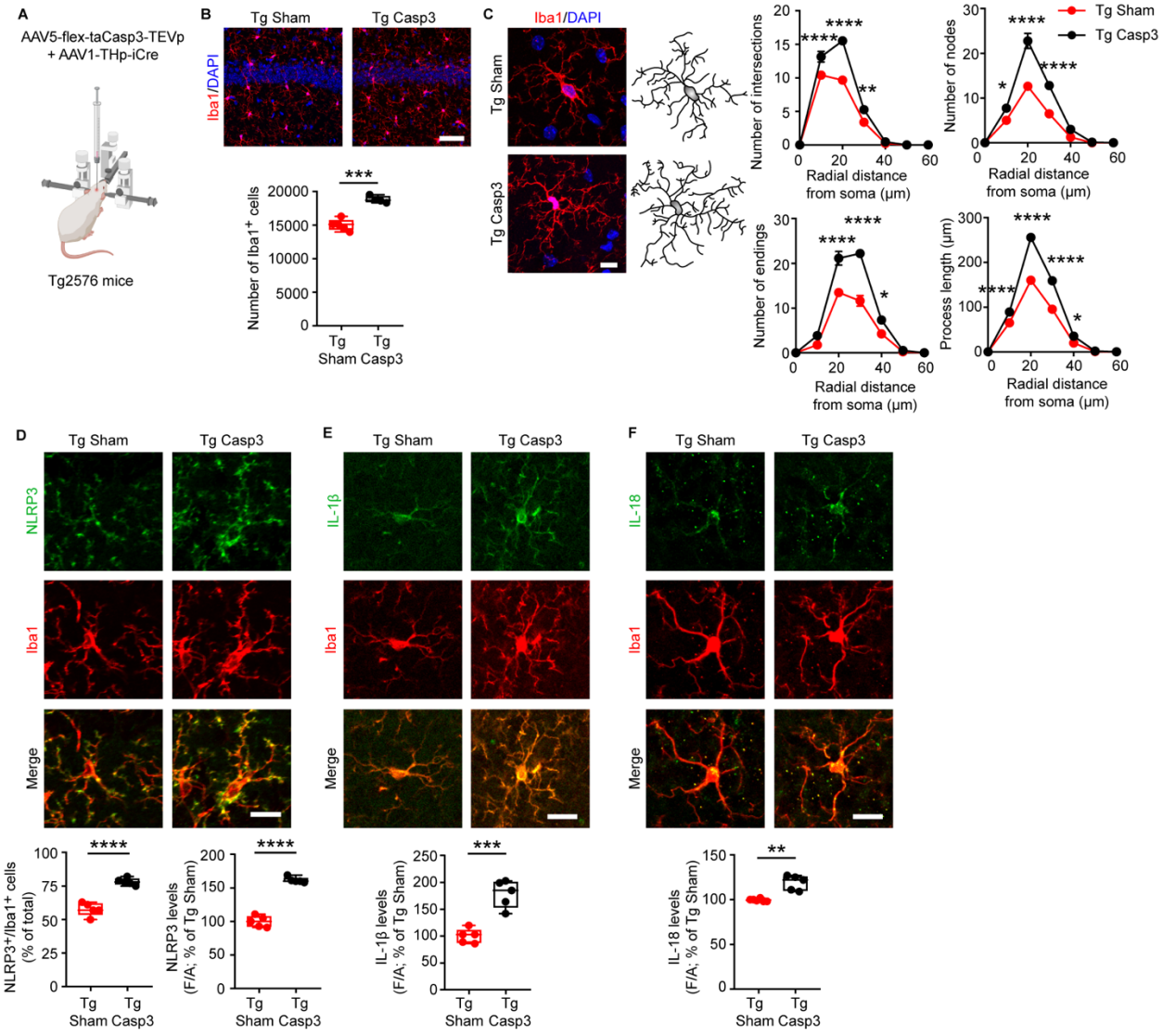

Figure 16: Midbrain lesion exacerbates microglia reactivity in the hippocampus of Tg Casp3 mice. A) Schematic representation of the midbrain lesion in 6-month-old Tg mice, using the dual AAV approach. Mice were analysed 1-month after lesion. **B)** Confocal images and plot showing cell count of Iba1^{+} cells in Tg Sham and Tg Casp3 hippocampi (scale: 50 µm. Tg Sham: n = 5 and Tg Casp3: n = 4 mice; Unpaired *t*-test: ***p = 0.0001). Nuclei are counterstained with DAPI. **C)** Representative images and 3D-reconstruction of microglia (scale: 10 µm). The graph shows Sholl analysis of microglia intersections (n = 5 mice / group; Two-way RM-ANOVA: interaction $F_{6,48} = 16.34$, p < 0.0001; distance $F_{6,48} = 437$, p < 0.0001; lesion $F_{1,8} = 47.90$, p = 0.0001; Tg Sham *vs* Tg Casp3: ****p < 0.0001 at 10-20 µm; **p = 0.008 at 30 µm, analysed with Sidak's multiple comparisons test). **D)** Confocal images of NLRP3 and Iba1 (scale: 15 µm). The plots show: % of NLRP3^{+}/Iba1^{+} cells (n = 5 mice / group; Unpaired *t*-test: ****p < 0.0001) and NLRP3 levels (Unpaired *t*-test: ****p < 0.0001). **E)** Confocal images of IL-1β and Iba1 (scale: 15 µm), and plot showing hippocampal IL-1β levels (n = 5 mice / group; Unpaired *t*-test: ***p = 0.0003). **F)** Confocal images of IL-18 and Iba1 (scale: 15 µm) and IL-18 levels (Tg Sham: n = 6, Tg Casp3: n = 5 mice; Unpaired *t*-test: **p = 0.006). Figure adapted from[136]

4.4 Midbrain lesion in Tg mice triggers astrocyte reactivity, tau hyperphosphorylation and Aβ plaque deposition

Previous studies have shown that reactive microglia can activate astrocytes, which in turn, participate in the inflammatory response by activating the NFκB pathway, leading to the release of complement 3 (C3). This cascade can further enhance the microglia reactivity impairing Aβ phagocytosis, and can promote Aβ and tau pathology in neurons[163–167]. Here, we explored the hypothesis that in Tg Casp3 mice the severe microglia reactivity induced by the midbrain lesion can lead to astrocytic response and, thus, trigger the pathogenic cycle described above.

Before doing so, we examined astrocyte reactivity in the hippocampus of naïve Tg2576 mice. Unlike microglia (see **Figure 15**), astrocytes do not appear to be responsive in naïve Tg2576 at 7 months of age, as shown by count of $GFAP^+$ cells, and the absence of NLRP3 immunoreactivity (**Figure 17A,B**). Additionally, we examined the microglia-astrocyte crosstalk pathway involving the activation of the IL-18R in astrocytes and the subsequent phosphorylation of NFκB [168]. Consistently with the absence of astrocyte reactivity in the naïve Tg2576 hippocampus, confocal analysis of IL-18R and p-NFκB in astrocytes (immunolabelled by GFAP or S100β) revealed comparable numbers of astrocytes expressing IL-18R and p-NFκB between Tg2576 and WT mice (**Figure 17C,D**).

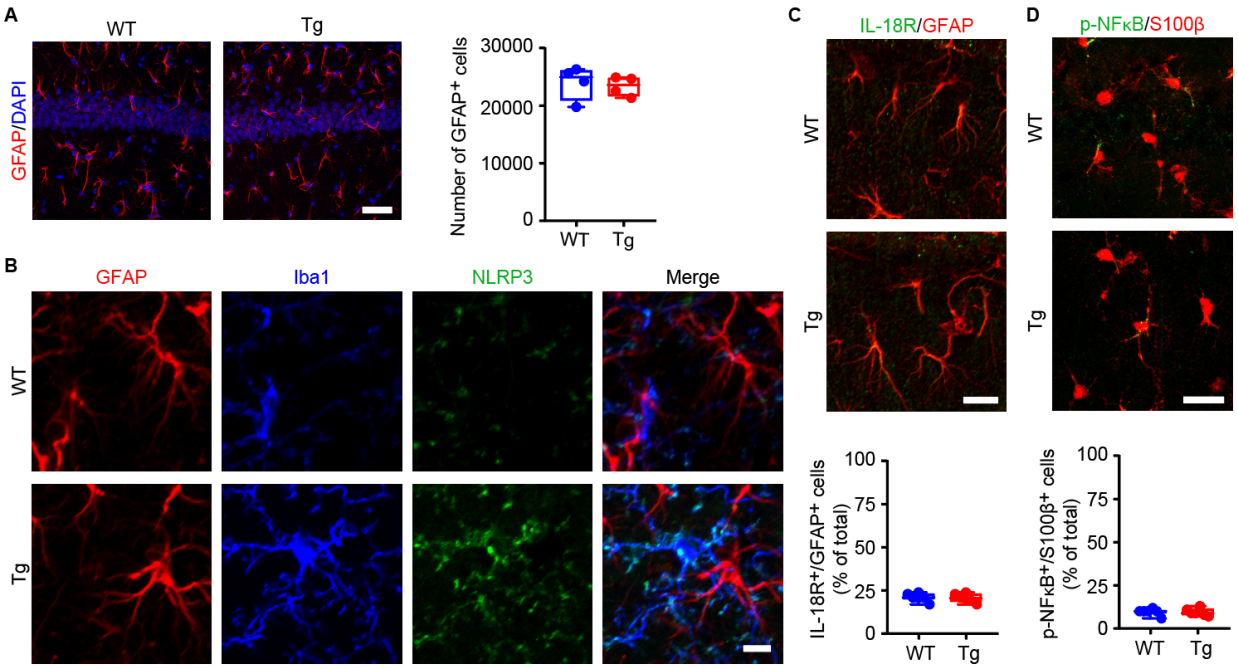

Figure 17: Additional analysis of neuroinflammation in WT, Tg2576 naïve, and in Tg Sham and Tg2576 Casp3 mice. A) Representative confocal images and plot showing stereological cell count of GFAP$^+$ cells in the hippocampus of WT and Tg2576 mice (n = 4 mice / group; scale: 50 µm). Nuclei are counterstained with DAPI. **B)** Representative confocal images of GFAP$^+$ cells, Iba1, and NLRP3 in the hippocampus of WT and Tg2576 mice (n = 3 mice / group; scale: 10 µm). **C)** Representative confocal images of GFAP and IL-18R, and plot showing the % of IL-18R$^+$/GFAP$^+$ cells in the hippocampus of WT and Tg2576 mice (n = 6 mice / group; scale: 20 µm). Figure adapted from[136]

We observed a different scenario in Tg Casp3 mice. Specifically, the enhanced NLRP3 inflammasome activity in microglia of Tg Casp3 mice was associated with an increased number of astrocytes and a higher portion of astrocytes expressing IL-18R and p-NFκB (**Figure 18A-C**). Furthermore, astrocytes from Tg Casp3 mice showed increased C3 immunoreactivity (**Figure 18D**), suggesting a pro-inflammatory activation.

To further investigate the astrocyte-neuron and astrocyte-microglia crosstalk in Tg Casp3 mice in response to elevated astrocytic C3, we assessed the C3a receptor (C3aR) levels in hippocampal CA1 pyramidal neurons and microglia. Both cell types exhibited an approximately two-fold increase in C3aR immunoreactivity (**Figure 18E**), which, in the case of microglia, may explain the exacerbated microglial response observed in Tg Casp3 compared to Tg Sham mice (see **Figure 16**).

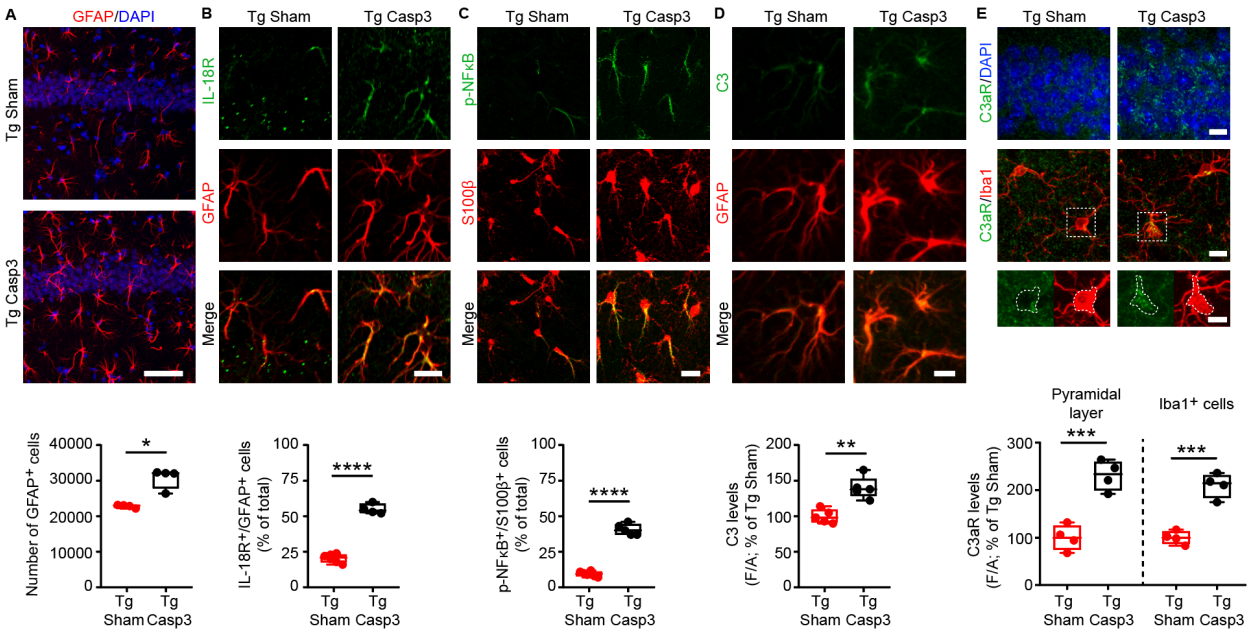

Figure 18: Reactive astrocytes, tau and Aβ pathology in Tg Casp3 mice. A) Stereological cell count of GFAP$^+$ cells in the hippocampus (scale: 50 µm) of Tg Sham and Tg Casp3 mice (n = 4 mice / group; Mann-Whitney test: *p = 0.029). Nuclei are counterstained with DAPI. **B)** IL-18R and GFAP immunostaining (scale: 15 µm), and plot showing % of IL-18R$^+$/GFAP$^+$ cells (Tg Sham: n = 6, Tg Casp3: n = 4 mice; Unpaired t-test: ****p < 0.0001). **C)** p-NFκB and S100β immunostaining (scale: 15 µm) and plot showing % of p-NFκB$^+$/S100β$^+$ cells in hippocampus (Tg Sham: n = 6, Tg Casp3: n = 5 mice; Unpaired t-test: ****p < 0.0001). **D)** Complement C3 and GFAP immunostaining (scale: 10 µm), and plot showing C3 levels (n = 5 mice / group; Unpaired *t*-test: **p = 0.001). **E)** Complement C3aR and DAPI (scale: 20 µm) or Iba1 immunostaining (scale: 20 µm, inset 10 µm), and plots showing C3aR levels on neurons (n = 4 mice / group; Unpaired *t*-test: ***p = 0.0007) and microglia (Unpaired *t*-test: ***p = 0.0003). Figure adapted from[136]

The astrocyte-neuron communication *via* the intracellular C3 pathway has been shown to drive Aβ and tau pathology as well as synaptic dysfunction in neurons, potentially through modulation of different kinases, including GSK3β and the Mitogen-Activated Protein Kinases (MAPKs) such as JNK and p38[163,164,169,170]. We therefore quantified the phosphorylated levels of GSK3β, JNK and p38 and observed a significant reduction of p-GSK3β, indicating an increased GSK3β activity in Tg Casp3 compared to Tg Sham mice (**Figure 19A**). Given the known role of GSK3β in the progression of tau pathology[171,172], we next evaluated tau hyperphosphorylation (immunolabelled with the AT8 antibody). We found a stronger AT8 immunoreactivity in the hippocampus of Tg Casp3 mice, associated with enhanced intracellular levels of hyperphosphorylated tau (**Figure 19B**). Of note, the levels of phosphorylated tau in the hippocampus of 7-month-old Tg Sham mice

are similar to those of WT littermates (**Figure 19B**), suggesting that midbrain lesion in APPSwe mice drives secondary tau pathology. The increased activity of GSK3β has also been associated with reduced microtubule stabilization and aggravated Aβ pathology[173,174]. Accordingly, we found a diffuse reduction of the dendritic MAP2 in pyramidal neurons of Tg Casp3 mice, suggestive of pathological changes in dendritic integrity (**Figure 19C**), and increased intracellular Aβ levels (**Figure19D**), paralleled by the appearance of precocious Aβ plaque accumulation (**Figure 19E**).

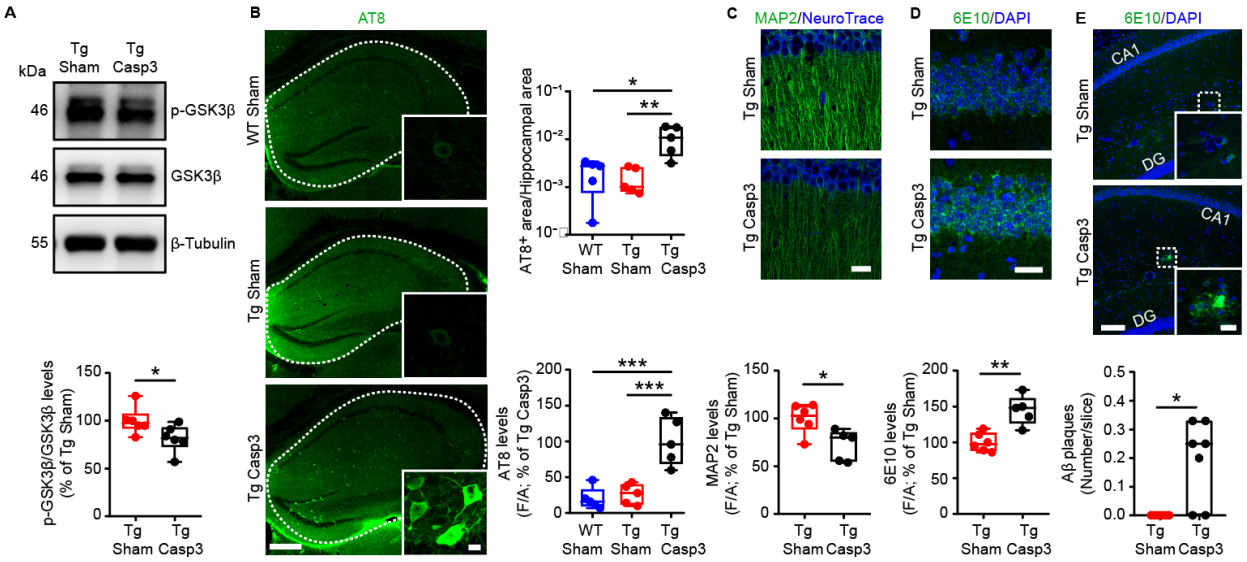

Figure 19: DA and 5-HT depletion induces tau and Aβ pathology in Tg Casp3 mice. A) Representative western blots and plot showing levels of p-GSK3β/GSK3β (as % of Tg Sham). β-Tubulin was used as loading control (n = 6 mice/group; Unpaired *t*-test: *p = 0.048). **B)** AT8 immunostaining in WT, Tg Sham and Tg Casp3 hippocampi and plot showing AT8^{+} area on total hippocampal area (scale bar: 250 µm; n = 5 mice / group. One-Way ANOVA: $F_{2,12}$ = 8.817; p = 0.004. WT Sham *vs* Tg Casp3: *p = 0.011, Tg Sham *vs* Tg Casp3: **p = 0.007, with Turkey's). The insets and bottom plot show AT8-reactive cells and AT8 levels (scale: 20 µm; n = 5 mice / group. One-Way ANOVA: $F_{2,12}$ = 19.27; p = 0.0002. WT *vs* Tg Casp3: ***p = 0.0003, Tg Sham *vs* Tg Casp3: ***p = 0.0007, with Turkey's). **C)** MAP2 immunostaining and plot showing MAP2 levels (counterstained with NeuroTrace; scale: 25 µm; Tg Sham: n = 6, Tg Casp3: n = 5 mice; Unpaired *t*-test: *p = 0.017). **D)** 6E10 immunostaining and plot of intracellular Aβ levels (Tg Sham: n = 6, Tg Casp3: n = 5 mice; Unpaired *t*-test: **p = 0.002). Nuclei are counterstained with DAPI (scale: 50 µm). **E)** Immunostaining for Aβ plaques and Iba1 (scale: 100 µm, inset 20 µm), and plot reporting hippocampal Aβ plaque load (n = 7 mice / group; Mann-Whitney test: *p = 0.021). Figure adapted from[136]

4.5 Astrocyte reactivity and tau pathology in Tg Casp3 mice are mitigated by dopaminergic or serotonergic treatment

To evaluate whether restoring the monoaminergic tone could reduce the astrocyte response and tau hyperphosphorylation in the context of AD, we treated Tg Casp3 mice with L-DOPA (4-day treatment) or fluoxetine (initiated one day post-lesion). Both interventions markedly attenuated the hippocampal astrocytic response, as evidenced by a significant reduction in $GFAP^+$ cell number compared to Tg Casp3 mice treated with vehicle (**Figure 20A; Figure 21A**).

Concomitantly, IL-18 expression in microglia was suppressed (**Figure 20B, Figure 21B**), and this was accompanied by a reduced portion of astrocytes expressing IL-18R and p-NFκB (**Figure 20C-D** and **Figure 21C-D**). Astrocytic C3 immunoreactivity was also markedly decreased after treatments (**Figure 20E and Figure 21E**). Crucially, AT8 immunostaining revealed a significant reduction in hippocampal hyperphosphorylated tau in treated Tg Casp3 mice (**Figure 20F and Figure 21F**).

Collectively, these results demonstrate that both dopaminergic and serotonergic treatments effectively suppress microglial pro-inflammatory cytokine release, astrocyte reactivity and the downstream tau hyperphosphorylation in the hippocampus of Tg Casp3 mice.

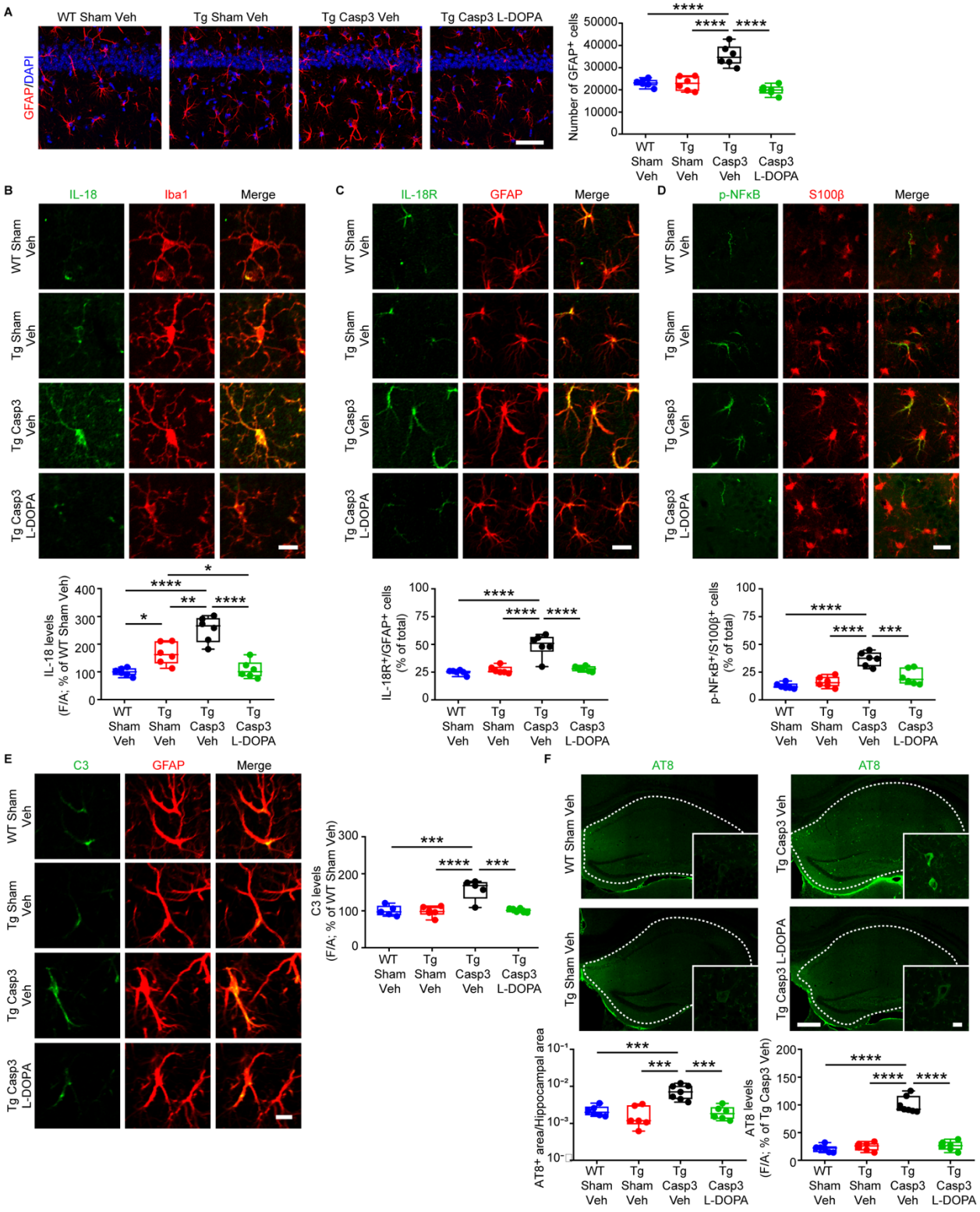

Figure 20: L-DOPA treatment attenuates astrocyte reactivity and tau pathology in Tg Casp3 mice. A) Representative figures (scale: 50 µm) and plot showing stereological count of GFAP$^+$ cells in the hippocampus of WT Sham, Tg Sham and Tg Casp3 mice treated with vehicle (Veh) and Tg Casp3 mice treated with L-DOPA (n = 6 mice / group; One-Way ANOVA: $F_{3,20} = 28.83$; $p < 0.0001$. WT Sham Veh *vs* Tg Casp3 Veh ****$p < 0.0001$, Tg Sham Veh *vs* Tg Casp3 Veh: ****$p < 0.0001$, Tg Casp3 Veh *vs* Tg Casp3 L-DOPA: ****$p < 0.0001$; with Turkey's). Nuclei are counterstained with DAPI. **B)** Confocal images of IL-18 and Iba1 (scale: 15 µm) and plot showing IL-18 levels

following Veh or L-DOPA treatment (n = 6 mice / group; One-Way ANOVA: $F_{3,20} = 24.71$; $p < 0.0001$. WT Sham Veh *vs* Tg Sham Veh: *p = 0.018, WT Sham Veh *vs* Tg Casp3 Veh ****p < 0.0001, Tg Sham Veh *vs* Tg Casp3 Veh: **p = 0.002, Tg Sham Veh *vs* Tg Casp3 L-DOPA *p = 0.044, Tg Casp3 Veh *vs* Tg Casp3 L-DOPA: ****p < 0.0001; with Turkey's). Nuclei are counterstained with DAPI. **C)** IL-18R and GFAP immunostaining (scale: 10 µm), and plot showing % of $IL\text{-}18R^{+}/GFAP^{+}$ cells following Veh or L-DOPA treatment (n = 6 mice / group; One-Way ANOVA: $F_{3,20} = 23.92$; $p < 0.0001$. WT Sham Veh *vs* Tg Casp3 Veh ****p < 0.0001, Tg Sham Veh *vs* Tg Casp3 Veh: ****p < 0.0001, Tg Casp3 Veh *vs* Tg Casp3 L-DOPA: ****p < 0.0001; with Turkey's). Nuclei are counterstained with DAPI. **D)** p-NFκB and S100β immunostaining (scale: 20 µm) and plot showing % of $p\text{-}NF\kappa B^{+}/S100\beta^{+}$ cells in the hippocampus following Veh or L-DOPA treatment (n = 6 mice / group; One-Way ANOVA: $F_{3,20} = 22.92$; $p < 0.0001$. WT Sham Veh *vs* Tg Casp3 Veh: ****p < 0.0001, Tg Sham Veh *vs* Tg Casp3 Veh: ****p < 0.0001, Tg Casp3 Veh *vs* Tg Casp3 L-DOPA: ***p = 0.0003; with Turkey's). **E)** Complement C3 and GFAP immunostaining (scale: 10 µm), and plot showing C3 levels following Veh or L-DOPA treatment (WT Sham Veh: n = 5, Tg Sham Veh: n = 6, Tg Casp3 Veh: n = 5, Tg Casp3 L-DOPA: n = 6 mice; One-Way ANOVA: $F_{3,18} = 15.29$; $p < 0.0001$. WT Sham Veh *vs* Tg Casp3 Veh: ***p = 0.0002, Tg Sham Veh *vs* Tg Casp3 Veh: ****p < 0.0001, Tg Casp3 Veh *vs* Tg Casp3 L-DOPA: ***p = 0.0002; with Turkey's). **F)** AT8 immunostaining in WT Sham Veh, Tg Sham Veh, Tg Casp3 Veh and Tg Casp L-DOPA hippocampi and plot showing $AT8^{+}$ area on total hippocampal area (scale bar: 250 µm; WT Sham Veh: n = 6, Tg Sham Veh: n = 6, Tg Casp3 Veh: n = 7, Tg Casp L-DOPA: n = 6 mice / group. One-Way ANOVA: $F_{3,21} = 14.37$; $p < 0.0001$. WT Sham Veh *vs* Tg Casp3 Veh: ***p = 0.0003, Tg Sham Veh *vs* Tg Casp3 Veh: ***p = 0.0001, Tg Casp3 Veh *vs* Tg Casp L-DOPA: ***p = 0.0002, with Turkey's). The insets and bottom plot show AT8-reactive cells and AT8 levels (scale: 20 µm; One-Way ANOVA: $F_{3,21} = 94.83$; $p < 0.0001$. WT Sham Veh *vs* Tg Casp3 Veh: ****p < 0.0001, Tg Sham Veh *vs* Tg Casp3 Veh: ****p < 0.0001, Tg Casp3 Veh *vs* Tg Casp L-DOPA: ****p < 0.0001, with Turkey's). Figure from[136]

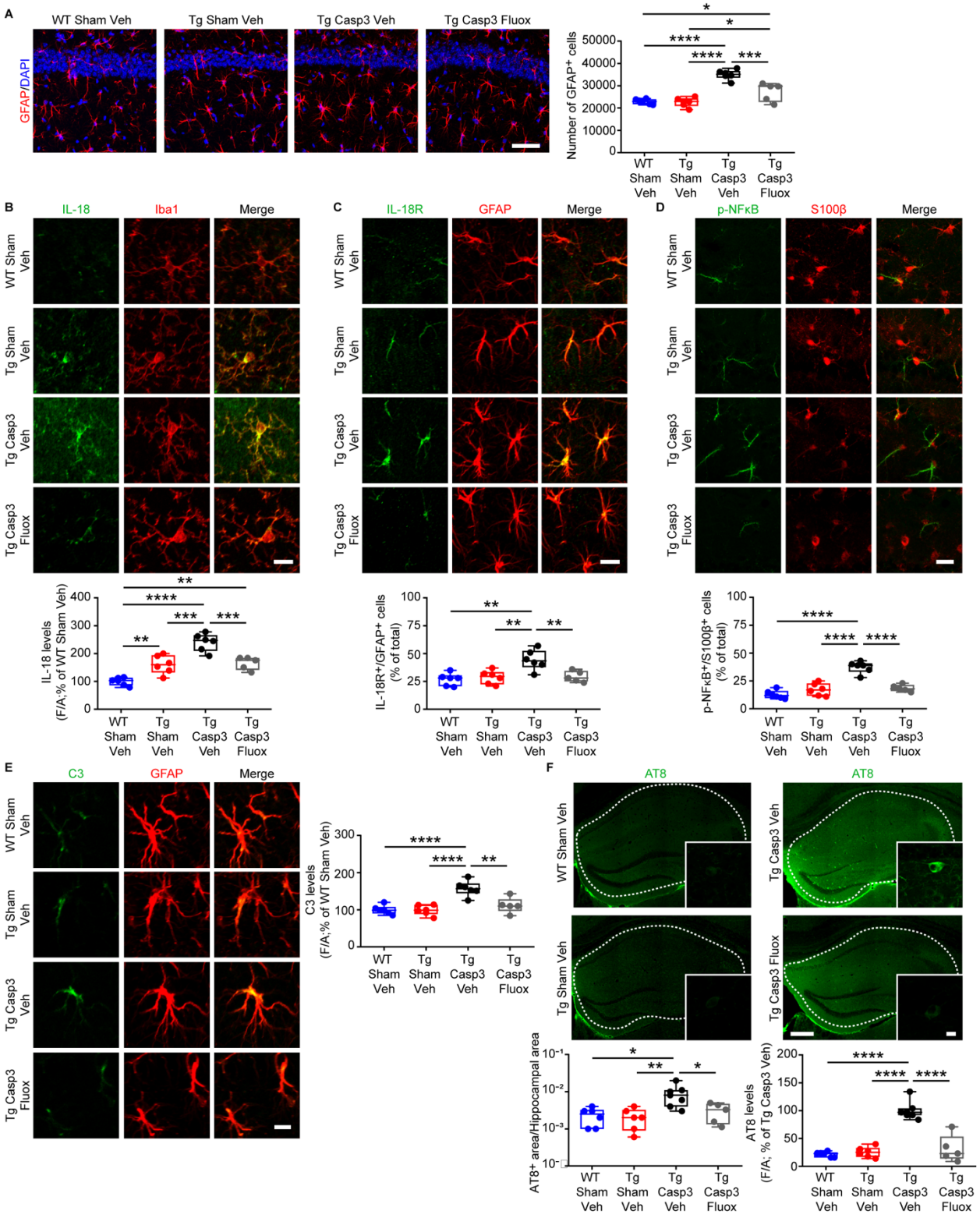

Figure 21: Fluoxetine treatment prevents astrocyte reactivity and tau pathology in Tg Casp3 mice. A) Representative figures (scale: 50 µm) and plot showing stereological count of GFAP$^+$ cells in the hippocampus of WT Sham, Tg Sham and Tg Casp3 mice drinking normal water (Veh) and Tg Casp3 mice drinking water containing fluoxetine (Fluox; WT Sham Veh: n = 6, Tg Sham Veh: n = 6, Tg Casp3 Veh: n = 6, Tg Casp3 Fluox: n = 5 mice; One-Way ANOVA: $F_{3,19} = 30.85$; $p < 0.0001$. WT Sham Veh *vs* Tg Casp3 Veh: ****$p < 0.0001$, WT Sham Veh *vs* Tg Casp3 Fluox: *$p = 0.050$, Tg Sham Veh *vs* Tg Casp3 Veh: ****$p < 0.0001$, Tg Sham Veh *vs* Tg Casp3 Fluox: *p

= 0.036, Tg Casp3 Veh *vs* Tg Casp3 Fluox: ***p = 0.0004; with Turkey's). Nuclei are counterstained with DAPI. **B)** Confocal images of IL-18 and Iba1 (scale: 15 µm) and plot showing IL-18 levels following Veh or Fluox treatment (WT Sham Veh: n = 6, Tg Sham Veh: n = 6, Tg Casp3 Veh: n = 6, Tg Casp3 Fluox: n = 5 mice; One-Way ANOVA: $F_{3,19} = 27.96$; $p < 0.0001$. WT Sham Veh *vs* Tg Sham Veh: **p = 0.005, WT Sham Veh *vs* Tg Casp3 Veh: ****p < 0.0001, WT Sham Veh *vs* Tg Casp3 Fluox: **p = 0.004, Tg Sham Veh *vs* Tg Casp3 Veh: ***p = 0.0003, Tg Casp3 Veh *vs* Tg Casp3 Fluox: ***p = 0.009; with Turkey's). **C)** IL-18R and GFAP immunostaining (scale: 10 µm), and plot showing % of $IL\text{-}18R^{+}/GFAP^{+}$ cells following Veh or Fluox treatment (WT Sham Veh: n = 6, Tg Sham Veh: n = 6, Tg Casp3 Veh: n = 6, Tg Casp3 Fluox: n = 5 mice; One-Way ANOVA: $F_{3,19} = 8.827$; $p = 0.0007$. WT Sham Veh *vs* Tg Casp3 Veh: **p = 0.001, Tg Sham Veh *vs* Tg Casp3 Veh: **p = 0.003, Tg Casp3 Veh *vs* Tg Casp3 Fluox: **p = 0.007; with Turkey's). **D)** p-NFκB and S100β immunostaining (scale: 20 µm) and plot showing % of $p\text{-}NF\kappa B^{+}/S100\beta^{+}$ cells following Veh or Fluox treatment (WT Sham Veh: n = 6, Tg Sham Veh: n = 6, Tg Casp3 Veh: n = 6, Tg Casp3 Fluox: n = 5 mice; One-Way ANOVA: $F_{3,19} = 33.70$; $p < 0.0001$. WT Sham Veh *vs* Tg Casp3 Veh: ****p < 0.0001, Tg Sham Veh *vs* Tg Casp3 Veh: ****p < 0.0001, Tg Casp3 Veh *vs* Tg Casp3 Fluox: ****p < 0.0001; with Turkey's). **E)** Complement C3 and GFAP immunostaining (scale: 10 µm), and plot showing C3 levels following Fluox treatment (WT Sham Veh: n = 6, Tg Sham Veh: n = 6, Tg Casp3 Veh: n = 6, Tg Casp3 Fluox: n = 5 mice; One-Way ANOVA: $F_{3,19} = 15.50$; $p < 0.0001$. WT Sham Veh *vs* Tg Casp3 Veh: ****p < 0.0001, Tg Sham Veh *vs* Tg Casp3 Veh: ****p < 0.0001, Tg Casp3 Veh *vs* Tg Casp3 Fluox: **p = 0.002; with Turkey's). **F)** AT8 immunostaining in WT Sham Veh, Tg Sham Veh, Tg Casp3 Veh and Tg Casp Fluox hippocampi and plot showing $AT8^{+}$ area on total hippocampal area (scale bar: 250 µm; WT Sham Veh: n = 6, Tg Sham Veh: n = 6, Tg Casp3 Veh: n = 7, Tg Casp Fluox: n = 5 mice / group. One-Way ANOVA: $F_{3,20} = 6.114$; $p = 0.004$. WT Sham Veh *vs* Tg Casp3 Veh: *p = 0.011, Tg Sham Veh *vs* Tg Casp3 Veh: **p = 0.008, Tg Casp3 Veh *vs* Tg Casp Fluox: *p = 0.036). The insets and right plot show AT8-reactive cells and AT8 levels (scale: 20 µm; One-Way ANOVA: $F_{3,20} = 41.32$; $p < 0.0001$. WT Sham Veh *vs* Tg Casp3 Veh: ****p < 0.0001, Tg Sham Veh *vs* Tg Casp3 Veh: ****p < 0.0001, Tg Casp3 Veh *vs* Tg Casp Fluox: ****p < 0.0001, with Turkey's). Figure from[136]

5. Discussion

Here, we provide two main results: i) in C57BL/6N mice, the combined loss of DA and 5-HT in the hippocampus induces microglia reactivity characterized by NLRP3 inflammasome activation and IL-1β release, that is considerably dampened by dopaminergic or serotonergic drugs; ii) in Tg2576 mice, the combined loss of DA and 5-HT triggers a greater microglia response, together with an abnormal astrocyte reactivity. In the Tg Casp3 hippocampus, reactive astrocytes foster the appearance of tau pathology and premature Aβ plaque formation (**Figure 22**).

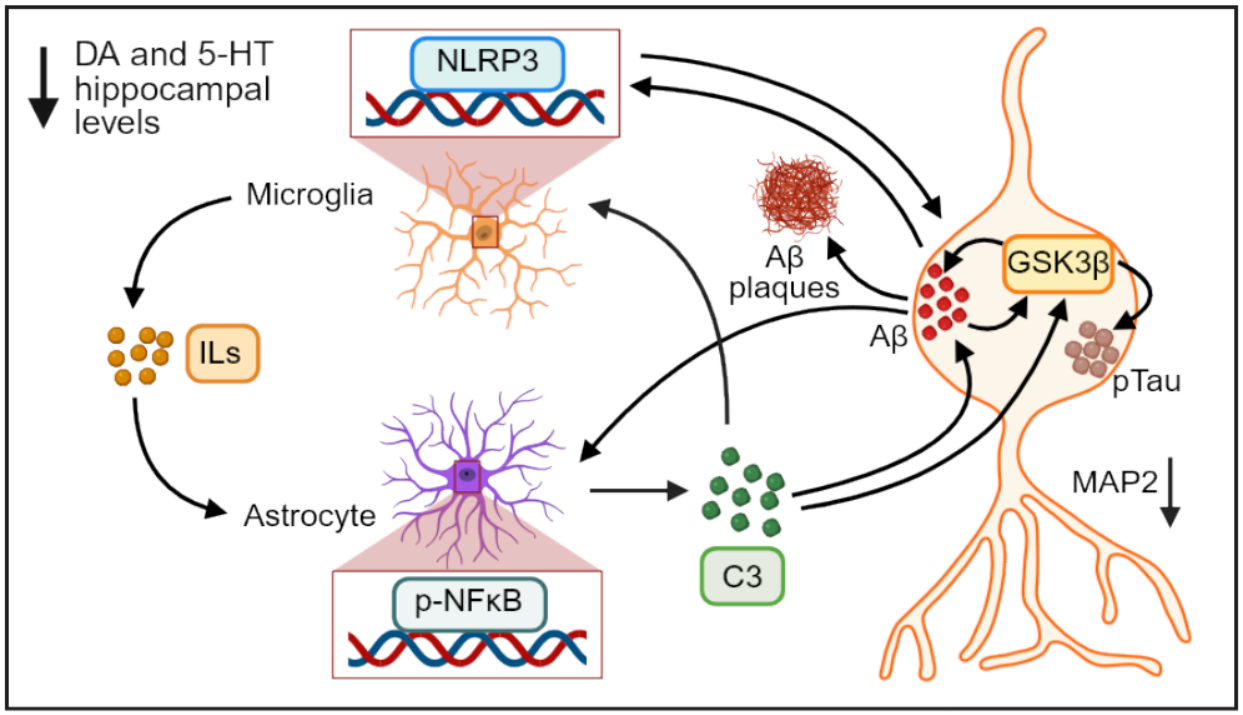

Figure 22: DA and 5-HT loss due to midbrain lesion triggers microglia-astrocyte-neuron crosstalk fostering neuroinflammation and, thus, exacerbating AD pathology in the hippocampus of Tg Casp3 mice. [Figure created using BioRender.com]. Figure from[136]

Crucially, pro-inflammatory cytokine release by microglia, astrocyte reactivity and tau hyperphosphorylation can all be significantly attenuated by L-DOPA or fluoxetine treatments.

Importantly, monoamine-driven neuroinflammation in Casp3 mice occurs independently of Aβ pathology. While in classic AD models (e.g., Tg2576, 3xTg-AD, 5xFAD) hippocampal microglia reactivity is typically attributed to Aβ plaque accumulation[175–177], these AD mice also exhibit early

midbrain degeneration and concomitant monoamine loss [45,91,142]. Nonetheless, the contribution of the monoamine depletion to neuroinflammation remains debatable if we consider the microglia response to Aβ[178,179]. Here, by selectively inducing monoaminergic loss in Aβ-naïve C57BL/6N mice, we demonstrate that combined DA/5-HT depletion is both necessary and sufficient to trigger NLRP3-dependent IL-1β release. Furthermore, our data distinguish microglia reactivity from downstream astrocyte activation: the microglia response emerges as an upstream event in the neuroinflammatory cascade and correlates with the onset of neuropsychiatric symptoms[175,180], whereas astrocyte reactivity appears more closely associated with Aβ-tau interactions[120,181–183].

Selective lesioning of either DA (6OHDA mice) or 5-HT (Casp3^{IPN} mice) alone, however, is insufficient to induce microglia-mediated neuroinflammation. Nonetheless, we found that fluoxetine entirely prevented the increase in NLRP3 and IL-1β levels in the hippocampus of Casp3 mice, in line with growing evidence that SSRI treatment can dampen neuroinflammatory responses [111,184,185]. Similarly, both L-DOPA and the selective D1 receptor agonist A68930 attenuated the microglia-mediated pro-inflammatory phenotype in Casp3 mice, consistent with reports highlighting that DA promotes NLRP3 ubiquitination and degradation, thereby curtailing IL-1β synthesis[65].

When dual monoamine deprivation was induced at the pre-plaque stage in Tg2576 mice, we observed an exacerbated microglial response accompanied by aberrant astrocyte reactivity. This key finding indicates that, in the context of ongoing Aβ pathology, the astrocyte response − and the resulting tau hyperphosphorylation in the hippocampus − critically depend on the reduced monoaminergic tone. Supporting this, treatment with either L-DOPA or fluoxetine significantly attenuated both astrocyte reactivity and hippocampal tau pathology in Tg Casp3 mice.

From a clinical perspective, these results resonate with three main observations. First, CSF and plasma GFAP levels are elevated in cognitively unimpaired individuals with positivity to brain

amyloid pathology, establishing astrocyte response as an early mediator linking Aβ accumulation to the downstream tauopathy (170). Second, reduced midbrain volumes observed on Magnetic Resonance Imaging are strongly correlated with faster progression from MCI to dementia due-to-AD, while early functional disconnection of these regions reliably predicts subsequent cognitive decline[83,95,96,131,187]. Third, DA-based therapies, such as L-DOPA/carbidopa, not only delay the progression from MCI to dementia, but also lower CSF levels of Aβ and tau in patients[188,189]. These effects are consistent with preclinical evidence that DA inhibits GSK-3β[190], up-regulates neprilysin[191] and promotes amyloid fibril disaggregation[192,193], thereby mitigating the neurotoxic environment. A similar function against AD pathology has been proposed for 5-HT and SSRIs, reducing amyloid load or tau pathology[111,194].

Here, the notion that deficits in monoaminergic nuclei may drive AD-relevant neuroinflammation and tau pathology supports the clinical studies linking Aβ to microglia and astrocyte reactivity and tau across the AD spectrum[195–198]. Furthermore, it may answer the unresolved question of why a significant number of Aβ-positive individuals do not develop tau pathology and thus remain cognitively unimpaired[199].

Our findings suggest that dysfunction in midbrain monoaminergic nuclei − key components of the "isodendritic core", known for their vulnerability in age-related neurodegenerative disorders − may actively drive AD-relevant astrocyte reactivity and downstream tau pathology[96,200–202]. By targeting the VTA, SNpc and IPN nuclei that collectively provide dopaminergic and serotonergic input to the hippocampus, we demonstrate that progressive midbrain degeneration triggers a cascade of neuroinflammatory, amyloidogenic and tau-related processes. These results extend the role of monoamines beyond behavioural modulation to the direct regulation of the mechanistic process determined by the glial and neuronal vulnerability. This underscores the therapeutic potential of preserving monoaminergic integrity as a strategy for early intervention in AD.

Overall, our study proves the direct involvement of midbrain monoamines in controlling hippocampal glial homoeostasis. The loss of dopaminergic and serotonergic input initiates NLRP3-dependent microglia reactivity, downstream astroglia activation, and drives tauopathy − a cascade that can be attenuated by restoring DA or 5-HT signalling. These results provide a mechanistic insight into how early midbrain degeneration may accelerate AD pathology. Clinically, our data resonate with evidence that individuals exhibiting reduced midbrain volumes experience more rapid progression from MCI to dementia, likely reflecting the loss of monoaminergic anti-inflammatory tone. These findings also highlight the importance of stratifying patients by midbrain integrity in clinical trials. More broadly, they support a precision-medicine paradigm in which early monoamine-restorative interventions could intercept neuroinflammation and glial dysregulation during the preclinical and/or prodromal AD phases, thereby slowing − or even halting − the manifestation/progression of cognitive symptoms. Such an approach holds considerable promise for restoring neuromodulatory control over vulnerable hippocampal circuits, and for modifying disease trajectory.

6. References

1. Villa, C., Lavitrano, M., Salvatore, E. & Combi, R. Molecular and Imaging Biomarkers in Alzheimer's Disease: A Focus on Recent Insights. *JPM* **10**, 61 (2020).
2. Jack, C. R. *et al.* NIA-AA Research Framework: Toward a biological definition of Alzheimer's disease. *Alzheimer's & Dementia* **14**, 535–562 (2018).
3. Pouryamout, L., Dams, J., Wasem, J., Dodel, R. & Neumann, A. Economic Evaluation of Treatment Options in Patients with Alzheimer's Disease: A Systematic Review of Cost-Effectiveness Analyses. *Drugs* **72**, 789–802 (2012).
4. Hardy, J. & Selkoe, D. J. The Amyloid Hypothesis of Alzheimer's Disease: Progress and Problems on the Road to Therapeutics. *Science* **297**, 353–356 (2002).
5. Shvetcov, A. *et al.* APOE ε4 carriers share immune-related proteomic changes across neurodegenerative diseases. *Nat Med* **31**, 2590–2601 (2025).
6. Huang, S., Wu, J. & He, L. APOE ε4 allele drives female-specific Alzheimer's disease progression via vascular dysfunction and tau spreading. *Front. Neurosci.* **19**, 1683204 (2025).
7. Tan, Y. *et al.* The Effect of *APOE* ε4 Allele on Dynamic Local Spontaneous Brain Activity and Functional Integration in Alzheimer's Disease. *Human Brain Mapping* **46**, e70269 (2025).
8. Krasemann, S. *et al.* The TREM2-APOE Pathway Drives the Transcriptional Phenotype of Dysfunctional Microglia in Neurodegenerative Diseases. *Immunity* **47**, 566-581.e9 (2017).
9. Livingston, G. *et al.* Dementia prevention, intervention, and care: 2020 report of the Lancet Commission. *The Lancet* **396**, 413–446 (2020).
10. Sperling, R. A. *et al.* Toward defining the preclinical stages of Alzheimer's disease: Recommendations from the National Institute on Aging-Alzheimer's Association workgroups on diagnostic guidelines for Alzheimer's disease. *Alzheimer's & Dementia* **7**, 280–292 (2011).
11. Olsson, B. *et al.* CSF and blood biomarkers for the diagnosis of Alzheimer's disease: a systematic review and meta-analysis. *The Lancet Neurology* **15**, 673–684 (2016).
12. Hunt, A. *et al.* Reduced cerebral glucose metabolism in patients at risk for Alzheimer's disease. *Psychiatry Research: Neuroimaging* **155**, 147–154 (2007).
13. Kumar, V., Kim, S.-H. & Bishayee, K. Dysfunctional Glucose Metabolism in Alzheimer's Disease Onset and Potential Pharmacological Interventions. *IJMS* **23**, 9540 (2022).

14. Sperling, R. A. *et al.* Association of Factors With Elevated Amyloid Burden in Clinically Normal Older Individuals. *JAMA Neurol* **77**, 735 (2020).
15. Jia, J. *et al.* Biomarker Changes during 20 Years Preceding Alzheimer's Disease. *N Engl J Med* **390**, 712–722 (2024).
16. Ismail, Z. *et al.* Neuropsychiatric symptoms as early manifestations of emergent dementia: Provisional diagnostic criteria for mild behavioral impairment. *Alzheimer's & Dementia* **12**, 195–202 (2016).
17. Alves, G. *et al.* Neuroimaging Findings Related to Behavioral Disturbances in Alzheimer's Disease: A Systematic Review. *CAR* **14**, 61–75 (2016).
18. Deimling, G. T. & Bass, D. M. Symptoms of Mental Impairment Among Elderly Adults and Their Effects on Family Caregivers. *Journal of Gerontology* **41**, 778–784 (1986).
19. Braak, H. & Braak, E. Neuropathological stageing of Alzheimer-related changes. *Acta Neuropathol* **82**, 239–259 (1991).
20. Mega, M. S., Cummings, J. L., Fiorello, T. & Gornbein, J. The spectrum of behavioral changes in Alzheimer's disease. *Neurology* **46**, 130–135 (1996).
21. Nelson, P. T. *et al.* Correlation of Alzheimer Disease Neuropathologic Changes With Cognitive Status: A Review of the Literature. *J Neuropathol Exp Neurol* **71**, 362–381 (2012).
22. Peters, M. E. *et al.* Neuropsychiatric Symptoms as Predictors of Progression to Severe Alzheimer's Dementia and Death: The Cache County Dementia Progression Study. *AJP* **172**, 460–465 (2015).
23. Mortby, M. E., Burns, R., Eramudugolla, R., Ismail, Z. & Anstey, K. J. Neuropsychiatric Symptoms and Cognitive Impairment: Understanding the Importance of Co-Morbid Symptoms. *Journal of Alzheimer's Disease* **59**, 141–153 (2017).
24. Villemagne, V. L. *et al.* Amyloid β deposition, neurodegeneration, and cognitive decline in sporadic Alzheimer's disease: a prospective cohort study. *The Lancet Neurology* **12**, 357–367 (2013).
25. Heneka, M. T. *et al.* Neuroinflammation in Alzheimer's disease. *The Lancet Neurology* **14**, 388–405 (2015).
26. Björklund, A. & Dunnett, S. B. Dopamine neuron systems in the brain: an update. *Trends in Neurosciences* **30**, 194–202 (2007).
27. Surmeier, D. J., Obeso, J. A. & Halliday, G. M. Selective neuronal vulnerability in Parkinson disease. *Nat Rev Neurosci* **18**, 101–113 (2017).

28. Costa, K. M. & Schoenbaum, G. Dopamine. *Current Biology* **32**, R817–R824 (2022).
29. Haber, S. N. & Knutson, B. The Reward Circuit: Linking Primate Anatomy and Human Imaging. *Neuropsychopharmacol* **35**, 4–26 (2010).
30. Grace, A. A. Dysregulation of the dopamine system in the pathophysiology of schizophrenia and depression. *Nat Rev Neurosci* **17**, 524–532 (2016).
31. Shohamy, D. & Adcock, R. A. Dopamine and adaptive memory. *Trends in Cognitive Sciences* **14**, 464–472 (2010).
32. Lisman, J. E. & Grace, A. A. The hippocampal-VTA loop: controlling the entry of information into long-term memory. *Neuron* **46**, 703–713 (2005).
33. Tsetsenis, T. *et al.* Midbrain dopaminergic innervation of the hippocampus is sufficient to modulate formation of aversive memories. *Proc. Natl. Acad. Sci. U.S.A.* **118**, e2111069118 (2021).
34. Takeuchi, T. *et al.* Locus coeruleus and dopaminergic consolidation of everyday memory. *Nature* **537**, 357–362 (2016).
35. Kempadoo, K. A., Mosharov, E. V., Choi, S. J., Sulzer, D. & Kandel, E. R. Dopamine release from the locus coeruleus to the dorsal hippocampus promotes spatial learning and memory. *Proc. Natl. Acad. Sci. U.S.A.* **113**, 14835–14840 (2016).
36. Wagatsuma, A. *et al.* Locus coeruleus input to hippocampal CA3 drives single-trial learning of a novel context. *Proc. Natl. Acad. Sci. U.S.A.* **115**, (2018).
37. Liu, C. & Kaeser, P. S. Mechanisms and regulation of dopamine release. *Current Opinion in Neurobiology* **57**, 46–53 (2019).
38. Xu, H., Baracskay, P., O'Neill, J. & Csicsvari, J. Assembly Responses of Hippocampal CA1 Place Cells Predict Learned Behavior in Goal-Directed Spatial Tasks on the Radial Eight-Arm Maze. *Neuron* **101**, 119-132.e4 (2019).
39. Kaufman, A. M., Geiller, T. & Losonczy, A. A Role for the Locus Coeruleus in Hippocampal CA1 Place Cell Reorganization during Spatial Reward Learning. *Neuron* **105**, 1018-1026.e4 (2020).
40. Nyberg, N., Duvelle, É., Barry, C. & Spiers, H. J. Spatial goal coding in the hippocampal formation. *Neuron* **110**, 394–422 (2022).
41. Schultz, W. Predictive Reward Signal of Dopamine Neurons. *Journal of Neurophysiology* **80**, 1–27 (1998).

42. Rosen, Z. B., Cheung, S. & Siegelbaum, S. A. Midbrain dopamine neurons bidirectionally regulate CA3-CA1 synaptic drive. *Nat Neurosci* **18**, 1763–1771 (2015).
43. Argyriou, S. *et al.* Beyond memory impairment: the complex phenotypic landscape of Alzheimer's disease. *Trends in Molecular Medicine* **30**, 713–722 (2024).
44. Wimber, M. *et al.* Prefrontal dopamine and the dynamic control of human long-term memory. *Transl Psychiatry* **1**, e15–e15 (2011).
45. Nobili, A. *et al.* Dopamine neuronal loss contributes to memory and reward dysfunction in a model of Alzheimer's disease. *Nat Commun* **8**, 14727 (2017).
46. Nobili, A., La Barbera, L. & D'Amelio, M. Targeting autophagy as a therapeutic strategy to prevent dopamine neuron loss in early stages of Alzheimer disease. *Autophagy* **17**, 1278–1280 (2021).
47. Cordella, A. *et al.* Dopamine loss alters the hippocampus-nucleus accumbens synaptic transmission in the Tg2576 mouse model of Alzheimer's disease. *Neurobiol. Dis.* **116**, 142–154 (2018).
48. La Barbera, L. *et al.* Upregulation of Ca2+-binding proteins contributes to VTA dopamine neuron survival in the early phases of Alzheimer's disease in Tg2576 mice. *Mol Neurodegener* **17**, 76 (2022).
49. Groenewegen, H. J. & Steinbusch, H. W. M. Serotonergic and non-serotonergic projections from the interpeduncular nucleus to the ventral hippocampus in the rat. *Neuroscience Letters* **51**, 19–24 (1984).
50. Montone, K. T., Fass, B. & Hamill, G. S. Serotonergic and nonserotonergic projections from the rat interpeduncular nucleus to the septum, hippocampal formation and raphe: A combined immunocytochemical and fluorescent retrograde labelling study of neurons in the apical subnucleus. *Brain Research Bulletin* **20**, 233–240 (1988).
51. Wirtshafter, D., Asin, K. E. & Lorens, S. A. Serotonin-immunoreactive projections to the hippocampus from the interpeduncular nucleus in the rat. *Neuroscience Letters* **64**, 259–262 (1986).
52. Jacobs, B. L. & Azmitia, E. C. Structure and function of the brain serotonin system. *Physiological Reviews* **72**, 165–229 (1992).
53. Rodríguez, J. J., Noristani, H. N. & Verkhratsky, A. The serotonergic system in ageing and Alzheimer's disease. *Progress in Neurobiology* **99**, 15–41 (2012).

54. Cirrito, J. R. *et al.* Serotonin signaling is associated with lower amyloid-β levels and plaques in transgenic mice and humans. *Proc. Natl. Acad. Sci. U.S.A.* **108**, 14968–14973 (2011).
55. Gharedaghi, M. H., Seyedabadi, M., Ghia, J.-E., Dehpour, A. R. & Rahimian, R. The role of different serotonin receptor subtypes in seizure susceptibility. *Exp Brain Res* **232**, 347–367 (2014).
56. Alenina, N. & Klempin, F. The role of serotonin in adult hippocampal neurogenesis. *Behavioural Brain Research* **277**, 49–57 (2015).
57. Švob Štrac, D., Pivac, N. & Mück-Šeler, D. The serotonergic system and cognitive function. *Translational Neuroscience* **7**, 35–49 (2016).
58. Vakalopoulos, C. Alzheimer's Disease: The Alternative Serotonergic Hypothesis of Cognitive Decline. *JAD* **60**, 859–866 (2017).
59. Babić Leko, M., Hof, P. R. & Šimić, G. Alterations and interactions of subcortical modulatory systems in Alzheimer's disease. *Prog Brain Res* **261**, 379–421 (2021).
60. Yu, W., Zhang, R., Zhang, A. & Mei, Y. Deciphering the Functions of Raphe–Hippocampal Serotonergic and Glutamatergic Circuits and Their Deficits in Alzheimer's Disease. *IJMS* **26**, 1234 (2025).
61. Heneka, M. T. *et al.* Neuroinflammation in Alzheimer disease. *Nat Rev Immunol* **25**, 321–352 (2025).
62. Heppner, F. L., Ransohoff, R. M. & Becher, B. Immune attack: the role of inflammation in Alzheimer disease. *Nat Rev Neurosci* **16**, 358–372 (2015).
63. Zhang, Y., Dong, Z. & Song, W. NLRP3 inflammasome as a novel therapeutic target for Alzheimer's disease. *Sig Transduct Target Ther* **5**, 37 (2020).
64. Furgiuele, A., Pereira, F. C., Martini, S., Marino, F. & Cosentino, M. Dopaminergic regulation of inflammation and immunity in Parkinson's disease: friend or foe? *Clin & Trans Imm* **12**, e1469 (2023).
65. Possemato, E., La Barbera, L., Nobili, A., Krashia, P. & D'Amelio, M. The role of dopamine in NLRP3 inflammasome inhibition: Implications for neurodegenerative diseases. *Ageing Research Reviews* **87**, 101907 (2023).
66. Coll, R., O'Neill, L. & Schroder, K. Questions and controversies in innate immune research: what is the physiological role of NLRP3? *Cell Death Discovery* **2**, 16019 (2016).
67. Jo, E.-K., Kim, J. K., Shin, D.-M. & Sasakawa, C. Molecular mechanisms regulating NLRP3 inflammasome activation. *Cell Mol Immunol* **13**, 148–159 (2016).

68. Haneklaus, M. & O'Neill, L. A. J. NLRP3 at the interface of metabolism and inflammation. *Immunological Reviews* **265**, 53–62 (2015).
69. Shao, W. *et al.* Suppression of neuroinflammation by astrocytic dopamine D2 receptors via αB-crystallin. *Nature* **494**, 90–94 (2013).
70. Karrer, T. M., Josef, A. K., Mata, R., Morris, E. D. & Samanez-Larkin, G. R. Reduced dopamine receptors and transporters but not synthesis capacity in normal aging adults: a meta-analysis. *Neurobiology of Aging* **57**, 36–46 (2017).
71. Montoya, A. *et al.* Dopamine receptor D3 signalling in astrocytes promotes neuroinflammation. *J Neuroinflammation* **16**, 258 (2019).
72. Nishikawa, Y. *et al.* Anti-inflammatory effects of dopamine on microglia and a D1 receptor agonist ameliorates neuroinflammation of the brain in a rat delirium model. *Neurochemistry International* **163**, 105479 (2023).
73. Pike, A. F. *et al.* Dopamine signaling modulates microglial NLRP3 inflammasome activation: implications for Parkinson's disease. *J Neuroinflammation* **19**, 50 (2022).
74. Turkin, A., Tuchina, O. & Klempin, F. Microglia Function on Precursor Cells in the Adult Hippocampus and Their Responsiveness to Serotonin Signaling. *Front. Cell Dev. Biol.* **9**, 665739 (2021).
75. Béchade, C. *et al.* The serotonin 2B receptor is required in neonatal microglia to limit neuroinflammation and sickness behavior in adulthood. *Glia* **69**, 638–654 (2021).
76. Mariani, N., Everson, J., Pariante, C. M. & Borsini, A. Modulation of microglial activation by antidepressants. *J Psychopharmacol* **36**, 131–150 (2022).
77. Zheng, Y. & Xu, L. Bidirectional crosstalk between microglia and serotonin signaling in neuroinflammation and CNS disorders. *Front. Immunol.* **16**, 1646740 (2025).
78. Krabbe, G. *et al.* Activation of serotonin receptors promotes microglial injury-induced motility but attenuates phagocytic activity. *Brain, Behavior, and Immunity* **26**, 419–428 (2012).
79. Kolodziejczak, M. *et al.* Serotonin Modulates Developmental Microglia via 5-HT_{2B} Receptors: Potential Implication during Synaptic Refinement of Retinogeniculate Projections. *ACS Chem. Neurosci.* **6**, 1219–1230 (2015).
80. Lim, C. *et al.* Fluoxetine affords robust neuroprotection in the postischemic brain via its anti-inflammatory effect. *J of Neuroscience Research* **87**, 1037–1045 (2009).
81. Saggu, S. *et al.* Monoamine signaling and neuroinflammation: mechanistic connections and implications for neuropsychiatric disorders. *Front. Immunol.* **16**, 1543730 (2025).

82. Vorobyov, V. *et al.* Loss of Midbrain Dopamine Neurons and Altered Apomorphine EEG Effects in the 5xFAD Mouse Model of Alzheimer's Disease. *Journal of Alzheimer's Disease* **70**, 241–256 (2019).
83. Venneri, A. & De Marco, M. Reduced monoaminergic nuclei MRI signal detectable in pre-symptomatic older adults with future memory decline. *Sci Rep* **10**, 18707 (2020).
84. De Marco, M. & Venneri, A. Volume and connectivity of the Ventral Tegmental Area are linked to neurocognitive signatures of Alzheimer's disease in Humans. *J. Alzheimers Dis.* **63**, 167–180 (2018).
85. Manca, R., De Marco, M., Soininen, H., Ruffini, L. & Venneri, A. Changes in neurotransmitter-related functional connectivity along the Alzheimer's disease continuum. *Brain Communications* **7**, fcaf008 (2024).
86. Manca, R., De Marco, M., Soininen, H., Ruffini, L. & Venneri, A. Changes in neurotransmitter-related functional connectivity along the Alzheimer's disease continuum. *Brain Commun* **7**, fcaf008 (2025).
87. Moreira, I. P., Vieira-Coelho, M. A. & Guimarães, J. Dopamine System Dysfunction in Alzheimer's Disease. *Psychogeriatrics* **25**, e70097 (2025).
88. De Marchi, F., Vignaroli, F., Mazzini, L., Comi, C. & Tondo, G. New Insights into the Relationship between Nutrition and Neuroinflammationin Alzheimer's Disease: Preventive and Therapeutic Perspectives. *CNSNDDT* **23**, 614–627 (2024).
89. Blankenship, H. E. *et al.* VTA dopamine neurons are hyperexcitable in 3xTg-AD mice due to casein kinase 2-dependent SK channel dysfunction. *Nat Commun* **15**, 9673 (2024).
90. La Barbera, L. *et al.* Nilotinib restores memory function by preventing dopaminergic neuron degeneration in a mouse model of Alzheimer's Disease. *Progress in Neurobiology* **202**, 102031 (2021).
91. La Barbera, L. *et al.* Upregulation of Ca2+-binding proteins contributes to VTA dopamine neuron survival in the early phases of Alzheimer's disease in Tg2576 mice. *Mol Neurodegeneration* **17**, 76 (2022).
92. Cordella, A. *et al.* Dopamine loss alters the hippocampus-nucleus accumbens synaptic transmission in the Tg2576 mouse model of Alzheimer's disease. *Neurobiol Dis* **116**, 142–154 (2018).

93. Krashia, P., Nobili, A. & D'Amelio, M. Unifying Hypothesis of Dopamine Neuron Loss in Neurodegenerative Diseases: Focusing on Alzheimer's Disease. *Front Mol Neurosci* **12**, 123 (2019).
94. Ficchì, S. *et al.* Optogenetic stimulation of midbrain dopaminergic neurons rescues hippocampal synaptic plasticity deficits in a mouse model of Alzheimer's disease. *Transl Psychiatry* **15**, 371 (2025).
95. De Marco, M. & Venneri, A. Volume and Connectivity of the Ventral Tegmental Area are Linked to Neurocognitive Signatures of Alzheimer's Disease in Humans. *J Alzheimers Dis* **63**, 167–180 (2018).
96. Manca, R., De Marco, M., Soininen, H., Ruffini, L. & Venneri, A. Changes in neurotransmitter-related functional connectivity along the Alzheimer's disease continuum. *Brain Commun* **7**, fcaf008 (2025).
97. Koch, G. *et al.* Altered dopamine modulation of LTD-like plasticity in Alzheimer's disease patients. *Clinical Neurophysiology* **122**, 703–707 (2011).
98. Koch, G. *et al.* Dopaminergic Modulation of Cortical Plasticity in Alzheimer's Disease Patients. *Neuropsychopharmacol* **39**, 2654–2661 (2014).
99. Martorana, A. & Koch, G. â€œIs dopamine involved in Alzheimer's disease?â€. *Front. Aging Neurosci.* **6**, (2014).
100. La Barbera, L. *et al.* Nilotinib restores memory function by preventing dopaminergic neuron degeneration in a mouse model of Alzheimer's Disease. *Progress in Neurobiology* **202**, 102031 (2021).
101. De Paolis, M. L. *et al.* Repetitive prefrontal tDCS activates VTA dopaminergic neurons, resulting in attenuation of Alzheimer's Disease-like deficits in Tg2576 mice. *Alzheimers Res Ther* **17**, 94 (2025).
102. Dahl, M. J. *et al.* The integrity of dopaminergic and noradrenergic brain regions is associated with different aspects of late-life memory performance. *Nat Aging* **3**, 1128–1143 (2023).
103. Bäckman, L., Lindenberger, U., Li, S.-C. & Nyberg, L. Linking cognitive aging to alterations in dopamine neurotransmitter functioning: Recent data and future avenues. *Neuroscience & Biobehavioral Reviews* **34**, 670–677 (2010).
104. Chowdhury, R. *et al.* Dopamine restores reward prediction errors in old age. *Nat Neurosci* **16**, 648–653 (2013).

105. Grinberg, L. T., Rueb, U., Alho, A. T. D. L. & Heinsen, H. Brainstem pathology and non-motor symptoms in PD. *Journal of the Neurological Sciences* **289**, 81–88 (2010).
106. Šimić, G. *et al.* Monoaminergic neuropathology in Alzheimer's disease. *Progress in Neurobiology* **151**, 101–138 (2017).
107. Tejani-Butt, S. M., Yang, J. & Pawlyk, A. C. Altered serotonin transporter sites in Alzheimer's disease raphe and hippocampus: *NeuroReport* **6**, 1207–1210 (1995).
108. Donovan, N. J. *et al.* Subjective Cognitive Concerns and Neuropsychiatric Predictors of Progression to the Early Clinical Stages of Alzheimer Disease. *The American Journal of Geriatric Psychiatry* **22**, 1642–1651 (2014).
109. Ismail, Z. *et al.* Neuropsychiatric symptoms as early manifestations of emergent dementia: Provisional diagnostic criteria for mild behavioral impairment. *Alzheimer's & Dementia* **12**, 195–202 (2016).
110. Heneka, M. T. *et al.* NLRP3 is activated in Alzheimer's disease and contributes to pathology in APP/PS1 mice. *Nature* **493**, 674–678 (2013).
111. Cirrito, J. R. *et al.* Serotonin signaling is associated with lower amyloid-β levels and plaques in transgenic mice and humans. *Proc Natl Acad Sci U S A* **108**, 14968–14973 (2011).
112. Ising, C. *et al.* NLRP3 inflammasome activation drives tau pathology. *Nature* **575**, 669–673 (2019).
113. Xu, W., Huang, Y. & Zhou, R. NLRP3 inflammasome in neuroinflammation and central nervous system diseases. *Cell Mol Immunol* **22**, 341–355 (2025).
114. Josephs, K. A., Weigand, S. D. & Whitwell, J. L. Characterizing Amyloid-Positive Individuals With Normal Tau PET Levels After 5 Years: An ADNI Study. *Neurology* **98**, (2022).
115. Pascoal, T. A. *et al.* Microglial activation and tau propagate jointly across Braak stages. *Nat Med* **27**, 1592–1599 (2021).
116. Bellaver, B. *et al.* Astrocyte reactivity influences amyloid-β effects on tau pathology in preclinical Alzheimer's disease. *Nat Med* **29**, 1775–1781 (2023).
117. Dubois, B. *et al.* Cognitive and neuroimaging features and brain β-amyloidosis in individuals at risk of Alzheimer's disease (INSIGHT-preAD): a longitudinal observational study. *The Lancet Neurology* **17**, 335–346 (2018).
118. Shi, F.-D. & Yong, V. W. Neuroinflammation across neurological diseases. *Science* **388**, eadx0043 (2025).

119. Appleton, J. *et al.* Brain inflammation co-localizes highly with tau in mild cognitive impairment due to early-onset Alzheimer's disease. *Brain* **148**, 119–132 (2025).
120. Schaffer Aguzzoli, C. *et al.* Neuropsychiatric Symptoms and Microglial Activation in Patients with Alzheimer Disease. *JAMA Netw Open* **6**, e2345175 (2023).
121. Shao, W. *et al.* Suppression of neuroinflammation by astrocytic dopamine D2 receptors via αB-crystallin. *Nature* **494**, 90–94 (2013).
122. Turkin, A., Tuchina, O. & Klempin, F. Microglia Function on Precursor Cells in the Adult Hippocampus and Their Responsiveness to Serotonin Signaling. *Front Cell Dev Biol* **9**, 665739 (2021).
123. Yan, Y. *et al.* Dopamine Controls Systemic Inflammation through Inhibition of NLRP3 Inflammasome. *Cell* **160**, 62–73 (2015).
124. Zhu, J. *et al.* Dopamine D2 receptor restricts astrocytic NLRP3 inflammasome activation via enhancing the interaction of β-arrestin2 and NLRP3. *Cell Death Differ* **25**, 2037–2049 (2018).
125. Heneka, M. T. *et al.* Locus ceruleus controls Alzheimer's disease pathology by modulating microglial functions through norepinephrine. *Proc. Natl. Acad. Sci. U.S.A.* **107**, 6058–6063 (2010).
126. D'Amelio, M., Serra, L. & Bozzali, M. Ventral Tegmental Area in Prodromal Alzheimer's Disease: Bridging the Gap between Mice and Humans. *J Alzheimers Dis* **63**, 181–183 (2018).
127. Iaccarino, L. *et al.* In vivo MRI Structural and PET Metabolic Connectivity Study of Dopamine Pathways in Alzheimer's Disease. *J Alzheimers Dis* **75**, 1003–1016 (2020).
128. Sala, A. *et al.* In vivo human molecular neuroimaging of dopaminergic vulnerability along the Alzheimer's disease phases. *Alzheimers Res Ther* **13**, 187 (2021).
129. Tondo, G. *et al.* Brain Metabolism and Microglia Activation in Mild Cognitive Impairment: A Combined [18F]FDG and [11C]-(R)-PK11195 PET Study. *JAD* **80**, 433–445 (2021).
130. Zhang, Y., Liang, Y. & Gu, Y. The dopaminergic system and Alzheimer's disease. *Neural Regen Res* **20**, 2495–2512 (2025).
131. Dutt, S., Li, Y., Mather, M., Nation, D. A., & for the Alzheimer's Disease Neuroimaging Initiative. Brainstem substructures and cognition in prodromal Alzheimer's disease. *Brain Imaging and Behavior* **15**, 2572–2582 (2021).
132. Pilotto, A. *et al.* Dopaminergic deficits along the spectrum of Alzheimer's disease. *Mol Psychiatry* **30**, 3069–3076 (2025).

133. Krashia, P., Spoleti, E. & D'Amelio, M. The VTA dopaminergic system as diagnostic and therapeutical target for Alzheimer's disease. *Front. Psychiatry* **13**, 1039725 (2022).
134. McNamara, C. G., Tejero-Cantero, Á., Trouche, S., Campo-Urriza, N. & Dupret, D. Dopaminergic neurons promote hippocampal reactivation and spatial memory persistence. *Nat Neurosci* **17**, 1658–1660 (2014).
135. Rossato, J. I., Bevilaqua, L. R. M., Izquierdo, I., Medina, J. H. & Cammarota, M. Dopamine Controls Persistence of Long-Term Memory Storage. *Science* **325**, 1017–1020 (2009).
136. La Barbera, L. *et al.* Midbrain degeneration triggers astrocyte reactivity and tau pathology in experimental Alzheimer's Disease. *Mol Neurodegeneration* **20**, 105 (2025).
137. Hsiao, K. *et al.* Correlative memory deficits, Abeta elevation, and amyloid plaques in transgenic mice. *Science* **274**, 99–102 (1996).
138. Yang, C. F. *et al.* Sexually Dimorphic Neurons in the Ventromedial Hypothalamus Govern Mating in Both Sexes and Aggression in Males. *Cell* **153**, 896–909 (2013).
139. Paxinos, G. & Franklin, K. B. J. *Paxinos and Franklin's the Mouse Brain in Stereotaxic Coordinates*. (Academic Press, 2019).
140. Spoleti, E. *et al.* Dopamine neuron degeneration in the Ventral Tegmental Area causes hippocampal hyperexcitability in experimental Alzheimer's Disease. *Mol Psychiatry* **29**, 1265–1280 (2024).
141. Spoleti, E. *et al.* Early derailment of firing properties in CA1 pyramidal cells of the ventral hippocampus in an Alzheimer's disease mouse model. *Exp Neurol* **350**, 113969 (2021).
142. De Paolis, M. L. *et al.* Repetitive prefrontal tDCS activates VTA dopaminergic neurons, resulting in attenuation of Alzheimer's Disease-like deficits in Tg2576 mice. *Alzheimers Res Ther* **17**, 94 (2025).
143. Holmes, B. B. *et al.* Proteopathic tau seeding predicts tauopathy in vivo. *Proceedings of the National Academy of Sciences* **111**, E4376–E4385 (2014).
144. Dobin, A. *et al.* STAR: ultrafast universal RNA-seq aligner. *Bioinformatics* **29**, 15–21 (2013).
145. Pertea, M. *et al.* StringTie enables improved reconstruction of a transcriptome from RNA-seq reads. *Nat Biotechnol* **33**, 290–295 (2015).
146. Love, M. I., Huber, W. & Anders, S. Moderated estimation of fold change and dispersion for RNA-seq data with DESeq2. *Genome Biol* **15**, 550 (2014).
147. Romoli, M. *et al.* Hippocampal epileptogenesis in autoimmune encephalitis. *Ann Clin Transl Neurol* **6**, 2261–2269 (2019).

148. D'Amelio, M. *et al.* Caspase-3 triggers early synaptic dysfunction in a mouse model of Alzheimer's disease. *Nat Neurosci* **14**, 69–76 (2011).
149. Wang, F. *et al.* A sensory-motor-sensory circuit underlies antinociception ignited by primary motor cortex in mice. *Neuron* **113**, 1947-1968.e7 (2025).
150. Cabib, S., Pascucci, T., Ventura, R., Romano, V. & Puglisi-Allegra, S. The Behavioral Profile of Severe Mental Retardation in a Genetic Mouse Model of Phenylketonuria. *Behav Genet* **33**, 301–310 (2003).
151. Nardecchia, F. *et al.* Targeting mGlu5 Metabotropic Glutamate Receptors in the Treatment of Cognitive Dysfunction in a Mouse Model of Phenylketonuria. *Front. Neurosci.* **12**, 154 (2018).
152. Sciamanna, G. *et al.* Optogenetic Activation of Striatopallidal Neurons Reveals Altered HCN Gating in DYT1 Dystonia. *Cell Reports* **31**, 107644 (2020).
153. Anders, S. & Huber, W. Differential expression analysis for sequence count data. *Genome Biology* **11**, R106 (2010).
154. Gasbarri, A., Verney, C., Innocenzi, R., Campana, E. & Pacitti, C. Mesolimbic dopaminergic neurons innervating the hippocampal formation in the rat: a combined retrograde tracing and immunohistochemical study. *Brain Research* **668**, 71–79 (1994).
155. Lammel, S. *et al.* Diversity of Transgenic Mouse Models for Selective Targeting of Midbrain Dopamine Neurons. *Neuron* **85**, 429–438 (2015).
156. Lindeberg, J. *et al.* Transgenic expression of Cre recombinase from the tyrosine hydroxylase locus. *Genesis* **40**, 67–73 (2004).
157. Gompf, H. S., Budygin, E. A., Fuller, P. M. & Bass, C. E. Targeted genetic manipulations of neuronal subtypes using promoter-specific combinatorial AAVs in wild-type animals. *Front. Behav. Neurosci.* **9**, (2015).
158. Broussard, J. I. *et al.* Dopamine Regulates Aversive Contextual Learning and Associated In Vivo Synaptic Plasticity in the Hippocampus. *Cell Reports* **14**, 1930–1939 (2016).
159. Teixeira, C. M. *et al.* Hippocampal 5-HT Input Regulates Memory Formation and Schaffer Collateral Excitation. *Neuron* **98**, 992-1004.e4 (2018).
160. Venegas, C. & Heneka, M. T. Inflammasome-mediated innate immunity in Alzheimer's disease. *FASEB J* **33**, 13075–13084 (2019).
161. Nisticò, R. *et al.* Inflammation Subverts Hippocampal Synaptic Plasticity in Experimental Multiple Sclerosis. *PLoS ONE* **8**, e54666 (2013).

162. Chae, S. *et al.* The dopamine analogue CA140 alleviates AD pathology, neuroinflammation, and rescues synaptic/cognitive functions by modulating DRD1 signaling or directly binding to Abeta. *J Neuroinflammation* **21**, 200 (2024).
163. Lian, H. *et al.* NFκB-Activated Astroglial Release of Complement C3 Compromises Neuronal Morphology and Function Associated with Alzheimer's Disease. *Neuron* **85**, 101–115 (2015).
164. Lian, H. *et al.* Astrocyte-Microglia Cross Talk through Complement Activation Modulates Amyloid Pathology in Mouse Models of Alzheimer's Disease. *J. Neurosci.* **36**, 577–589 (2016).
165. Litvinchuk, A. *et al.* Complement C3aR Inactivation Attenuates Tau Pathology and Reverses an Immune Network Deregulated in Tauopathy Models and Alzheimer's Disease. *Neuron* **100**, 1337-1353.e5 (2018).
166. Liddelow, S. A. *et al.* Neurotoxic reactive astrocytes are induced by activated microglia. *Nature* **541**, 481–487 (2017).
167. Wu, T. *et al.* Complement C3 Is Activated in Human AD Brain and Is Required for Neurodegeneration in Mouse Models of Amyloidosis and Tauopathy. *Cell Reports* **28**, 2111-2123.e6 (2019).
168. Xu, X. *et al.* MFG-E8 reverses microglial-induced neurotoxic astrocyte (A1) via NF-κB and PI3K-Akt pathways. *Journal Cellular Physiology* **234**, 904–914 (2019).
169. Ito, S. *et al.* The complement C3-complement factor D-C3a receptor signalling axis regulates cardiac remodelling in right ventricular failure. *Nat Commun* **13**, 5409 (2022).
170. Chi, X. *et al.* Astrocyte-neuron communication through the complement C3-C3aR pathway in Parkinson's disease. *Brain, Behavior, and Immunity* **123**, 229–243 (2025).
171. Lovestone, S. *et al.* Alzheimer's disease-like phosphorylation of the microtubule-associated protein tau by glycogen synthase kinase-3 in transfected mammalian cells. *Current Biology* **4**, 1077–1086 (1994).
172. Rankin, C. A., Sun, Q. & Gamblin, T. C. Tau phosphorylation by GSK-3β promotes tangle-like filament morphology. *Mol Neurodegeneration* **2**, 12 (2007).
173. Aplin, A. E., Gibb, G. M., Jacobsen, J. S., Gallo, J. & Anderton, B. H. In Vitro Phosphorylation of the Cytoplasmic Domain of the Amyloid Precursor Protein by Glycogen Synthase Kinase-3β. *Journal of Neurochemistry* **67**, 699–707 (1996).

174. Ly, P. T. T. *et al.* Inhibition of GSK3β-mediated BACE1 expression reduces Alzheimer-associated phenotypes. *J. Clin. Invest.* **123**, 224–235 (2013).
175. Apelt, J. & Schliebs, R. β-Amyloid-induced glial expression of both pro- and anti-inflammatory cytokines in cerebral cortex of aged transgenic Tg2576 mice with Alzheimer plaque pathology. *Brain Research* **894**, 21–30 (2001).
176. Delizannis, A. T. *et al.* Effects of microglial depletion and TREM2 deficiency on Aβ plaque burden and neuritic plaque tau pathology in 5XFAD mice. *acta neuropathol commun* **9**, 150 (2021).
177. Gloria, Y., Ceyzériat, K., Tsartsalis, S., Millet, P. & Tournier, B. B. Dopaminergic dysfunction in the 3xTg-AD mice model of Alzheimer's disease. *Sci Rep* **11**, 19412 (2021).
178. Diaz, A., Limon, D., Chávez, R., Zenteno, E. & Guevara, J. Aβ25-35 Injection into the Temporal Cortex Induces Chronic Inflammation that Contributes to Neurodegeneration and Spatial Memory Impairment in Rats. *JAD* **30**, 505–522 (2012).
179. Ramírez, E. *et al.* Neuroinflammation induced by the peptide amyloid-β (25–35) increase the presence of galectin-3 in astrocytes and microglia and impairs spatial memory. *Neuropeptides* **74**, 11–23 (2019).
180. Zhu, H. *et al.* Noteworthy perspectives on microglia in neuropsychiatric disorders. *J Neuroinflammation* **20**, 223 (2023).
181. Leng, F. & Edison, P. Neuroinflammation and microglial activation in Alzheimer disease: where do we go from here? *Nat Rev Neurol* **17**, 157–172 (2021).
182. Malpetti, M. *et al.* Microglial activation and tau burden predict cognitive decline in Alzheimer's disease. *Brain* **143**, 1588–1602 (2020).
183. Madsen, L. S. *et al.* Microglial responses partially mediate the effect of Aβ on cognition in Alzheimer's disease. *Alzheimer's & Dementia* **20**, 8028–8037 (2024).
184. Du, R.-H. *et al.* Fluoxetine Inhibits NLRP3 Inflammasome Activation: Implication in Depression. *Int J Neuropsychopharmacol* **19**, pyw037 (2016).
185. Zabot, G. C. *et al.* The involvement of inflammation in the effect of the administration of donepezil, galantamine, memantine and/or fluoxetine in an animal model of depression and dementia. *Alzheimer's & Dementia* **17**, e056472 (2021).
186. Sánchez-Juan, P. *et al.* Serum GFAP levels correlate with astrocyte reactivity, post-mortem brain atrophy and neurofibrillary tangles. *Brain* **147**, 1667–1679 (2024).

187. Serra, L. *et al.* Ventral Tegmental Area Disconnection Contributes Two Years Early to Correctly Classify Patients Converted to Alzheimer's Disease: Implications for Treatment. *J Alzheimers Dis* **82**, 985–1000 (2021).
188. Sárkány, Z., Damásio, J., Macedo-Ribeiro, S. & Martins, P. M. Association between the use of levodopa/carbidopa, Alzheimer's disease biomarkers, and cognitive decline among participants in the National Alzheimer's Coordinating Center Uniform Data Set. *Alzheimers Dement* **21**, e70213 (2025).
189. Nobili, A. & D'Amelio, M. Reconsidering dopaminergic modulation in Alzheimer's disease: A case for levodopa/carbidopa as a disease-modifying agent. *Alzheimers Dement* **21**, e70532 (2025).
190. Svenningsson, P. *et al.* Diverse psychotomimetics act through a common signaling pathway. *Science* **302**, 1412–1415 (2003).
191. Watamura, N. *et al.* The dopaminergic system promotes neprilysin-mediated degradation of amyloid-β in the brain. *Science Signaling* **17**, eadk1822 (2024).
192. Cataldi, R. *et al.* A dopamine metabolite stabilizes neurotoxic amyloid-β oligomers. *Commun Biol* **4**, 1–10 (2021).
193. Li, J., Zhu, M., Manning-Bog, A. B., Di Monte, D. A. & Fink, A. L. Dopamine and L-dopa disaggregate amyloid fibrils: implications for Parkinson's and Alzheimer's disease. *The FASEB Journal* **18**, 962–964 (2004).
194. Terstege, D. J. *et al.* SSRIs reduce plasma tau and restore dorsal raphe metabolism in Alzheimer's disease. *Alzheimer's & Dementia* **21**, e14579 (2025).
195. Ising, C. *et al.* NLRP3 inflammasome activation drives tau pathology. *Nature* **575**, 669–673 (2019).
196. Pascoal, T. A. *et al.* Microglial activation and tau propagate jointly across Braak stages. *Nat Med* **27**, 1592–1599 (2021).
197. Bellaver, B. *et al.* Astrocyte reactivity influences amyloid-β effects on tau pathology in preclinical Alzheimer's disease. *Nat Med* **29**, 1775–1781 (2023).
198. Appleton, J. *et al.* Brain inflammation co-localizes highly with tau in mild cognitive impairment due to early-onset Alzheimer's disease. *Brain* awae234 (2024) doi:10.1093/brain/awae234.
199. Josephs, K. A., Weigand, S. D. & Whitwell, J. L. Characterizing Amyloid-Positive Individuals With Normal Tau PET Levels After 5 Years. *Neurology* **98**, e2282–e2292 (2022).

200. Wearn, A. *et al.* Neuromodulatory subcortical nucleus integrity is associated with white matter microstructure, tauopathy and APOE status. *Nat Commun* **15**, 4706 (2024).
201. Theofilas, P., Dunlop, S., Heinsen, H. & Grinberg, L. T. Turning on the Light Within: Subcortical Nuclei of the Isodentritic Core and their Role in Alzheimer's Disease Pathogenesis. *Journal of Alzheimer's Disease* **46**, 17–34 (2015).
202. Ehrenberg, A. J. *et al.* Priorities for research on neuromodulatory subcortical systems in Alzheimer's disease: Position paper from the NSS PIA of ISTAART. *Alzheimer's & Dementia* **19**, 2182–2196 (2023).